SIMPLE TRENDS IN ATOMIC NUCLEI

D. T. Yordanov

Orsay, 2020

Preface: The following summarizes a series of publications on the subject of nuclear structure from laser spectroscopy. A general perspective on the complexity of the nuclear many-body problem is presented, with emphasis on theoretical concepts permitting a simpler understanding. The experimental observables from laser spectroscopy and the regular patterns they exhibit under certain conditions are discussed in detail. Highlighted is the importance of atomic theory for high-resolution measurements. A guideline to a newly constructed instrumentation for collinear laser spectroscopy is presented.

CONTENTS

A. MANY - BODY PROBLEM

Nuclear is the most recent and complex of many-body problems that have arisen throughout history. The motion of only three point masses, for instance, interacting according to Newton's law of universal gravitation is generally chaotic, as pointed out by Poincaré in 1892 [1], and remains as "arguably the oldest open question in astrophysics" [2]. The latter is not to suggest that a general solution does not exist; the problem can be solved numerically, as spectacularly demonstrated in space exploration [3].

The helium atom, with two electrons and a doubly-charged nucleus, is a quantum-mechanical analogue to the celestial three-body problem. Unlike hydrogen, helium, as any other multi-electron system, requires approximations, and dedicated computational schemes, such as the multiconfiguration Dirac-Hartree-Fock method [4, 5] discussed here.

Three-body problems are fundamental also in the standard model. The proton and the neutron, for instance, consist of three quarks each. So far, their magnetic moments have not been adequately explained and only recently have been calculated reasonably from first principles [6].

"It was clear that there is no exact solution to the nuclear many-body problem", as Talmi recalls [7]. Indeed, nuclei may comprise up to hundreds of nucleons whose interaction is not explicitly known, despite many aspects of the nuclear force being quantified through experimentation, or fairly understood, e.g., long-range attraction, short-range repulsion, tensor component, etc. Nuclei are also profoundly affected by the repulsive Coulomb force [8] between protons. Being such complex systems, it is rather curious that they are generally described by a shell model [9] largely inspired by atomic physics.

The following does not elaborate directly on the nuclear many-body problem or the associated mean-field approximations and effective interactions. However, it is shown here, empirically, in spite of the underlined complexity, that electromagnetic properties may evolve from one isotope to another in an extremely predictable manner. Regularities as these, observed at high experimental precision, are a consequence of the underlined symmetries and many-body correlations within the nucleus [10].

Experimental findings on nuclear charge radii, magnetic-dipole, and electric-quadrupole moments from collinear laser spectroscopy are discussed here from a simple perspective [11, 12] and further analysed through large-scale-shell-model and density-functional-theory calculations in the appended publications.

B. ELECTROMAGNETIC OBSERVABLES

The following summarizes the basic formalism and certain formulae derivations invoked in the subsequent discussions of experimental results on electromagnetic moments and mean square charge radii. So it begins; the interaction of the nucleus with the multipole components of the electromagnetic field is quantified by:

$$\mathscr{M}_{\lambda\eta=0} = \langle I, M = I | \sum_{k=1}^{A} \hat{T}_{\lambda\eta=0}(k) | I, M = I \rangle, \tag{B.1}$$

where $\hat{T}_{\lambda\eta}$ is a one-body tensor operator of rank λ representing either the electric moments $\hat{Q}_{\lambda\eta}$ associated with the static distribution of charge, or the magnetic moments $\hat{M}_{\lambda\eta}$ rising from charge currents. Having respective parities $(-)^{\lambda}$ and $(-)^{\lambda+1}$ [13], and considering parity conservation, only even electric and odd magnetic operators are defined. For spherical tensor operators the M-state dependence of the matrix elements reduces to a dependence on the Clebsch-Gordan or $3j$ coefficient via the Wigner-Eckart theorem:

$$\langle IM | \hat{T}_{\lambda\eta} | IM \rangle = (-1)^{I-M} \begin{pmatrix} I & \lambda & I \\ -M & \eta & M \end{pmatrix} \langle I || \hat{T}_{\lambda} || I \rangle, \tag{B.2}$$

where $\langle I || \hat{T}_{\lambda} || I \rangle$ is the reduced matrix element. According to the properties of the $3j$ coefficients $\eta = 0$ and $\lambda \leq 2I$. The only moment defined for $I = 0$ is the electric monopole moment $\sum_{k=1}^{A} e_k$ $(\lambda = 0)$, which represents the total charge of the nucleus. The magnetic dipole moment $(\lambda = 1)$ is defined for $I \geq 1/2$ and the electric quadrupole moment $(\lambda = 2)$ for $I \geq 1$. The dipole moment operator for a single nucleon in a static binding field is defined as:

$$\hat{\mu} = \mu_{\mathrm{N}} \left(g_l^{t_z} \hat{l} + g_s^{t_z} \hat{s} \right) / \hbar, \tag{B.3}$$

where $g_l^{t_z}$ and $g_s^{t_z}$ are the orbital and spin gyromagnetic ratios of the nucleon in terms of nuclear magnetons $\mu_{\mathrm{N}} = e\hbar/2m_{\mathrm{p}} = 5.0507837461(15) \times 10^{-27}$ J/T [14]. The index t_z represents the isospin of the particle, either $-1/2$ for protons "p" or $1/2$ for neutrons "n". The orbital g factors are deduced from the definition, while the spin g factors derive from the proton and the neutron magnetic moments, as tabulated [14]:

$$\begin{aligned} g_l^{\mathrm{p}} &= 1, & g_l^{\mathrm{n}} &= 0, \\ g_s^{\mathrm{p}} &= 5.5856946893(16) = 2\mu_{\mathrm{p}}/\mu_{\mathrm{N}}, & g_s^{\mathrm{n}} &= -3.82608545(90) = 2\mu_{\mathrm{n}}/\mu_{\mathrm{N}}. \end{aligned} \tag{B.4}$$

Since g_s of the neutron is different from zero, and that of the proton is far from the expectation value of two from the Dirac equation, shows, as indicated earlier, that neither is an elementary particle. The single-particle magnetic moments, also known as Schmidt values, can be derived with the use of the projection theorem [15]. It is useful to explicitly show their m-dependence through the use of B.2 and tabulated $3j$ symbols [12]. The result is:

$$\mu = m \left(g_l^{t_z} \pm \frac{g_s^{t_z} - g_l^{t_z}}{2l+1} \right) \mu_{\mathrm{N}}, \; j = l \pm \frac{1}{2}. \tag{B.5}$$

Thus, adjacent m states produce no magnetic moment, since $\mu(m)+\mu(-m)=0$ according to B.5. Crucially, this is not the case for quadrupole moments, as discussed further. Single-particle magnetic moments are generally weaker than the Schmidt values. As a result, the nucleon g factors in nuclei differ from the free values in B.4. An approach to this discrepancy is to consider effective g factors, calculated microscopically [16, 17] or fitted to experimental data. The nuclear gyromagnetic ratio g of a state with an angular momentum $\hat{I}$ is defined by:

$$\langle\hat{\mu}\rangle = g\,\hat{I}\,\mu_{\mathrm{N}}/\hbar \quad \Rightarrow \quad \mu = g\,I\,\mu_{\mathrm{N}}. \tag{B.6}$$

The g factor of a composite state can be calculated from the g factors of its constituents [15]. A consequence from the result given below is that any multi-nucleon coupling in the same orbital preserves the g factor, but not necessarily the magnetic moment.

$$g = \frac{g_1+g_2}{2} + \frac{g_1-g_2}{2}\times\frac{I_1(I_1+1)-I_2(I_2+1)}{I(I+1)} \tag{B.7}$$

The magnetic moment of a nucleus essentially quantifies its ability to experience torque when subjected to a magnetic field. Its electric quadrupole moment on the other hand, defined below as the third component of the respective tensor operator from classical electrodynamics, is a measure for the departure of the nuclear charge distribution from spherical symmetry.

$$e\,\hat{Q} = e^{t_z}e\left(3z^2-r^2\right) \tag{B.8}$$

Here e^{t_z} represents the effective charge of the carrier, either a proton or a neutron, in units e. These quantities can also be obtained empirically or theoretically [17]. As defined above, the quadrupole moment does not incorporate the elementary charge and acquires the dimension of a surface. It is worth pointing out that the alternative convention causes no ambiguity as the elementary charge is then incorporated into the units, such that the actual values are preserved. As expected, in systems with spherical symmetry $|\psi(\hat{r})|^2 = |\psi(r)|^2$ B.8 vanishes because of the equality of the expectation values: $\langle x^2\rangle = \langle y^2\rangle = \langle z^2\rangle = \langle r^2\rangle/3$. The electric quadrupole moment depends on the average size of the proton distribution. In general, the radial moments [18] can be defined as:

$$\langle r^n\rangle = \frac{\int \rho(\hat{r})\,r^n\,dV}{\int \rho(\hat{r})\,dV}, \tag{B.9}$$

where $\rho(\hat{r})$ represents the nuclear charge-distribution density in the elementary volume dV. Generalized with the use of B.2 and tabulated $3j$ symbols [12], the single-particle quadrupole moment [19] becomes:

$$\langle jm|e\,\hat{Q}|jm\rangle = \frac{j(j+1)-3m^2}{2j(j+1)}\left\langle r^2\right\rangle e^{t_z}e. \tag{B.10}$$

The sum over all states in B.10 vanishes,[1] regardless of adjacent m states contributing to a finite moment as a result of $Q(m)=Q(-m)$. However, for an odd number of nucleons n in a

[1] $\sum_{m=-j}^{j} m^2 = j(j+1)(2j+1)/3$;

single orbital with an angular momentum j, the states with maximum projection $m = \pm j$ are not available to nucleon pairs due to a single nucleon occupying the $m = j$ state. The quadrupole moment of such j^n configuration becomes:[2]

$$\langle j^n | e\hat{Q} | j^n \rangle = \frac{2j+1-2n}{2j-1} \langle jj | e\hat{Q} | jj \rangle. \tag{B.11}$$

This equation gives rise to a liner mass dependence, which intercepts the zero line in the middle of the shell. The general form of B.11 for high-seniority states can be found in Ref. [12]. On the subject of compound states [19], the quadrupole moment corresponding to B.7 is given by:

$$Q = q(I_1, I_2, I) Q_1 + q(I_2, I_1, I) Q_2, \tag{B.12}$$

where:

$$q(I_a, I_b, I) = (-1)^{I_a+I_b+I}(2I+1) \begin{Bmatrix} I_a & I_b & I \\ I & 2 & I_a \end{Bmatrix} \begin{pmatrix} I & I & 2 \\ I & -I & 0 \end{pmatrix} \begin{pmatrix} I_a & I_a & 2 \\ I_a & -I_a & 0 \end{pmatrix}^{-1}.$$

The observation of large quadrupole moments has been attributed to collective phenomena resulting in nuclear deformations [20]. In the case of $\lambda = 2$ the nuclear shape is parametrized with:

$$\underset{k=1,2,3}{R_k} = R_0 \left[1 + \sqrt{\frac{5}{4\pi}}\, \beta\, \cos\left(\gamma - \frac{2k\pi}{3} \right) \right], \tag{B.13}$$

where β and γ are the Hill-Wheeler coordinates [21]. In the axially symmetric case ($\gamma = 0 \Leftrightarrow R_1 = R_2 = R_\perp$) the following relation exists:

$$\frac{R_3 - R_\perp}{R_0} = \frac{3\beta}{4}\sqrt{\frac{5}{\pi}}. \tag{B.14}$$

The intrinsic quadrupole moment of an axially-symmetric nucleus with Z protons relates to the quadrupole deformation β by:

$$Q_0 = Z \left\langle r^2 \right\rangle \beta \sqrt{\frac{5}{\pi}} \left(1 + \frac{\beta}{8}\sqrt{\frac{5}{\pi}} \right). \tag{B.15}$$

The latter holds in the reference frame of the nucleus. In the laboratory frame of reference the angular-momentum algebra provides the relation:[3]

$$Q = \langle IK20|IK\rangle \langle II20|II\rangle\, Q_0 = \frac{3K^2 - I(I+1)}{(I+1)(2I+3)}\, Q_0, \tag{B.16}$$

to be taken with caution for small deformations when simple geometrical relations do not apply. This is particularly true for the isotopes of tin and cadmium discussed here, which are found to be close to spherical.

---

[2] $\langle j^n | e\hat{Q} | j^n \rangle = \langle jj | e\hat{Q} | jj \rangle + \sum_{m=1-j}^{j-1} (n-1) \langle jm | e\hat{Q} | jm \rangle / (2j-1)$, where $\sum_{m=1-j}^{j-1} \langle jm | e\hat{Q} | jm \rangle = -2 \langle jj | e\hat{Q} | jj \rangle$.

[3] $\langle J_1 M_1 J_2 M_2 | JM \rangle = (-1)^{J_1 - J_2 + M} \sqrt{2J+1} \begin{pmatrix} J_1 & J_2 & J \\ M_1 & M_2 & -M \end{pmatrix}$, where $M_1 + M_2 = M$.

C. HYPERFINE STRUCTURE

Electromagnetic moments and mean square charge radii defined with the former are observables from laser spectroscopy, as they determine various aspects of the atomic hyperfine structure [22] discussed in the following. The electron cloud in an atom generates an electromagnetic environment at the origin which interacts with the multipole moments of the nucleus. The corresponding Hamiltonian in its most general form is:

$$\hat{H} = \hat{H}(M1) + \hat{H}(E2) + \ldots \tag{C.1}$$

The hyperfine interaction couples the angular momenta of the nucleus $\hat{I}$ and the electrons $\hat{J}$, being no longer integrals of motion, to the total angular-momentum operator $\hat{F} = \hat{I} + \hat{J}$. Thus, the quantum number F is used to denote the quantum states $|JIFM_F\rangle$. Since $\hat{F}$ satisfies the triangle condition the number of states in a hyperfine multiplet is $2I+1$ for $I \leq J$ and $2J+1$ for $I \geq J$. The magnetic dipole term in C.1 is:

$$\hat{H}(M1) = -\langle\hat{\mu}\rangle \cdot \langle\hat{B}\rangle = A\frac{\hat{I}\cdot\hat{J}}{\hbar^2}, \tag{C.2}$$

where $\langle\hat{\mu}\rangle$ is given by B.6 and $\hat{B}$ is the magnetic field associated with the total magnetic moment of the electrons. One can write:

$$\langle\hat{B}\rangle = -B_0\,\hat{J}/\hbar J, \tag{C.3}$$

where B_0 is a scalar quantity representing the average flux density of the magnetic field at the origin. For alkali-like atoms the general direction of $\hat{B}$ is anti-parallel to the angular momentum $\hat{J}$, thus $B_0 > 0$. The energy levels depend on the product $\hat{I}\cdot\hat{J}$, which can be expressed as a function of $\hat{J}^2$, $\hat{I}^2$, and $\hat{F}^2$ by squaring $\hat{F} = \hat{I} + \hat{J}$. It can be shown with the use of B.6 and C.3 that the magnetic dipole hyperfine parameter takes the value:

$$A = \frac{g\,\mu_N B_0}{J}. \tag{C.4}$$

In free atoms the second term in C.1 is of the form:

$$\hat{H}(E2) = \frac{eQV_{JJ}}{4I(2I-1)\hbar^2}\,(3\hat{I}_z^2 - \hat{I}^2), \tag{C.5}$$

where V_{JJ} is the average electric-field gradient at the nucleus, induced by the atomic electrons having a cylindrical symmetry about the J axis, and

$$B = eQV_{JJ} \tag{C.6}$$

is the electric quadrupole hyperfine parameter. The energy levels of the hyperfine structure are described with:

$$E_F = E_J + A\frac{k}{2} + B\,\frac{3k(k+1) - 4I(I+1)J(J+1)}{8I(2I-1)J(2J-1)}, \tag{C.7}$$

where $k = F(F+1) - I(I+1) - J(J+1)$ and E_J is the energy of the associated fine-structure level. The B parameter, and therefore the second term in C.7, vanishes for either $J = 1/2$ or $I = 1/2$. Electromagnetic moments are generally extracted through C.4 and C.6 relative to a reference isotope using $A/g = \text{const}$ and $B/Q = \text{const}$. Both, however, present a challenge. At high experimental precision the influence on the A hyperfine constant by the extended nuclear magnetization, known as Bohr-Weisskopf effect, and the extended nuclear charge distribution, known as Breit-Rosenthal-Crawford-Schawlow correction, needs to be considered. These contribute to the hyperfine anomaly:

$$^1\Delta^2 = \frac{A_1}{A_2}\frac{g_2}{g_1} - 1, \tag{C.8}$$

which in the absence of nuclear magnetic-resonance measurements needs to be derived from atomic theory. More critical is the issue with electric-field gradients, which historically have been deduced from semi-empirical calculations, whose uncertainties have been assumed on the level of 10%. Contemporary atomic calculations, however, reveal much bigger inaccuracies. Calibrating with a reference isotope, as mentioned above, implicitly perpetuates those inaccuracies to newer studies. The field of laser spectroscopy has now reached a point when solid conclusions on nuclear effects require having the atomic effects under control. This summary offers further discussion on the subject.

Electric dipole transitions obey the selection rules $\Delta F = 0, \pm 1$, and $F + F' \geq 1$ invoked by the triangle condition. Dipole radiation within the same multiplet is forbidden by the parity selection rule. The decay rate per atom, known as Racah intensities [23], is given by:

$$R = \frac{\xi}{3\tau}\frac{(2J_1+1)(2F_1+1)(2F_2+1)}{(2I+1)(2J_2+1)}\begin{Bmatrix} J_2 & F_2 & I \\ F_1 & J_1 & 1 \end{Bmatrix}^2, \tag{C.9}$$

where τ is the lifetime of the excited atomic state and ξ is the ratio between the induced and spontaneous emission coefficients, which incorporates the laser intensity and the spectral lineshape. A change in the nuclear mean square charge radius causes a change in the transition energies:

$$\delta\nu^{AA'} = K\frac{m_A - m_{A'}}{m_A m_{A'}} + \Phi\,\delta\left\langle r^2\right\rangle^{AA'}. \tag{C.10}$$

The latter is known as an isotope shift when the effect concerns two isotopes, or an isomer shift when two states in the same nucleus are involved, in which case the change in the nuclear mass is neglected:

$$\delta\nu = \Phi\,\delta\left\langle r^2\right\rangle. \tag{C.11}$$

The field-shift coefficient[4] Φ is typically determined through a King-plot procedure [24], which requires at least three radii to be known beforehand, usually form experiments with muonic atoms of stable isotopes. Some isotopic chains need atomic calculations for the field-shift coefficient due to the lack of muonic data. This is not discussed here, as tin has the largest number of (ten) stable isotopes, cadmium has the third largest, and magnesium has the minimum number required.

[4] Traditionally denoted by F, which is ambiguous with respect to the total angular momentum $\hat{F}$.

D. INSTRUMENTATION FOR COLLINEAR LASER SPECTROSCOPY

Collinear is the type of laser spectroscopy sampling atoms moving along the path set by a probe laser. Atomic beams with well-defined energies of the order of tens of keV in combination with narrow-band lasers facilitate high-resolution measurements limited essentially by the atomic lifetime broadening.[5] The method utilizes the relativistic Doppler effect:

$$\nu = \nu_0(1-\beta\cos\phi)/\sqrt{1-\beta^2}, \tag{D.1}$$

where ϕ is the angle between the propagation direction of the laser radiation and the velocity $\vec{v}$ of the atomic beam, and takes values of $\phi = 0$ and $\phi = 2\pi$ radians for collinear and anti-collinear geometry, respectively. The Doppler-shifted frequency ν is scanned to match the transitions of the hyperfine structure by varying the velocity $|\vec{v}|$ while the laser frequency ν_0 is kept constant, or vice versa. The following relation holds:

$$\beta = \frac{|\vec{v}|}{c} = \sqrt{1-\frac{M_0^2c^4}{(Uq+M_0c^2)^2}}, \tag{D.2}$$

where U is the acceleration potential for ions of charge q with a rest mass M_0, and c is the speed of light. In the majority of cases, measurements are implemented in neutral atoms, thus, after neutralisation [25] of the singly-ionized beams typically used for acceleration. Resonant laser excitations are detected by various means, e.g., atomic-beam fluorescence, β-decay asymmetry, or changes in ion count rates [26]. The progress in the field has been comprehensively outlined in recent reviews [27, 28].

One of the pioneering experiments by laser spectroscopy on radioactive beams was performed using $^{21,\,22,\,24,\,25}$Na radioactivity from the Orsay synchrocyclotron [29]. The measurements were subsequently extended up to ^{31}Na at CERN [30] using the same technique of magnetic-substate separation after optical pumping. A program was later initiated at ISOLDE by the collaboration for spectroscopy measurements using a pulsed-laser ion source, COMPLIS [31], which studied the lead [32–34] and tin [35, 36] regions, including refractory elements. This program was preceded by work at the ISOCELE separator at Orsay [37–39]. The following may thus be considered in the broad context of local tradition.

The instrument in Fig. 1 has been constructed at the ALTO laboratory [40] along the provisional timeline of the future facility for decay excitation and storage of radioactive ions DESIR [41], where it is expected to complement in-gas-jet laser spectroscopy at GANIL's super separator spectrometer. Financial support has been provided by the Orsay Nuclear Physics Institute, the P2IO Laboratory of Excellence, the French National Institute for Nuclear and Particle Physics, and Paris-Sud University. Complete technical specifications, data from off-line commissioning, and perspectives are presented in "Instrumentation for high-resolution laser spectroscopy at the ALTO radioactive-beam facility" [42] appended to this summary.

[5] Natural linewidth in angular frequency: $\Gamma = \tau^{-1}$.

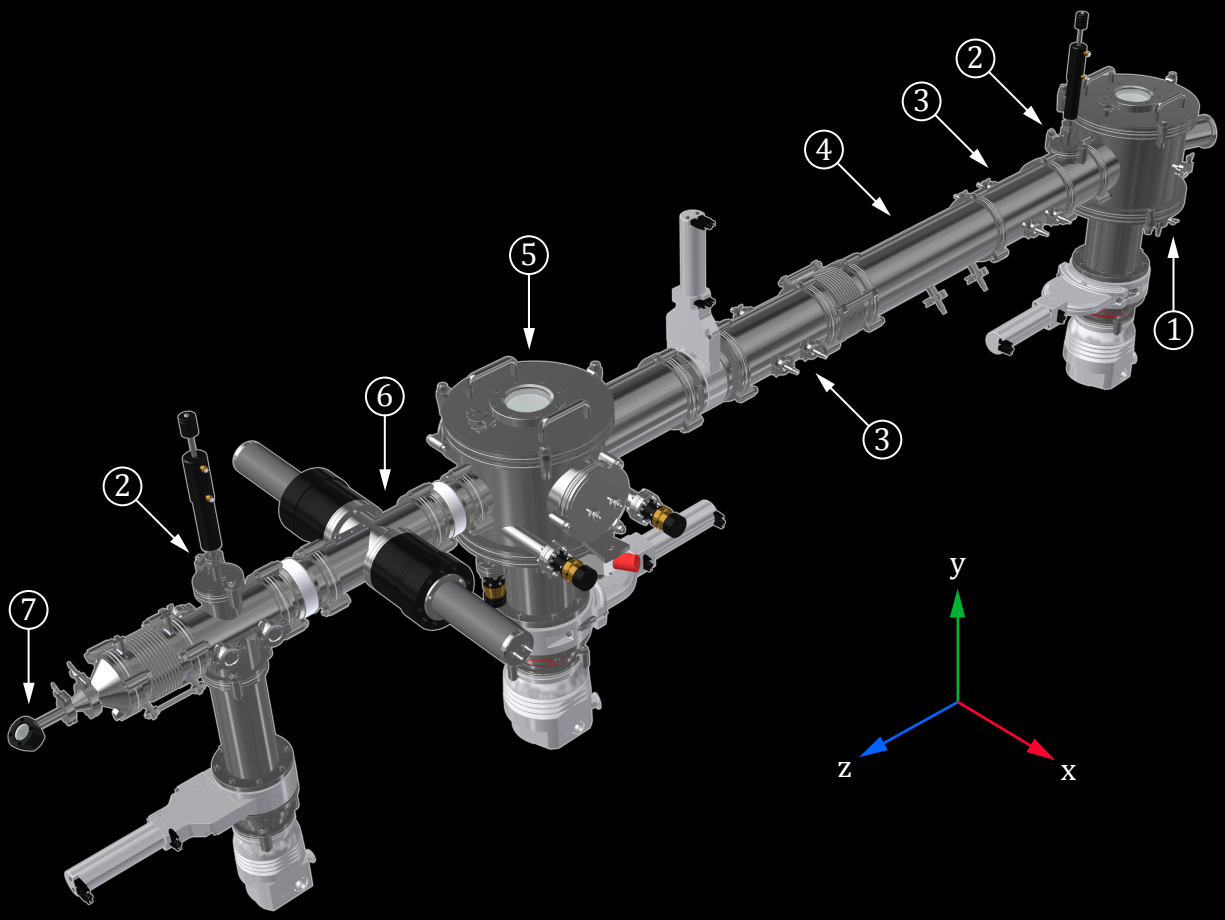

Figure 1. Vacuum beamline: 1.) Merging bender; 2.) Faraday cups; 3.) Electrostatic x-y deflectors; 4.) Electrostatic quadrupole triplet; 5.) Post-acceleration and charge-exchange chamber; 6.) Optical detection; 7.) Fused-silica window at Brewster's angle;

E. SIMPLE TRENDS IN ELECTROMAGNETIC MOMENTS

It is well established that schematic descriptions, such as the seniority or generalized seniority, are instrumental in understanding the simple features of semi-magic nuclei [7]. These explain regular patterns in proton- and neutron-separation energies, excitation energies, and other quantities including electromagnetic transitions. Quadrupole moments have only recently been determined with sufficient accuracy in the isotopes of tin ($Z = 50$) and cadmium ($Z = 48$) to permit a conclusive discussion. These results are summarized below, following the chronological order of the appended publications [43–46].

"Spins, electromagnetic moments, and isomers of $^{107\text{-}129}$Cd" [43], also highlighted in "Physics" [47], reports high-resolution measurements in the alkali-like ion of cadmium. The corresponding laser wavelength of 214 nm was produced by two second-harmonic generation cavities in series, thus by frequency quadrupling. Demonstrating capabilities so close to the absorption barrier of air at 200 nm opened possibilities for studies of other elements with

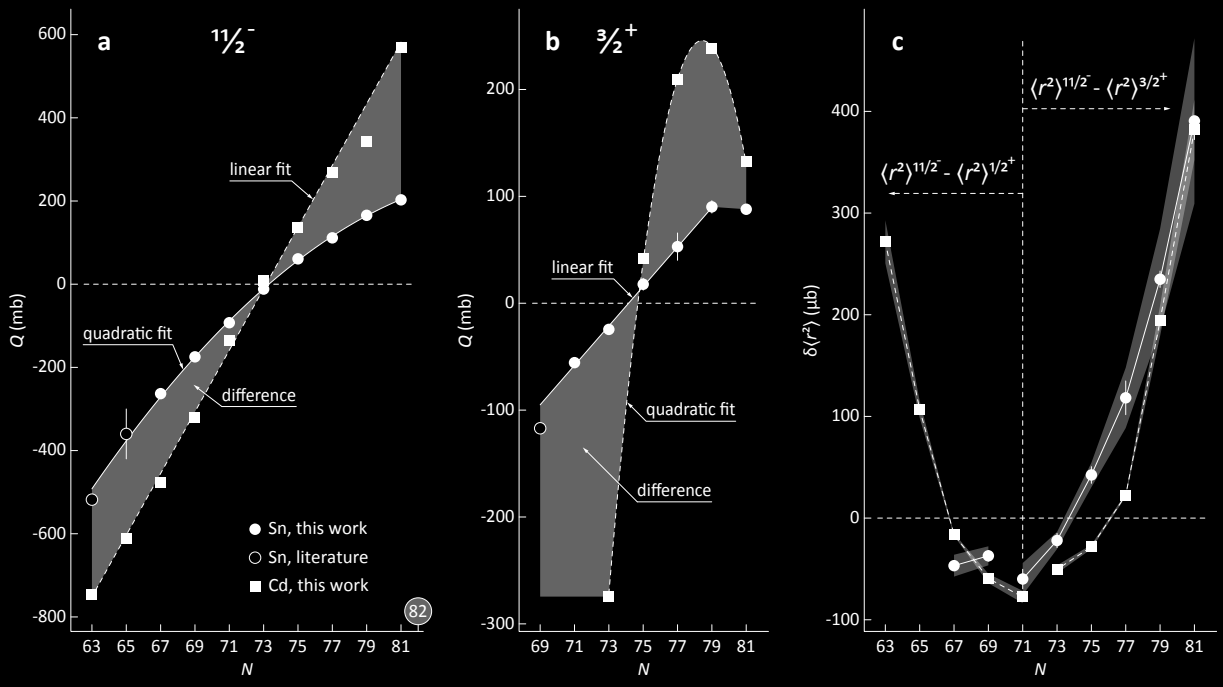

Figure 2. Sn vs. Cd: a, $11/2^-$ quadrupole moments; b, $3/2^+$ quadrupole moments; c, mean square charge-radii changes for the $11/2^-$ states relative to the $1/2^+$ ($N \leq 71$) and $3/2^+$ ($N \geq 71$) states. The empty markers correspond to short-lived states measured with other techniques [52].

suitable transitions deep in the ultraviolet spectrum, such as antimony [48]. The paper is focused on the electric quadrupole moments of the $11/2^-$ states, represented by the squares in Fig. 2a. These compose the longest known to date sequence of linearly aligned quadrupole moments. It is worth pointing out before comparison with tin [46], that the expression C.6 used to convert the measured hyperfine parameters to moments incorporates an electric-field gradient derived from Dirac-Hartree-Fock calculations. Subsequent measurements and calculations in the neutral atom of cadmium [49] support the experimental findings in the ion.

The $11/2^-$ quadrupole moments are compared with the linear expression B.11, which in the seniority scheme [12] corresponds to the lowest value $v = 1$ of the seniority quantum number. Higher seniorities are dismissed on the basis of tabulated fractional-parentage coefficients [50], as these would contradict the observed gradient in Fig. 2a. The linearity and the intercept in the middle of the trend are naturally explained in the seniority scheme. The alignment of ten quadrupole moments, however, is not. Generalized seniority is not discussed. Instead, a naive picture suggesting delayed filling of the unique-parity $h_{11/2}$ orbital due to a shell degeneracy is proposed. The $3/2^+$ states in Fig. 2b show parabolic, thus, less simplistic behaviour. The paper correctly associates nearly half of the observed quadrupole moments with proton polarizability on the $g_{9/2}$ orbital, later confirmed in the framework of covariant density functional theory [51].

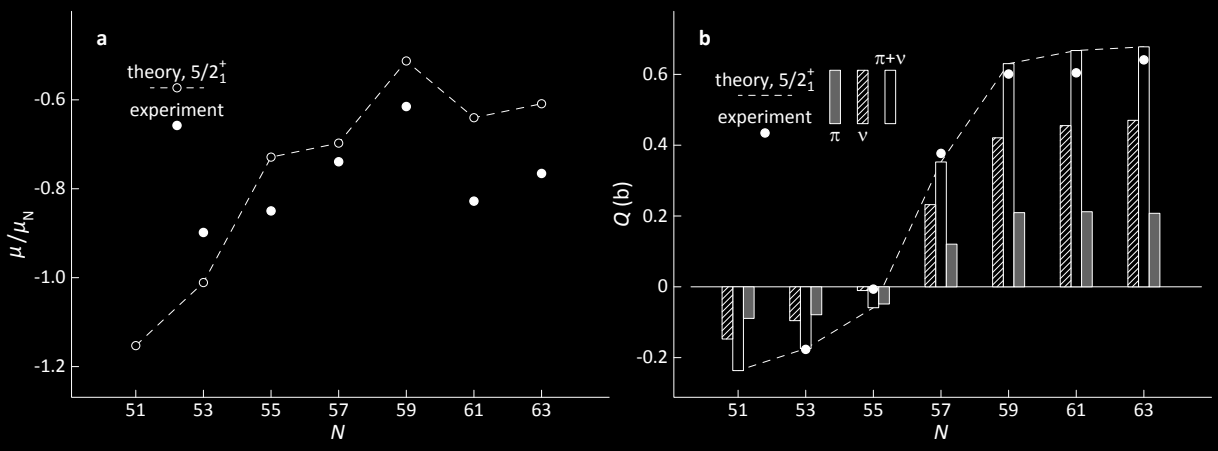

Figure 3. Electromagnetic moments of the neutron-deficient cadmium isotopes compared with theoretical values. The data at ^{111}Cd are taken from the literature [53, 54].

"Simple nuclear structure in $^{111\text{-}129}$Cd from atomic isomer shifts" [44] reports the first observation of a parabolic mass dependence of the atomic isomer shift C.11, and therefore of the nuclear isomeric mean square charge-radii changes. The result is shown with the squares in Fig. 2c. It is proposed that this parabolic trend derives directly from the linear behaviour of the $11/2^-$ quadrupole moments. In principle, the mean square charge radius follows the squared quadrupole deformation which is proportional to the spectroscopic quadrupole moment, resulting in an overall quadratic dependence. The paper goes a step further and attempts to establish this connection quantitatively. This simple description, however, uses several assumptions that need to be taken with a grain of salt. Most notable is the use of B.16 which assumes strong coupling. At very small deformations such simple geometrical relations may no longer apply. This issue is countered in the paper by calculating the quadrupole deformation within the covariant density functional theory and a linear mass dependence is indeed confirmed. The trend in Fig. 2c takes negative values in the middle of the shell, which is attributed to a smaller deformation of the positive-parity states due to a weaker proton polarizability. Theoretical description of the quadratic behaviour of the isomer shift is somewhat challenging, as discussed further.

"Spins and electromagnetic moments of $^{101\text{-}109}$Cd" [45] reports on the $5/2^+$ ground states in the neutron-deficient isotopes. Simplistic interpretations are removed from focus. Instead, the moments in Figs. 3a and 3b are compared with large-scale shell-model calculations using a hypothetical ^{88}Sr core [55, 56] and the *m*-scheme parallel-computation code KSHELL [57]. A complex picture emerges towards the middle of the shell where the wave function is found to be very fragmented. Joined filling of the neutron $d_{5/2}$ and $g_{7/2}$ orbitals is found to play a key role for the structure of the $5/2^+$ states, in addition to contributions from 2^+ and 4^+ configurations on the proton $g_{9/2}$ orbital. This conclusion is in line with the expectations set by mean-field calculations [51].

"Structural trends in atomic nuclei from laser spectroscopy of tin" [46] reports the electromagnetic moments and isomeric charge-radii changes along the tin isotopic chain towards $N = 82$. These are compared with the corresponding values in the cadmium isotopes in Fig. 2 where three striking observations are readily made. First, there is a clear departure from simplicity with the closure of the $Z = 50$ proton core in tin, judged by the transition from a linear to a quadratic N dependence over the unique-parity states in Fig. 2a. Second, the curvature in Fig. 2b switches states and becomes strongly quadratic for cadmium and strictly linear for tin. Third, the trends of differential mean square charge radii of tin and cadmium isotopes in Fig 2c are nearly identical. The latter is hard to understand in the simple terms proposed in Ref. [44], as the larger $11/2^-$ quadrupole moments of the cadmium isotopes should have resulted in much greater radii changes relative to the values in tin. Calculations in the framework of density-functional theory demonstrate consistencies with the above-listed features. Further theoretical modelling is anticipated.

The role of atomic theory needs to be discussed. As stated earlier, laser spectroscopy relies on estimated values of electric-field gradients to quote quadrupole moments through the relation C.6. Therefore, any comparison between the trends of tin and cadmium in Figs. 2a and 2b implicitly involves a comparison between two calculations. The fully relativistic multiconfiguration Dirac-Hartree-Fock method [4, 5] is employed to calculate the electric-field gradient in the relevant states of atomic tin and singly-ionized cadmium. This is essential for the physics case, as it allows to determine with confidence the smaller size of the nuclear quadrupole moment in the tin isotopes. Atomic theory is also used to account for the hyperfine anomaly of the nuclear magnetic moment through the relation C.8.

Quadrupole moments in the literature [58] are found to deviate from reality, partly due to the use of a semi-empirical estimate for the electric-field gradient and, to an extent, because of experimental factors. This discrepancy has modified the conclusions from phenomenological calculations using the generalised-seniority model [59]. Furthermore, the quadratic trend of the unique-parity states of tin is not reproduced. Nonetheless, the generalised seniority, as in Ref. [60], does predict a non-linear filling of the virtual orbitals constructed in the model. Perhaps, future theoretical studies will offer a better agreement with the latest results from laser spectroscopy. An open question that needs to be addressed experimentally is the behaviour of the analogue states in the tellurium isotopes ($Z = 52$). In the lead region ($Z = 82$), studies with high resolution can shed light on the unique-parity $i_{13/2}$ states whose behaviour may be similar [61].

The radii trends from the aforementioned works are discussed in "From calcium to cadmium: Testing the pairing functional through charge radii measurements of $^{100\text{-}130}$Cd" [62] and "Laser spectroscopy of neutron-rich tin isotopes: A discontinuity in charge radii across the $N = 82$ shell closure" [63]. Density-functional-theory calculations correctly predict the observed odd-even staggering in the former, and the kink at $N = 82$ in the latter.

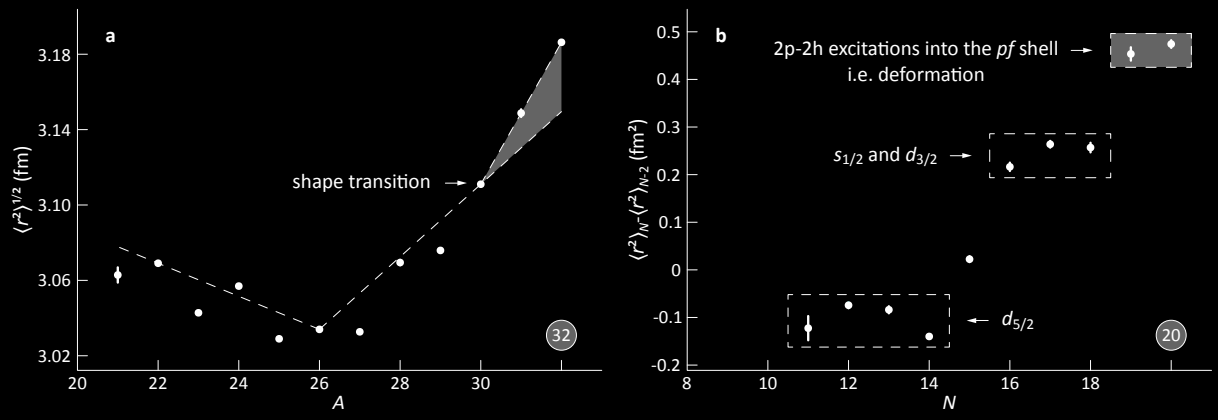

Figure 4. Root mean square charge radii and differential mean square radii changes for the isotopes of magnesium in the *sd* shell.

F. DEFORMATION IN LIGHT NUCLEI

Experimental evidence at the time, such as the unexpected ground-state spin of ^{31}Na [30] determined by the Orsay laser-spectroscopy groups, prompted Wildenthal and Chung to discuss a "collapse of the conventional shell-model ordering in the very-neutron-rich isotopes of Na and Mg" [64]. A shape transition had been previously proposed [65], which favours the filling of the pf shell at large prolate deformations before the sd shell is complete. The subject remained at the forefront of nuclear research for decades, with laser spectroscopy playing a prominent role [66]. Yet, the transition to a deformed configuration in the magnesium isotopes had not been directly observed, with spins zero and a half in the relevant isotopes being a major obstacle due to the non-existence of a quadrupole moment. This issue is resolved in the following.

"Nuclear charge radii of $^{21\text{-}32}$Mg" [67] examines the full range of magnesium isotopes in the sd shell. In principle, by means of integrating B.9 for the parametrisation B.13 averaged over time, the charge radius acquires a dependence on the quadrupole deformation, which can be studied. Three "modes" of the nuclear charge radius are observed in Fig. 4a as variations in the gradient, demonstrated also in the derivative plot 4b. The kink/step at $N = 14$ signifies the completion of the $d_{5/2}$ shell. Towards $N = 8$ strong α-type correlations involving the four valence protons in magnesium result in cluster configurations and large radii. An additional kink/step appears in the opposite direction, two units before $N = 20$, signifying the long-anticipated shape transition in light nuclei. Overall, fine details of the neutron sd shell are revealed as features in the radii trend, produced by the specific proton polarizability associated with each neutron orbital. These are only observable with high experimental resolution, as the underlined isotope shifts are measured with a precision of better than a ‰. The experimental results are discussed in the theoretical framework of fermionic molecular dynamics.

G. OUTLOOK

The reoccurring theme in the summarized works is: mass-dependent trends of nuclear quantities revealed at high experimental precision. It is rather the neutron dimension N which is scrutinized in collinear laser spectroscopy, due to the laser wavelength being tied to a chemical element and its isotopes. The proton dimension is currently being exploited by in-source spectroscopy in somewhat lower resolution [68]. In general, since the protons carry the nuclear charge, simplistic trends of nuclear electromagnetic observables will show substantial effects, albeit for a smaller number of cases; the latter reflecting the fact that isotonic chains are generally shorter due to the Coulomb repulsion. Systematic uncertainties will arise as a result of inaccuracies in electric-field gradients and electronic factors associated with each chemical element. Without consistent atomic calculations, the issue will be difficult to overcome. With regard to the measurements on cadmium, Haas *et al.* discuss "Quadrupole moments of Cd and Zn nuclei: When solid-state, molecular, atomic, and nuclear theory meet" [54]. The importance of the spectroscopy on tin presented here, and its accurate calibration with contemporary atomic calculations, is yet to be put into a perspective.

H. CURRICULUM VITAE

	Deyan Todorov Yordanov (1978)
2002	M.Sc. in theoretical and mathematical Physics
2007	Ph.D. in nuclear Physics
2013	CNRS
unit	Institut de Physique Nucléaire d'Orsay
e-mail	yordanov@ipno.in2p3.fr
address	15 rue Georges Clémenceau, 91406 Orsay, France
tel.	+33 169 153 307
publons	C-3187-2015
ORCID	0000-0002-1592-7779

2019	CERN scientific associate
2012-2013	MPI-K
2010-2012	CERN fellow
2008-2009	MPI-K
2007-2008	University of Mainz
2003-2007	KU Leuven
1997-2002	Sofia University

[1] H. Poincaré, *Les méthodes nouvelles de la mécanique céleste*, Vol. 1 (Gauthier-Villars et fils, 1892).

[2] N. C. Stone and N. W. C. Leigh, "A statistical solution to the chaotic, non-hierarchical three-body problem," Nature **576**, 406 (2019).

[3] R. A. Kerr, "It's official-Voyager has left the solar system," Science **341**, 1158 (2013).

[4] C. Froese Fischer, M. Godefroid, T. Brage, P. Jönsson, and G. Gaigalas, "Advanced multiconfiguration methods for complex atoms: I. energies and wave functions," J. Phys. B **49**, 182004 (2016).

[5] I. P. Grant, *Relativistic Quantum Theory of Atoms and Molecules. Theory and Computation* (Springer-Verlag, New York, USA, 2007).

[6] S. R. Beane, E. Chang, S. Cohen, W. Detmold, H. W. Lin, K. Orginos, A. Parreño, M. J. Savage, and B. C. Tiburzi, "Magnetic moments of light nuclei from lattice quantum chromodynamics," Phys. Rev. Lett. **113**, 252001 (2014).

[7] I. Talmi, "The shell model - simplicity from complexity: some of my best nuclei are spherical," Phys. Scr. **92**, 083001 (2017).

[8] C. A. de Coulomb, *Premier mémoire sur l'électricité et le magnétisme* (Histoire de l'Académie Royale des Sciences. Imprimerie Royale., Paris, 1785) pp. 569–577.

[9] M. G. Mayer and J. H. D. Jensen, *Elementary Theory of Nuclear Shell Structure* (John Wiley & Sons, Inc., New York, 1955).

[10] P. Van Isacker, "Partial and quasi dynamical symmetries in nuclei," Nucl. Phys. News **24**, 23 (2014).

[11] R. F. Casten, *Nuclear Structure from a Simple Perspective* (Oxford University Press, New York, 1990).

[12] I. Talmi, *Simple Models of Complex Nuclei* (Harwood Academic Publishers, Switzerland, 1993).

[13] P. Ring and P. Schuck, *The Nuclear Many-Body Problem* (Springer-Verlag, Berlin, Heidelberg, 1980).

[14] CODATA recommended values of the fundamental physical constants: 2018.

[15] B. Castel and I. S. Towner, *Modern Theories of Nuclear Moments* (Clarendon Press, Oxford, 1990).

[16] B. A. Brown, N. J. Stone, J. R. Stone, I. S. Towner, and M. Hjorth-Jensen, "Magnetic moments of the 2_1^+ states around ^{132}Sn," Phys. Rev. C **71**, 044317 (2005).

[17] L. Coraggio, L. De Angelis, T. Fukui, A. Gargano, N. Itaco, and F. Nowacki, "Renormalization of the Gamow-Teller operator within the realistic shell model," Phys. Rev. C **100**, 014316 (2019).

[18] G. Fricke, C. Bernhardt, K. Heilig, L. A. Schaller, L. Schellenberg, E. B. Shera, and C. W. Dejager, "Nuclear ground state charge radii from electromagnetic interactions," At. Data Nucl. Data Tables **60**, 177 (1995).

[19] K. Heyde, *The Nuclear Shell Model* (Springer-Verlag, Berlin Heidelberg, 1994).

[20] A. Bohr and B. R. Mottelson, *Nuclear Structure*, Vol. 2 (W. A. Benjamin, Inc., 1975).

[21] D. L. Hill and J. A. Wheeler, "Nuclear constitution and the interpretation of fission phenomena," Phys. Rev. **89**, 1102 (1953).

[22] H. Kopfermann, *Nuclear Moments* (Academic Press Inc., New York, 1958).

[23] P. C. Magnante and H. H. Stroke, "Isotope shift between ^{209}Bi and 6.3-day ^{206}Bi," J. Opt. Soc. Am. **59**, 836 (1969).

[24] W. H. King, "Comments on the article "Peculiarities of the isotope shift in the samarium spectrum"," J. Opt. Soc. Am. **53**, 638 (1963).

[25] A. Klose, K. Minamisono, Ch. Geppert, N. Frömmgen, M. Hammen, J. Krämer, A. Krieger, C. D. P. Levy, P. F. Mantica, W. Nörtershäuser, and S. Vinnikova, "Tests of atomic charge-exchange cells for collinear laser spectroscopy," Nucl. Instrum. Methods Phys. Res., Sect. A **678**, 114 (2012).

[26] R. Neugart, J. Billowes, M. L. Bissell, K. Blaum, B. Cheal, K. T. Flanagan, G. Neyens, W. Nörtershäuser, and D. T. Yordanov, "Collinear laser spectroscopy at ISOLDE: new methods and highlights," J. Phys. G **44**, 064002 (2017).

[27] K. Blaum, J. Dilling, and W. Nörtershäuser, "Precision atomic physics techniques for nuclear physics with radioactive beams," Phys. Scr. **T152**, 014017 (2013).

[28] P. Campbell, I. D. Moore, and M. R. Pearson, "Laser spectroscopy for nuclear structure physics," Prog. Part. Nucl. Phys. **86**, 127 (2016).

[29] G. Huber, C. Thibault, R. Klapisch, H. T. Duong, J. L. Vialle, J. Pinard, P. Juncar, and P. Jacquinot, "High-resolution laser spectroscopy of the D lines of on-line produced $^{21,\,22,\,24,\,25}$Na using a new high-sensitivity method of detection of optical resonances," Phys. Rev. Lett. **34**, 1209 (1975).

[30] G. Huber, F. Touchard, S. Büttgenbach, C. Thibault, R. Klapisch, H. T. Duong, S. Liberman, J. Pinard, J. L. Vialle, P. Juncar, and P. Jacquinot, "Spins, magnetic moments, and isotope shifts of $^{21\text{-}31}$Na by high resolution laser spectroscopy of the atomic D_1 line," Phys. Rev. C **18**, 2342 (1978).

[31] J. Sauvage, N. Boos, L. Cabaret, J. E. Crawford, H. T. Duong, J. Genevey, M. Girod, G. Huber, F. Ibrahim, M. Krieg, F. Le Blanc, J. K. P. Lee, J. Libert, D. Lunney, J. Obert, J. Oms, S. Péru, J. Pinard, J. C. Putaux, B. Roussière, V. Sebastian, D. Verney, S. Zemlyanoi, J. Arianer, N. Barré, M. Ducourtieux, D. Forkel-Wirth, G. Le Scornet, J. Lettry, C. Richard-Serre, and C. Véron, "COMPLIS experiments: COllaboration for spectroscopy Measurements using a Pulsed Laser Ion Source," Hyp. Interact. **129**, 303 (2000).

[32] F. Le Blanc, J. Obert, J. Oms, J. C. Putaux, B. Roussière, J. Sauvage, J. Pinard, L. Cabaret, H. T. Duong, G. Huber, M. Krieg, V. Sebastian, J. Crawford, J. K. P. Lee, J. Genevey, and F. Ibrahim, "Nuclear moments and deformation change in ^{184}Au^{g,m} from laser spectroscopy," Phys. Rev. Lett. **79**, 2213 (1997).

[33] F. Le Blanc, D. Lunney, J. Obert, J. Oms, J. C. Putaux, B. Roussière, J. Sauvage, S. Zemlyanoi, J. Pinard, L. Cabaret, H. T. Duong, G. Huber, M. Krieg, V. Sebastian, J. E. Crawford, J. K. P. Lee, M. Girod, S. Péru, J. Genevey, and J. Lettry, "Large odd-even radius staggering in the very light platinum isotopes from laser spectroscopy," Phys. Rev. C **60**, 054310 (1999).

[34] D. Verney, L. Cabaret, J. E. Crawford, H. T. Duong, B. Fricke, J. Genevey, G. Huber, F. Ibrahim, M. Krieg, F. Le Blanc, J. K. P. Lee, G. Le Scornet, D. Lunney, J. Obert, J. Oms, J. Pinard, J. C.

Puteaux, K. Rashid, B. Roussière, J. Sauvage, and V. Sebastian, "Deformation change in light iridium nuclei from laser spectroscopy," Eur. Phys. J. A **30**, 489 (2006).

[35] F. Le Blanc, L. Cabaret, E. Cottereau, J. E. Crawford, S. Essabaa, J. Genevey, R. Horn, G. Huber, J. Lassen, J. K. P. Lee, G. Le Scornet, J. Lettry, J. Obert, J. Oms, A. Ouchrif, J. Pinard, H. Ravn, B. Roussière, J. Sauvage, and D. Verney, "Charge-radius change and nuclear moments in the heavy tin isotopes from laser spectroscopy: Charge radius of ^{132}Sn," Phys. Rev. C **72**, 034305 (2005).

[36] R. Sifi, F. Le Blanc, N. Barré, L. Cabaret, J. Crawford, M. Ducourtieux, S. Essabaa, J. Genevey, G. Huber, M. Kowalska, C. Lau, J. K. P. Lee, G. Le Scornet, J. Oms, J. Pinard, B. Roussière, J. Sauvage, M. Seliverstov, and H. Stroke, "Laser spectroscopy measurements of neutron-rich tellurium isotopes by COMPLIS," Hyp. Interact. **171**, 173 (2006).

[37] J. K. P. Lee, G. Savard, J. E. Crawford, G. Thekkadath, H. T. Duong, J. Pinard, S. Liberman, F. Le Blanc, P. Kilcher, J. Obert, J. Oms, J. C. Putaux, B. Roussière, and J. Sauvage, "Resonant ionization spectroscopy of laser-desorbed gold isotopes," AIP Conf. Proc. **164**, 205 (1987).

[38] J. K. P. Lee, G. Savard, J. E. Crawford, G. Thekkadath, H. T. Duong, J. Pinard, S. Liberman, F. Le Blanc, P. Kilcher, J. Obert, J. Oms, J. C. Putaux, B. Roussière, and J. Sauvage, "Charge-radius changes in even-*A* platinum nuclei," Phys. Rev. C **38**, 2985 (1988).

[39] H. T. Duong, J. Pinard, S. Liberman, G. Savard, J. K. P. Lee, J. E. Crawford, G. Thekkadath, F. Le Blanc, P. Kilcher, J. Obert, J. Oms, J. C. Putaux, B. Roussière, and J. Sauvage, "Shape transition in neutron deficient Pt isotopes," Phys. Lett. B **217**, 401 (1989).

[40] F. Ibrahim, D. Verney, M. Lebois, B. Roussière, S. Essabaa, S. Franchoo, S. Gales, D. Guillemaud Mueller, C. Lau, F. Le Blanc, J.F. Le Du, M.C. Mhamed, A.C. Mueller, and J. Sauvage, "The ALTO facility at IPN Orsay and study of neutron rich nuclei in the vincinity of ^{78}Ni," Nucl. Phys. **A787**, 110 (2007).

[41] DESIR: the SPIRAL2 low-energy beam facility (2009), Technical proposal for SPIRAL2 instrumentation.

[42] D. T. Yordanov, D. Atanasov, M. L. Bissell, S. Franchoo, G. Georgiev, A. Kanellakopoulos, S. Lechner, E. Minaya Ramirez, D. Nichita, L. V. Rodríguez, and A. Said, "Instrumentation for high-resolution laser spectroscopy at the alto radioactive-beam facility," J. Instrum. (2020), in review.

[43] D. T. Yordanov, D. L. Balabanski, J. Bieroń, M. L. Bissell, K. Blaum, I. Budinčević, S. Fritzsche, N. Frömmgen, G. Georgiev, Ch. Geppert, M. Hammen, M. Kowalska, K. Kreim, A. Krieger, R. Neugart, W. Nörtershäuser, J. Papuga, and S. Schmidt, "Spins, electromagnetic moments, and isomers of $^{107\text{-}129}$Cd," Phys. Rev. Lett. **110**, 192501 (2013).

[44] D. T. Yordanov, D. L. Balabanski, M. L. Bissell, K. Blaum, I. Budinčević, B. Cheal, K. Flanagan, N. Frömmgen, G. Georgiev, Ch. Geppert, M. Hammen, M. Kowalska, K. Kreim, A. Krieger, J. Meng, R. Neugart, G. Neyens, W. Nörtershäuser, M. M. Rajabali, J. Papuga, S. Schmidt, and P. W. Zhao, "Simple nuclear structure in $^{111\text{-}129}$Cd from atomic isomer shifts," Phys. Rev. Lett. **116**, 032501 (2016).

[45] D. T. Yordanov, D. L. Balabanski, M. L. Bissell, K. Blaum, A. Blazhev, I. Budinčević, N. Frömmgen, Ch. Geppert, H. Grawe, M. Hammen, K. Kreim, R. Neugart, G. Neyens, and W. Nörtershäuser, "Spins and electromagnetic moments of $^{101\text{-}109}$Cd," Phys. Rev. C **98**, 011303(R) (2018).

[46] D. T. Yordanov, L. V. Rodríguez, D. L. Balabanski, J. Bieroń, M. L. Bissell, K. Blaum, B. Cheal, J. Ekman, G. Gaigalas, R. F. Garcia Ruiz, G. Georgiev, W. Gins, M. R. Godefroid, C. Gorges, Z. Harman, H. Heylen, P. Jönsson, A. Kanellakopoulos, S. Kaufmann, C. H. Keitel, V. Lagaki, S. Lechner, B. Maaß, S. Malbrunot-Ettenauer, W. Nazarewicz, R. Neugart, G. Neyens, W. Nörtershäuser, N. S. Oreshkina, A. Papoulia, P. Pyykkö, P.-G. Reinhard, S. Sailer, R. Sánchez, S. Schiffmann, S. Schmidt, L. Wehner, C. Wraith, L. Xie, Z. Xu, and X. Yang, "Structural trends in atomic nuclei from laser spectroscopy of tin," Comm. Phys. (2020), accepted.

[47] J. Wood, "Viewpoint: Simple structure in complex nuclei," Physics **6**, 52 (2013).

[48] Z. Y. Xu, D. T. Yordanov, D. L. Balabanski, J. Billowes, M. L. Bissell, K. Blaum, B. Cheal, S. Malbrunot-Ettenauer, S. Franchoo, R. F. Garcia Ruiz, G. Georgiev, W. Gins, C. Gorges, H. Heylen, A. Koszorús, S. Kaufmann, J. Krämer, M. Kowalska, G. Neyens, R. Neugart, L. V. Rodríguez, W. Nörtershäuser, R. Sánchez, C. Wraith, L. Xie, and X. F. Yang, "Nuclear quadrupole moments and charge radii of the $_{51}$Sb isotopes via collinear laser spectroscopy," CERN-INTC-2016-054, INTC-P-484 (2016).

[49] N. Frömmgen, D. L. Balabanski, J. Bieroń, M. L. Bissell, K. Blaum, B. Cheal, Flanagan K., S. Fritzsche, Ch. Geppert, M. Hammen, M. Kowalska, K. Kreim, A. Krieger, R. Neugart, G. Neyens, M. Rajabali, W. Nörtershäuser, J. Papuga, and D. T. Yordanov, "Collinear laser spectroscopy of atomic cadmium," Eur. Phys. J. D **69**, 164 (2015).

[50] B. F. Bayman and A. Lande, "Tables of identical-particle fractional parentage coefficients," Nucl. Phys. **77**, 1 (1966).

[51] P. W. Zhao, S. Q. Zhang, and J. Meng, "Explanation of the simplicity of the quadrupole moments recently observed in Cd isotopes from covariant density functional theory," Phys. Rev. C **89**, 011301(R) (2014).

[52] H. Haas, (2019), private communication.

[53] H. Bertschat, H. Haas, F. Pleiter, E. Recknagel, E. Schlodder, and B. Spellmeyer, "Temperature dependence of the knight shift for cadmium in palladium," Z. Phys. **270**, 203 (1974).

[54] H. Haas, S. P. A. Sauer, L. Hemmingsen, V. Kellö, and P. W. Zhao, "Quadrupole moments of Cd and Zn nuclei: When solid-state, molecular, atomic, and nuclear theory meet," Europhysics Lett. **117**, 62001 (2017).

[55] T. Faestermann, M. Górska, and H. Grawe, "The structure of ^{100}Sn and neighbouring nuclei," Prog. Part. Nucl. Phys. **69**, 85 (2013).

[56] O. Kavatsyuk, C. Mazzocchi, Z. Janas, A. Banu, L. Batist, F. Becker, A. Blazhev, W. Brüchle, J. Döring, T. Faestermann, M. Górska, H. Grawe, A. Jungclaus, M. Karny, M. Kavatsyuk, O. Klepper, R. Kirchner, M. La Commara, K. Miernik, I. Mukha, C. Plettner, A. Płochocki, E. Roeckl, M. Romoli, K. Rykaczewski, M. Schädel, K. Schmidt, R. Schwengner, and J. Żylicz, "Beta decay of ^{101}Sn," Eur. Phys. J. A **31**, 319 (2007).

[57] N. Shimizu, "Nuclear shell-model code for massive parallel computation, KSHELL," arXiv:1310.5431 [nucl-th] (2013).

[58] M. Anselment, K. Bekk, A. Hanser, H. Hoeffgen, G. Meisel, S. Göring, H. Rebel, and G. Schatz, "Charge radii and moments of tin nuclei by laser spectroscopy," Phys. Rev. C **34**, 1052 (1986).

[59] B. Maheshwari, H. Abu Kassim, N. Yusof, and A. K. Jain, "Evolution of nuclear structure in and around $Z = 50$ closed shell: Generalized Seniority in Cd, Sn and Te isotopes," Nucl. Phys. **A992**, 121619 (2019).

[60] I. O. Morales, P. Van Isacker, and I. Talmi, "Generalized seniority and E2 transitions in the tin isotopes," Phys. Lett. B **703**, 606 (2011).

[61] G. Neyens, "Nuclear magnetic and quadrupole moments for nuclear structure research on exotic nuclei," Rep. Prog. Phys. **66**, 633 (2003).

[62] M. Hammen, W. Nörtershäuser, D. L. Balabanski, M. L. Bissell, K. Blaum, I. Budinčević, B. Cheal, K. T. Flanagan, N. Frömmgen, G. Georgiev, Ch. Geppert, M. Kowalska, K. Kreim, A. Krieger, W. Nazarewicz, R. Neugart, G. Neyens, J. Papuga, P.-G. Reinhard, M. M. Rajabali, S. Schmidt, and D. T. Yordanov, "From calcium to cadmium: Testing the pairing functional through charge radii measurements of $^{100\text{-}130}$Cd," Phys. Rev. Lett. **121**, 102501 (2018).

[63] C. Gorges, L. V. Rodríguez, D. L. Balabanski, M. L. Bissell, K. Blaum, B. Cheal, R. F. Garcia Ruiz, G. Georgiev, W. Gins, H. Heylen, A. Kanellakopoulos, S. Kaufmann, M. Kowalska, V. Lagaki, S. Lechner, B. Maaß, S. Malbrunot-Ettenauer, W. Nazarewicz, R. Neugart, G. Neyens, W. Nörtershäuser, P.-G. Reinhard, S. Sailer, R. Sánchez, S. Schmidt, L. Wehner, C. Wraith, L. Xie, Z. Y. Xu, X. F. Yang, and D. T. Yordanov, "Laser spectroscopy of neutron-rich tin isotopes: A discontinuity in charge radii across the $N = 82$ shell closure," Phys. Rev. Lett. **122**, 192502 (2019).

[64] B. H. Wildenthal and W. Chung, "Collapse of the conventional shell-model ordering in the very-neutron-rich isotopes of Na and Mg," Phys. Rev. C **22**, 2260 (1980).

[65] X. Campi, H. Flocard, A.K. Kerman, and S. Koonin, "Shape transition in the neutron rich sodium isotopes," Nucl. Phys. **A251**, 193 (1975).

[66] G. Neyens, "Multiparticle-multihole states in ^{31}Mg and ^{33}Mg: A critical evaluation," Phys. Rev. C **84**, 064310 (2011).

[67] D. T. Yordanov, M. L. Bissell, K. Blaum, M. De Rydt, Ch. Geppert, M. Kowalska, J. Krämer, K. Kreim, A. Krieger, P. Lievens, T. Neff, R. Neugart, G. Neyens, W. Nörtershäuser, R. Sánchez, and P. Vingerhoets, "Nuclear charge radii of $^{21\text{-}32}$Mg," Phys. Rev. Lett. **108**, 042504 (2012).

[68] R. Ferrer, A. Barzakh, B. Bastin, R. Beerwerth, M. Block, P. Creemers, H. Grawe, R. de Groote, P. Delahaye, X. Fléchard, S. Franchoo, S. Fritzsche, L.P. Gaffney, L. Ghys, W. Gins, C. Granados, R. Heinke, L. Hijazi, M. Huyse, T. Kron, Yu. Kudryavtsev, M. Laatiaoui, N. Lecesne, M. Loiselet, F. Lutton, I.D. Moore, Y. Martínez, E. Mogilevskiy, P. Naubereit, J. Piot, S. Raeder, S. Rothe, H. Savajols, S. Sels, V. Sonnenschein, J.-C. Thomas, E. Traykov, C. Van Beveren, P. Van den Bergh, P. Van Duppen, K. Wendt, and A. Zadvornaya, "Towards high-resolution laser ionization spectroscopy of the heaviest elements in supersonic gas jet expansion," Nat. Comm. **8**, 14520 (2017).

Journal of Instrumentation, in review

Prepared for submission to JINST

Instrumentation for high-resolution laser spectroscopy at the ALTO radioactive-beam facility

D. T. Yordanov,[a,b,1] **D. Atanasov,**[b] **M. L. Bissell,**[c] **S. Franchoo,**[a] **G. Georgiev,**[d] **A. Kanellakopoulos,**[e] **S. Lechner,**[b,f] **E. Minaya Ramirez,**[a] **D. Nichita,**[g,h] **L. V. Rodríguez**[i] **and A. Said**[a]

[a] *Institut de Physique Nucléaire, CNRS-IN2P3, Université Paris-Sud, Université Paris-Saclay Orsay, France*

[b] *Experimental Physics Department, CERN Geneva, Switzerland*

[c] *School of Physics and Astronomy, The University of Manchester Manchester, United Kingdom*

[d] *CSNSM, CNRS-IN2P3, Université Paris-Sud, Université Paris-Saclay Orsay, France*

[e] *Instituut voor Kern- en Stralingsfysica, KU Leuven Leuven, Belgium*

[f] *Technische Universität Wien Vienna, Austria*

[g] *ELI-NP, Horia Hulubei National Institute for R&D in Physics and Nuclear Engineering Magurele, Romania*

[h] *Doctoral School in Engineering and Applications of Lasers and Accelerators, University Polytechnica of Bucharest, Bucharest, Romania*

[i] *Max-Planck-Institut für Kernphysik Heidelberg, Germany*

E-mail: Deyan.Yordanov@cern.ch

Abstract: Collinear laser spectroscopy is one of the essential tools for nuclear-structure studies. It allows nuclear electromagnetic properties of ground and isomeric states to be extracted with high experimental precision. Radioactive-beam facilities worldwide strive to introduce such capabilities or to improve existing ones. Here we present the implementation of collinear laser spectroscopy at the ALTO research laboratory, along with data from successful off-line commissioning using sodium beam. The instrumental constituents are discussed with emphasis on simple technical solutions and maximized use of standard equipment. Potential future applications are outlined.

Keywords: collinear laser spectroscopy, atomic hyperfine structure;

[1] Corresponding author.

Contents

1 Introduction

Laser spectroscopy is an experimental technique probing the energy levels of the atomic hyperfine structure induced by the nuclear electromagnetic properties [1]. Root mean square charge-radii changes, magnetic-dipole and electric-quadrupole moments of a nucleus are the quantities typically assessed. Atomic beams with well-defined energy of the order of tens of keV in combination with narrow-band lasers facilitate high-resolution measurements limited essentially by the lifetime broadening.[1] The relativistic Doppler effect:

$$\nu = \nu_0(1 - \beta\cos\phi)/\sqrt{1-\beta^2}$$

is used, where ϕ is the angle between the propagation direction of the laser radiation and the velocity $\vec{v}$ of the atomic beam ($\beta = |\vec{v}|/c$), and takes values of $\phi = 0$ and $\phi = 2\pi$ radians for collinear and anti-collinear geometry, respectively. The Doppler-shifted frequency ν is scanned to match the transitions of the hyperfine structure by varying the velocity $|\vec{v}|$ while the laser frequency ν_0 is kept constant, or vice versa. In most cases, measurements are implemented on atomic states, which require neutralisation [2] of the singly-ionized beams used for acceleration. Resonant laser excitations are detectable by various means [3]. A comprehensive overview of the technique and its existing implementations can be found in dedicated reviews [4, 5]. The following outlines the newly-constructed collinear-laser-spectroscopy setup at the ALTO facility [6].

2 Instrumentation

Figure 1 shows a technical drawing of the associated vacuum beamline. Due to space limitations in the experimental hall, the realised assembly is relatively compact, with a total length of 3.8 m. The instrument is commissioned by measurements in the D_1 line of ^{23}Na, as shown in Fig. 2. A brief technical description of the instrumentation is presented below.

[1] The natural linewidth in angular frequency is inversely proportional to the lifetime of the excited state: $\Gamma = \tau^{-1}$.

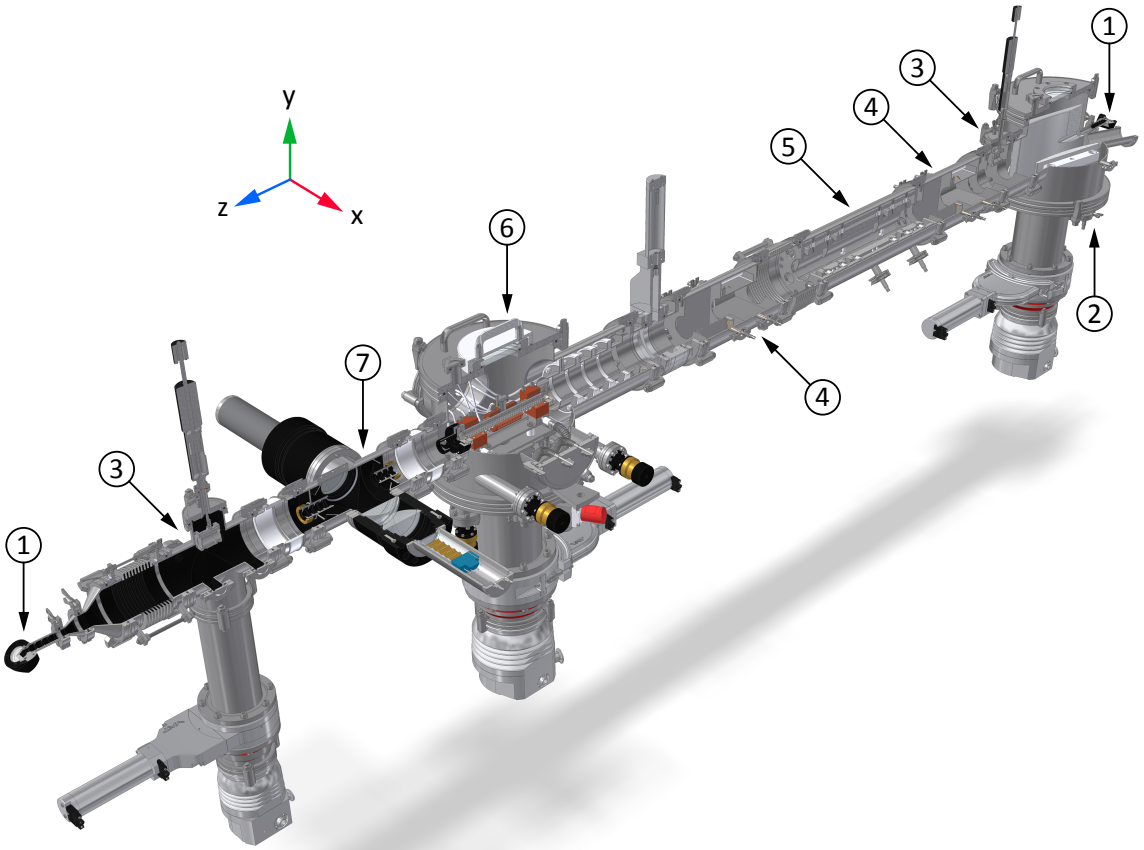

Figure 1. **Vacuum beamline.** Technical drawing with a 90° longitudinal cross section: 1.) Fused-silica windows at Brewster's angle; 2.) 20° bender for laser and ion-beam overlap; 3.) Faraday cups; 4.) Electrostatic x-y deflectors; 5.) Electrostatic quadrupole triplet; 6.) Post-acceleration and charge-exchange chamber; 7.) Optical detection; Total length: 3.8 m.

Merging bender A cylindrical bender with a radius of 800 mm, a gap of 60 mm, and a height of 180 mm facilitates a 20° rotation of the ion beam. The laser beam penetrates the outer electrode collinearly to the ion beam through an opening of 20 mm in diameter. The bending voltage requirement per unit beam energy is 0.15 V/eV. Windows of fused silica at Brewster's angle of 55.5°, each including a set of apertures, are installed at both ends of the instrument.

Electrostatic ion optics The bender is followed by a section for ion-beam handling comprising a Faraday cup, two x-y deflectors, and a non-steering quadrupole triplet in between, namely the model EQT 64-15 by NEC. The latter is tuned in conjunction with a quadrupole lens [7] in the preceding section of beamline to achieve maximum transmission to the second Faraday cup.

Post-acceleration chamber Chamber 6 in Fig. 1 is specific to collinear laser spectroscopy and conceptually similar to existing instrumentation [2, 3]. A five-cylinder electrostatic lens with elements of 40 × 80 mm in length and diameter, separated by 12-mm thick insulators, is used for

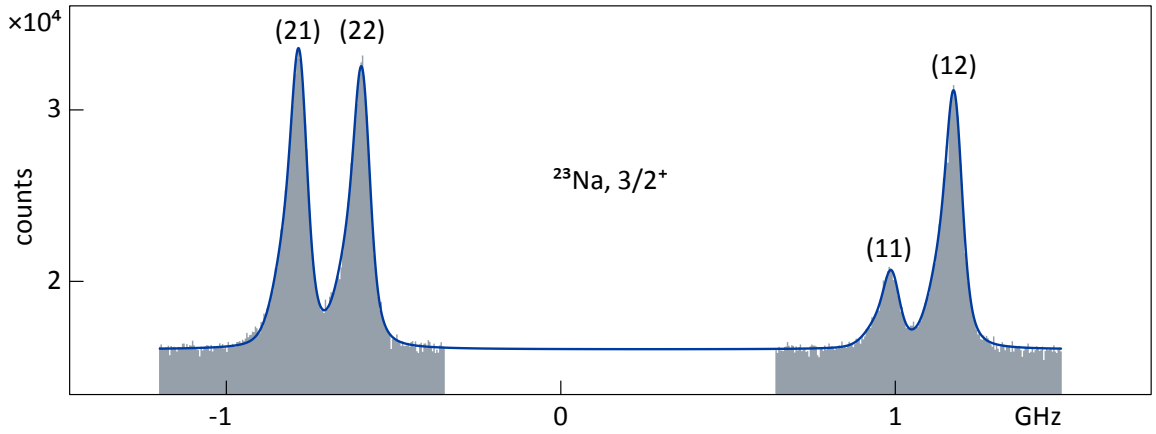

Figure 2. **Fluorescence spectrum of the D_1 line in ^{23}Na ($I^\pi = 3/2^+$).** Each transition is denoted in parentheses by the total angular-momentum quantum numbers of the lower and the higher state, respectively. The frequency scale is relative to the fine-structure splitting.

modification of the ion-beam energy. The post-acceleration potential is linearly distributed with a voltage divider. Optionally, the first three elements may also be operated as an Einzel lens to obtain an additional handle on the ion-beam focusing. A hot cell for vaporizing alkali metals is held at the post-acceleration potential. For use with sodium vapour on a sodium ion beam, its central region of 80 mm in length is heated to about 270°C to achieve 50% neutralization. A floating power supply FPD-40-008-10 by ISEG, matched to a THERMOCOAX 1 NcAc heating wire, is used for the purpose. A heating and cooling oil circulator LAUDA-ECO-RE-630-GN maintains both ends at a constant temperature of just a couple of degrees above the melting point, hence at a 100°C for sodium. Apertures of 8 mm contain the molten metal within the cell while obstructing the propagation of stray light.

Optical detection Two telescopes of aspheric lenses positioned in the horizontal plane image the ion-beam fluorescence onto the faceplates of photomultiplier tubes. Longitudinal aperture arrays down to 8 mm at the entrance and 12 mm at the exit reduce the background from laser scattering. All internal surfaces are painted in colloidal graphite. The lenses AL100100-328-SP by THORLABS with a diameter of 100 mm are custom made from ultra-violet grade fused silica with a focal length from the flat surface of 76.2 mm at a wavelength of 328 nm. The assembly is designed with spacer rings which allows adjusting the focal distance in steps of 5 mm to accommodate wavelengths in the range from 200 nm to 1 μm. Head-on photomultiplier tubes for single-photon counting are used, such as the 51-mm (2″) model 9829QSA from ET with domed quartz windows, magnetic shielding, and a specified dark count rate of less than 300 Hz.

Control and data acquisition Analogue and digital voltage input-output is implemented using PXI express electronic modules from NATIONAL INSTRUMENTS. A four-quadrant source and measure unit type 4137 provides a scanning potential, software limited to ±10 V, with high stability and low ripple. The actual post-acceleration voltage is produced by a ±10-kV four-quadrant fast amplifier 10/10B-HS-H-CE from TREK capable of ramping speeds greater than 700 V/μs. A digital multimeter type 4081 is used to monitor and record the applied voltage via an OHM-LABS voltage divider model

KV-10R. During a scan, the multimeter is operated in a 5 1/2-digit mode at 3000 S/s. An ultra-precise 7 1/2-digit mode at 100 S/s is used for independent voltage calibrations. An identical module is available for monitoring the acceleration voltage. The analogue signals of the photomultiplier tubes are converted to low-voltage TTL pulses and read by a timer-counter module type 6612, operated as a 32-bit edge counter. The unit is also capable of digital-signal output for controlling auxiliary equipment. All modules are housed in a type 1082 chassis with an 8840-type controller and currently operated with a user-oriented LabVIEW software.

3 Results of commissioning test

Surface-ionized sodium was accelerated to an energy of 30 keV and subjected to collinear laser spectroscopy in the transition $3s\ ^2S_{1/2} \rightarrow 3p\ ^2P^{\mathrm{o}}_{1/2}$. The required wavelength of 589.8 nm [8] was produced by a cw ring dye laser using Rhodamine 590 in ethylene glycol as the active medium. An example spectrum is shown in Fig. 2 fitted with the empirical lineshape from Ref. [9], which accounts for the asymmetric line broadening from collisional excitations in the hot cell after charge exchange. The full width at half maximum of resonances observed throughout the experiment is about 50 MHz, determined by a substantial Gaussian-like component. Considering the differential Doppler shift of 14.2 MHz/V, the latter could be attributed to a 10^{-4} ripple on the acceleration voltage. For faster transitions, this contribution will be surpassed by the natural linewidth, which in the above transition is only about 10 MHz [10]. A magnetic hyperfine parameter of +885.3(2)(8) MHz is found from the individual fit in Fig. 2. The systematic uncertainty in the second set of parentheses represents the standard deviation of the sample distribution from 26 independent measurements. This result is in line with the value from atomic-beam magnetic resonance [11]. The spectrum in Fig. 2 was obtained in 30 scans of 400 steps, 20 ms each. Laser power of about 1 mW was used on an incident beam of about 300 pA, measured with the first Faraday cup in Fig. 1. The corresponding detection efficiency is one photon in 64000 ions. For faster transitions at the peak of the detector's quantum efficiency of 30%, compared to 2% at the above wavelength, the overall detection efficiency is projected to about 1 : 1000.

4 Perspectives

Collinear laser spectroscopy interlinks several cutting-edge technologies: from the production of exotic beams, to lasers, to high-precision measurement instrumentation. In this context, "off-the-shelf" laser spectroscopy is out of reach, certainly on the isotope production side where dedicated facilities are required. Commercially available user-oriented laser systems, on the other hand, are already being exploited in most existing installations to enhance operations. Likewise, the instrumentation described here has been developed with an emphasis on simple solutions, thus, maximizing the use of standard equipment to reduce cost and development time, and to improve user accessibility. To exploit its full potential, the apparatus needs to be used in conjunction with ion-beam bunching capabilities [12] for background suppression. Techniques such as laser-induced nuclear orientation [13], collisional ionization [14], and state-selective charge exchange [15] may also be considered in specific cases. Possible future applications include studies of nuclear structure or facilitating experiments with polarized beams for decay spectroscopy [16] or research on

fundamental symmetries [17]. The instrument has been constructed along the time-line of the low-energy radioactive beam facility DESIR [18], where dedicated techniques for studies of proton-rich nuclei will be developed.

Acknowledgments

This work has been supported by the Orsay Nuclear Physics Institute, the P2IO Laboratory of Excellence, the French National Institute for Nuclear and Particle Physics, the Paris-Sud University, and the European Union's HORIZON 2020 Program under grant agreement no. 654002. We thank the ALTO technical group for their professional assistance.

Author contributions D.T.Y. initiated the project and contributed in securing financial resources along with S.F., G.G., E.M.R., L.V.R., and other collaborators. Implementation took place under the technical coordination of A.S. M.L.B, A.K., S.L., D.N., L.V.R., and D.T.Y. prepared the instrumentation. D.A. developed the software for data acquisition. All authors contributed to the measurements and the preparation of the manuscript.

Data availability Technical and experimental details are available from the main author upon reasonable request.

References

[1] H. Kopfermann, *Nuclear Moments*. Academic Press Inc., New York, 1958.

[2] A. Klose, K. Minamisono, C. Geppert, N. Frömmgen, M. Hammen, J. Krmer et al., *Tests of atomic charge-exchange cells for collinear laser spectroscopy*, *Nucl. Instrum. Methods Phys. Res., Sect. A* **678** (2012) 114.

[3] R. Neugart et al., *Collinear laser spectroscopy at ISOLDE: New methods and highlights*, *J. Phys. G* **44** (2017) 064002.

[4] K. Blaum, J. Dilling and W. Nörtershäuser, *Precision atomic physics techniques for nuclear physics with radioactive beams*, *Phys. Scr.* **T152** (2013) 014017.

[5] P. Campbell, I. D. Moore and M. R. Pearson, *Laser spectroscopy for nuclear structure physics*, *Prog. Part. Nucl. Phys.* **86** (2016) 127.

[6] F. Ibrahim, D. Verney, M. Lebois, B. Roussière et al., *The ALTO facility at IPN Orsay and study of neutron rich nuclei in the vincinity of* ^{78}*Ni*, *Nucl. Phys.* **A787** (2007) 110.

[7] L. Perrot and H. Cherif, *Beam dynamic into the transfer RIB lines to the DESIR facility at GANIL-SPIRAL2*, in *Proc. 5th International Particle Accelerator Conference (IPAC'14)*, p. 806, 2014. DOI.

[8] P. Juncar, J. Pinard, J. Hamon and A. Chartier, *Absolute determination of the wavelengths of the sodium* D_1 *and* D_2 *lines by using a cw tunable dye laser stabilized on iodine*, *Metrologia* **17** (1981) 77.

[9] D. T. Yordanov et al., *Spin and magnetic moment of* ^{23}*Mg*, *J. Phys. G* **44** (2017) 075104.

[10] U. Volz, M. Majerus, H. Liebel, A. Schmitt and H. Schmoranzer, *Precision lifetime measurements on Na I* $3p\ ^2P_{1/2}$ *and* $3p\ ^2P_{3/2}$ *by beam-gas-laser spectroscopy*, *Phys. Rev. Lett.* **76** (1996) 2862.

[11] A. Beckmann, K. D. Böklen and D. Elke, *Precision measurements of the nuclear magnetic dipole moments of ^{6}Li, ^{7}Li, ^{23}Na, ^{39}K and ^{41}K*, Z. Phys. **270** (1974) 173.

[12] A. Nieminen, P. Campbell, J. Billowes et al., *On-line ion cooling and bunching for collinear laser spectroscopy*, Phys. Rev. Lett. **88** (2002) 094801.

[13] R. Neugart et al., *Precision measurement of ^{11}Li Moments: Influence of halo neutrons on the ^{9}Li core*, Phys. Rev. Lett. **101** (2008) 132502.

[14] W. Geithner, T. Neff et al., *Masses and charge radii of $^{17\text{-}22}$Ne and the two-proton-halo candidate ^{17}Ne*, Phys. Rev. Lett. **101** (2008) 252502.

[15] L. Vermeeren, R. E. Silverans, P. Lievens, A. Klein, R. Neugart, C. Schulz et al., *Ultrasensitive radioactive detection of collinear-laser optical pumping: Measurement of the nuclear charge radius of ^{50}Ca*, Phys. Rev. Lett. **68** (1992) 1679.

[16] Y. Hirayama, T. Shimoda, H. Izumi et al., *Study of ^{11}Be structure through β-delayed decays from polarized ^{11}Li*, Phys. Lett. B **611** (2005) 239.

[17] N. Severijns and O. Naviliat-Cuncic, *Symmetry tests in nuclear beta decay*, Annu. Rev. Nucl. Part. Sci. **61** (2011) 23.

[18] DESIR: the SPIRAL2 low-energy beam facility, Technical proposal for SPIRAL2 instrumentation, 2009.

Spins, Electromagnetic Moments, and Isomers of $^{107-129}$Cd

D. T. Yordanov,[1,2,*] D. L. Balabanski,[3] J. Bieroń,[4] M. L. Bissell,[5] K. Blaum,[1] I. Budinčević,[5] S. Fritzsche,[6] N. Frömmgen,[7] G. Georgiev,[8] Ch. Geppert,[6,7] M. Hammen,[7] M. Kowalska,[2] K. Kreim,[1] A. Krieger,[7] R. Neugart,[7] W. Nörtershäuser,[6,7] J. Papuga,[5] and S. Schmidt[6]

[1]*Max-Planck-Institut für Kernphysik, Saupfercheckweg 1, D-69117 Heidelberg, Germany*
[2]*CERN European Organization for Nuclear Research, Physics Department, CH-1211 Geneva 23, Switzerland*
[3]*INRNE, Bulgarian Academy of Science, BG-1784 Sofia, Bulgaria*
[4]*Instytut Fizyki imienia Mariana Smoluchowskiego, Uniwersytet Jagielloński, Reymonta 4, 30-059 Kraków, Poland*
[5]*Instituut voor Kern-en Stralingsfysica, KU Leuven, Celestijnenlaan 200D, B-3001 Leuven, Belgium*
[6]*GSI Helmholtzzentrum für Schwerionenforschung GmbH, D-64291 Darmstadt, Germany*
[7]*Institut für Kernchemie, Johannes Gutenberg-Universität Mainz, D-55128 Mainz, Germany*
[8]*CSNSM-IN2P3-CNRS, Université de Paris Sud, F-91405 Orsay, France*

(Received 28 January 2013; published 6 May 2013)

The neutron-rich isotopes of cadmium up to the $N = 82$ shell closure have been investigated by high-resolution laser spectroscopy. Deep-uv excitation at 214.5 nm and radioactive-beam bunching provided the required experimental sensitivity. Long-lived isomers are observed in ^{127}Cd and ^{129}Cd for the first time. One essential feature of the spherical shell model is unambiguously confirmed by a linear increase of the $11/2^-$ quadrupole moments. Remarkably, this mechanism is found to act well beyond the $h_{11/2}$ shell.

DOI: 10.1103/PhysRevLett.110.192501 PACS numbers: 21.10.Ky, 21.60.Cs, 31.15.aj, 32.10.Fn

When first proposed, the nuclear shell model was largely justified on the basis of magnetic-dipole properties of nuclei [1]. The electric quadrupole moment could have provided an even more stringent test of the model, as it has a very characteristic linear behavior with respect to the number of valence nucleons [2,3]. However, the scarcity of experimental quadrupole moments at the time did not permit such studies. Nowadays, regardless of experimental challenges, the main difficulty is to predict which nuclei are likely to display this linear signature. The isotopes of cadmium, investigated here, proved to be the most revealing case so far. Furthermore, being in the neighborhood of the "magic" tin, cadmium is of general interest for at least two additional reasons. First, theory relies on nuclei near closed shells for predicting other, more complex systems. Second, our understanding of stellar nucleosynthesis strongly depends on the current knowledge of nuclear properties in the vicinity of the doubly magic tin isotopes [4]. Moreover, specific questions concerning the nuclear structure of the cadmium isotopes require critical evaluation, such as shell quenching [5,6], sphericity [7], deformation [8,9], or whether vibrational nuclei exist at all [10]. Some of these points will be addressed here quite transparently, while others require dedicated theoretical work to corroborate our conclusions. In this Letter we report advanced measurements by collinear laser spectroscopy on the very neutron-rich cadmium isotopes. Electromagnetic moments in these complex nuclei are found to behave in an extremely predictable manner. Yet, their description goes beyond conventional interpretation of the nuclear shell model.

The measurements were carried out with the collinear laser spectroscopy setup at ISOLDE-CERN. High-energy protons impinging on a tungsten rod produced low- to medium-energy neutrons inducing fission in a uranium carbide target. Proton-rich spallation products, such as cesium, were largely suppressed in this manner. Further reduction of surface-ionized isobaric contamination was achieved by the use of a quartz transfer line [11], which allowed the more volatile cadmium to diffuse out of the target while impurities were retained sufficiently long to decay. Cadmium atoms were laser ionized, accelerated to an energy of 30 keV, and mass separated. The ion beam was injected into a gas-filled radio-frequency Paul trap [12] and extracted typically every 100 ms as short bunches with a temporal width of about 5 μs. The ratio of the above time constants equals the factor of background suppression and therefore results in an increase of the overall sensitivity by the square root of that factor ($\approx 10^2$).

The ion of cadmium was excited in the transition: $5s\ ^2S_{1/2} \rightarrow 5p\ ^2P_{3/2}$ at 214.5 nm. Continuous-wave laser light of this wavelength was produced by sequential second-harmonic generation from the output of a titanium-sapphire laser, pumped at 532 nm. The combined fourth-harmonic generation is characterized by a conversion efficiency of up to 2%. Optimal laser power of about 1 mW was supplied for the measurements. Using the ion for laser excitation increased the overall sensitivity by more than an order of magnitude with respect to the neutral atom. The improvement can be accounted for by the faster transition, the higher quantum efficiency of detection, and the absence of ion-beam neutralization. Such establishment of deep-uv laser beams could potentially provide

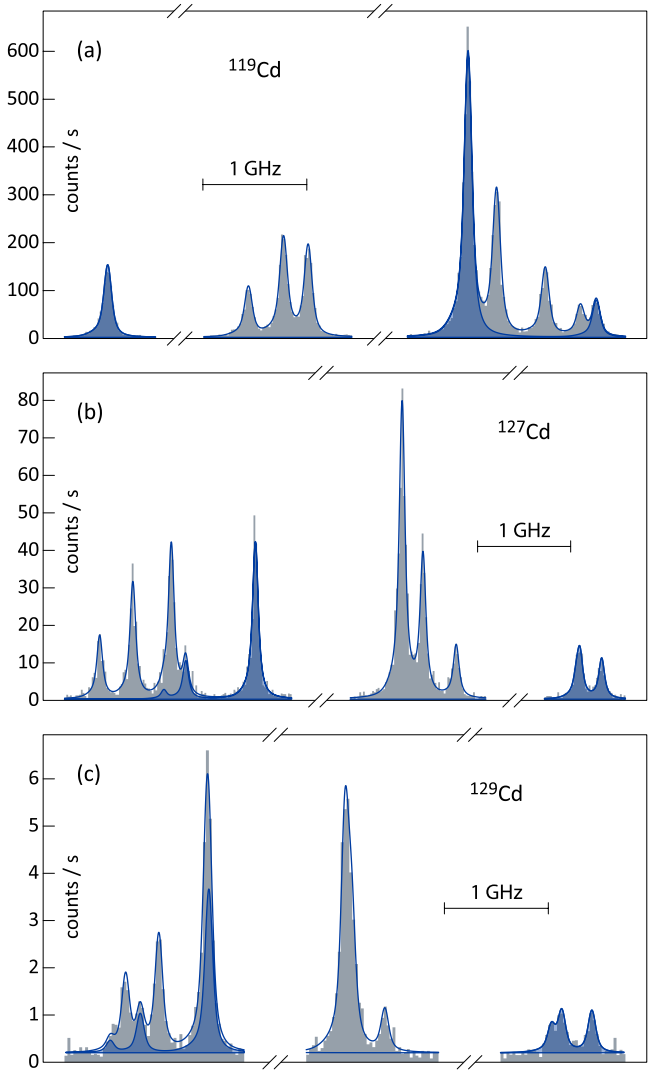

FIG. 1 (color online). Example hfs spectra of ^{119}Cd (a), ^{127}Cd (b), and ^{129}Cd (c). Only frequency regions containing hfs components are displayed. The fitted curve incorporates two states on a common background. The lower-spin state is indicated by a semitransparent fill.

access to isotopic chains thus far unstudied due to demanding transition wavelengths.

In the conventional manner the atomic hyperfine structure was detected by the ion-beam fluorescence as a function of the laser frequency scanned via the Doppler effect. This method is to a large extent insensitive to contaminant beams. However, care has been taken not to exceed 10^6 ions accumulated in the Paul trap in order to avoid space-charge effects. This condition was not a limiting factor for the experiment.

An important accomplishment of this work is the discovery of long-lived isomers in ^{127}Cd and ^{129}Cd. Representative spectra are displayed in Figs. 1(b) and 1(c) where the presence of two nuclear states is clearly identified. It is impossible to determine from the optical measurements alone which of the two is the ground state and what their respective decay modes are. Spins and electromagnetic moments, on the other hand, were determined successfully for both states in each of the isotopes. The presence of such isomers has been suggested in previous studies [13–15].

The experimental results are presented in Table I. Some comments on the spin measurements apply here. The hyperfine structure clearly identifies a ground-state spin of $5/2$ for ^{107}Cd and ^{109}Cd. Spin $1/2$ is assigned to all ground states from ^{111}Cd to ^{119}Cd due to the reduced number of hfs components, three instead of six. A typical example is ^{119}Cd in Fig. 1(a), whose spin adopted in the literature [21] is therefore incorrect. The $3/2$ assignments in $^{121\text{-}129}$Cd are strongly supported by χ^2 analysis of relative hfs intervals and line intensities. Furthermore, the magnetic moments are consistent with an odd-neutron occupation of the $d_{3/2}$ orbital. The hyperfine structure offers limited sensitivity to high spins. Nevertheless, all $11/2$ assignments are rather firm, since the corresponding electromagnetic moments in Fig. 2 are clearly of $h_{11/2}$ origin.

The $S_{1/2}$ hyperfine parameters A are measured with precision on the level of detectable hyperfine anomaly. Accurate results were deduced with the following procedures. For the observed spins of $1/2$, $5/2$, and $11/2$, there are isotopes in the cadmium chain studied by NMR. The hyperfine anomaly within a set of states with identical spins was neglected and each set was assigned a high-precision value of the corresponding spin as a reference. The resulting magnetic moments are in good agreement with NMR measurements, as evident from Table I. For the $3/2$ magnetic moments a hyperfine-anomaly correction was applied with the semiempirical approach of Moskowitz and Lombardi [16]:

$$\frac{A}{A_0}\frac{I}{I_0}\frac{\mu_0}{\mu} - 1 = \frac{\alpha}{|\mu_0|} - \frac{\alpha}{|\mu|}. \quad (1)$$

Quadrupole moments were derived from the hyperfine parameters B using the relation $B = e\,Q\,V_{JJ}$, where V_{JJ} is the electric field gradient at the nucleus and e is the electron charge. Dirac-Hartree-Fock [22] calculations provided the field gradient in the $5p\ ^2P_{3/2}$ state of the cadmium ion. The finite-difference code GRASP [23] was used to generate the numerical-grid wave functions in conjunction with tools and methodology for hyperfine-structure applications previously described [24–26]. The theoretical error bar was evaluated by applying several methods of orbital generation. Details on the applied computational procedure will be published elsewhere. The obtained electric field gradient is presented in Table I along with the quadrupole moments thus determined independent of previous studies. Note that the literature values are about 14% larger in magnitude as they are all referenced to a semiempirical calculation of the electric field gradient for ^{109}Cd [27]. Much of this discrepancy can be accounted for by the

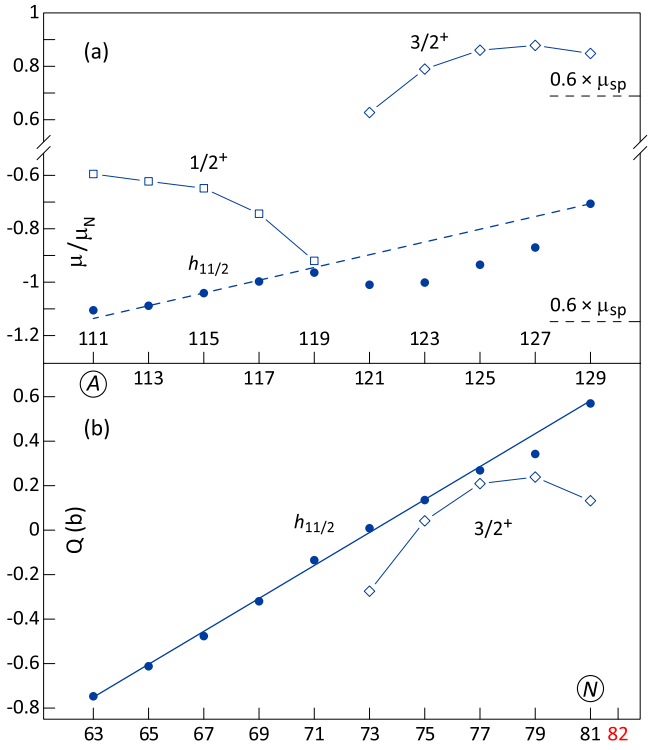

FIG. 2 (color online). Magnetic (a) and quadrupole (b) moments of $^{111\text{-}129}$Cd from this work. The experimental error bars are smaller than the markers. A straight line is fitted through the $h_{11/2}$ quadrupole moments, consistent with Eq. (2). The dashed line indicates the effect of core polarization.

Sternheimer shielding, which is intrinsically included in our calculation, but not in the above-mentioned work.

The linear behavior of the $11/2^-$ quadrupole moments is the most striking and revealing feature of the cadmium nuclei. Moreover, the trend is found to persist uninterruptedly over a sequence of ten odd-mass isotopes, as shown in Fig. 2(b). The most likely cause behind this phenomenon is the unique parity of the $h_{11/2}$ orbital, which would favor simpler shell-model configurations for the $11/2^-$ states. Indeed, in the jj-coupling shell model by Mayer and Jensen [2] single-shell proton states would exhibit a linear increase with respect to the number of protons. Horie and Arima justified a similar dependence for neutrons [3] by taking into account their interaction with protons. In a more general sense, we consider here the seniority scheme and its formalism by de-Shalit and Talmi [28]:

$$\langle j^n|\hat{Q}|j^n\rangle = \frac{2j+1-2n}{2j+1-2\nu}\langle j^\nu|\hat{Q}|j^\nu\rangle. \qquad (2)$$

The origin of Eq. (2) is easier to understand in the particular case of seniority $\nu = 1$, or "normal coupling" [1,2], when all but one particle are coupled to spin zero. By definition the quadrupole moment corresponds to the state with maximum angular-momentum projection; therefore, the magnetic substates $m = \pm j$ are not available for nucleon pairs. This will produce a quadrupole moment dependent on the number of nucleons n. Since the number of j^n configurations is $(2j+1)/2$, Eq. (2) could explain the alignment of only six quadrupole moments for spin $11/2$. Furthermore, the possibility of configurations with different seniorities following the same trend can be excluded. For instance, the matrix element $\langle j^\nu|\hat{Q}|j^\nu\rangle$ for seniority $\nu = 3$, calculated with the aid of tabulated coefficients of fractional parentage [29], is -8% of the single-particle quadrupole moment $Q_{\text{sp}} = \langle j|\hat{Q}|j\rangle$. Such values would greatly deviate from the experimental trend. Clearly, one has to surrender the integer nature of n and interpret it as the actual neutron occupation. This is possible if one assumes that the population of neutron pairs ($I = 0$) is shared between the neighboring orbitals: $s_{1/2}$, $d_{3/2}$, $d_{5/2}$, and $h_{11/2}$, suggesting a kind of degeneracy in terms of total energy per pair. The odd particle, on the other hand, must always occupy $h_{11/2}$, as migration to any other orbital in the shell would result in a change of parity. Finally, assuming no particle-hole excitations across $N = 82$, one can substitute: $n = 1 + p(A - n_0)$, where $n_0 = 111$, $A = N + Z$, and $p = 5/9$. The probability p for pair occupation of $h_{11/2}$ is calculated as the capacity of $h_{11/2}$ for neutron pairs in addition to an odd neutron, divided by the number of pairs filled between ^{111}Cd and ^{129}Cd. It can be easily verified that with this substitution there is exactly one $h_{11/2}$ neutron in ^{111}Cd and eleven in ^{129}Cd. An examination of Eq. (2) shows that the quadrupole moments should cross zero in the middle of the shell, which in the current description corresponds to $A = 120$. Indeed, the crossing point was determined at ^{121}Cd, very close to that prediction. In order to account for the small deviation of one mass unit, the data in Fig. 2(b) are fitted with an offset term Q_{const} representing a constant quadrupole-moment contribution from correlations with the core. The resulting fit parameters are $Q_{\text{sp}} = -667(31)$ mb and $Q_{\text{const}} = -85(8)$ mb. For comparison, the single-particle quadrupole moment of $h_{11/2}$ can be estimated by $-\langle r^2\rangle(2j-1)/(2j+2) = -269$ mb. Here, under the assumption of a uniformly charged spherical nucleus, the mean square radius of the last orbital is approximated by $5/3$ of the mean square charge radius of ^{111}Cd [30]. The ratio of the two values implies a relatively large effective charge $e_n = 2.5e$. This result is commented on below in connection with the magnetic moments. The line of quadrupole moments crossing zero essentially in the middle of the $h_{11/2}$ shell indicates a spherical shape for the $11/2^-$ states. However, one has to acknowledge the deviation from the straight line at ^{127}Cd. It is a small negative effect occurring between ^{126}Cd and ^{128}Cd, for which abnormal first 2^+ energies are reported [5]. The meaning of this observation should be further evaluated in light of possible shell quenching [5,6] against suggested deformation [8,9]. The n dependence of the nuclear quadrupole moment has been investigated in the past [31] and more recently reviewed in the $i_{13/2}$ isomers of lead and mercury [32]. The results

TABLE I. Spins, hyperfine parameters, and electromagnetic moments derived from this work. Experimental uncertainties (uncorrelated) are quoted in parentheses. Uncertainties on the quadrupole moments due to the electric field gradient (correlated) are enclosed in square brackets. Correction for the hyperfine anomaly is applied to the magnetic moments by using separate NMR references for the states with spin 1/2, 5/2, and 11/2, and by the Moskowitz-Lombardi rule [16] for the states with spin 3/2. High-precision magnetic moments calculated from NMR frequency ratios [17,18] relative to the proton [19] and corrected for diamagnetism [20] are displayed for comparison.

$Z+N$	I	$A_{(5p\ ^2P_{3/2})}$ (MHz)	$A_{(5s\ ^2S_{1/2})}$ (MHz)	μ (μ_N)	$\mu_{(NMR)}$ (μ_N)	$B_{(5p\ ^2P_{3/2})}$ (MHz)	Q (mb)
107	5/2	−82.3 (3)	−3009.8 (7)	−0.6151 (2)	−0.6150554 (11)	401 (2)	601 (3)[24]
109	5/2	−111.4 (2)	−4051.0 (7)		−0.8278461 (15)[a]	403 (1)	604 (1)[25]
111	1/2	−398.2 (5)	−14 535.0 (23)		−0.5948861 (8)[a,b]		
111	11/2	−67.2 (2)	−2456.9 (5)	−1.1052 (3)		−498 (3)	−747 (4)[30]
113	1/2	−418.5 (6)	−15 208.0 (23)	−0.6224 (2)	−0.6223009 (9)		
113	11/2	−66.4 (2)	−2419.3 (6)	−1.0883 (3)	−1.0877842 (17)	−408 (2)	−612 (3)[25]
115	1/2	−434.1 (10)	−15 840.6 (30)	−0.6483 (2)	−0.6484259 (12)		
115	11/2	−63.7 (2)	−2314.2 (4)		−1.0410343 (15)[a]	−317 (3)	−476 (5)[19]
117	1/2	−499.2 (11)	−18 168.5 (32)	−0.7436 (2)			
117	11/2	−60.8 (3)	−2217.5 (8)	−0.9975 (4)		−213 (4)	−320 (6)[13]
119	1/2	−615.5 (13)	−22 482.0 (39)	−0.9201 (2)			
119	11/2	−59.0 (2)	−2143.3 (4)	−0.9642 (3)		−90 (2)	−135 (3) [5]
121	3/2	139.7 (15)	5106.2 (34)	0.6269 (7)		−183 (5)	−274 (7)[11]
121	11/2	−62.0 (3)	−2245.3 (8)	−1.0100 (4)		6 (4)	9 (6)
123	3/2	175.5 (13)	6435.6 (27)	0.7896 (6)		28 (3)	42 (5) [2]
123	11/2	−61.7 (2)	−2226.3 (5)	−1.0015 (3)		90 (3)	135 (4) [6]
125	3/2	193.5 (7)	7012.6 (19)	0.8603 (6)		139 (3)	209 (4) [9]
125	11/2	−57.0 (2)	−2077.9 (4)	−0.9347 (2)		179 (5)	269 (7)[11]
127	3/2	195.3 (12)	7159.6 (31)	0.8783 (7)		159 (3)	239 (5)[10]
127	11/2	−52.6 (3)	−1934.5 (5)	−0.8702 (3)		228 (7)	342 (10)[14]
129	3/2	187.7 (23)	6912.9 (48)	0.8481 (8)		88 (5)	132 (7) [5]
129	11/2	−44.1 (5)	−1570.2 (11)	−0.7063 (5)		380 (9)	570 (13)[23]

Electric field gradient: $eV_{JJ}/h = 666\,(27)$ (MHz/b)

[a]Magnetic moment used as a reference for the states with the corresponding spin [μ_0 in Eq. (1), with $\alpha = 0\ \mu_N$].
[b]μ_0 for the 3/2 states ($\alpha/\mu_N = 1.7‰$). The experimental uncertainties of the 3/2 magnetic moments are convoluted with $5 \times 10^{-4}\ \mu_N$ representing the standard deviation of the scatter when the hyperfine anomaly is neglected and different reference values are used.

reported here are the first to demonstrate persistence of that mechanism beyond a single shell. Furthermore, the exceptionally high experimental precision achieved here provides a far more stringent definition of a linear trend.

The nuclei of cadmium exhibit yet another simple trend. Their $11/2^-$ magnetic moments, as shown in Fig. 2(a), increase linearly from ^{111}Cd to ^{129}Cd. Four isotopes in the range $^{121\text{-}127}$Cd make an exception, which appears to be correlated with the spin change of the second long-lived state. Seemingly, this linear dependence is inconsistent with our description of the quadrupole moments since any odd number of nucleons in a single shell would produce the same magnetic moment as a single nucleon [1,2]. In this respect one may consider ^{129}Cd where all neutron orbitals apart from a single $h_{11/2}$ hole are fully occupied with no apparent possibility of "configuration mixing" [33]. It is then expected that the $11/2^-$ magnetic moment of ^{129}Cd should be the most consistent one with the single-particle value, yet it deviates the most. Clearly, an accurate description of the cadmium isotopes should account for the two holes in the $Z = 50$ proton core. First-order core polarization does indeed generate a linear n dependence of the magnetic moment [34], though higher-order contributions may be important as well [35]. The quadrupole moments, on the other hand, are influenced by this proton-core polarization only through the effective charge, whose large value can now be understood.

In summary, advanced laser spectroscopy provided access to the very exotic odd-mass isotopes of cadmium within the $N = 82$ shell. Long-lived $11/2^-$ states are identified in ^{127}Cd and ^{129}Cd for the first time. Remarkably, all quadrupole moments associated with the unique-parity $h_{11/2}$ orbital increase linearly with respect to the number of neutrons, as predicted by the extreme shell model. Yet, this linear trend is found to extend well beyond the single $h_{11/2}$ shell. Interpretation of both magnetic and quadrupole moments is offered in simple terms and in a common framework.

This work has been supported by the Max-Planck Society, the German Federal Ministry for Education and Research under Contract No. 05P12RDCIC, the Belgian IAP Project No. P7/12, the FWO-Vlaanderen, and the European Union seventh framework through ENSAR under Contract No. 262010. The atomic calculations were supported by the Polish National Center of Science (N N202 014140). N. F. received support through GRK Symmetry Breaking (DFG/GRK 1581). D. L. B. acknowledges support from the Bulgarian National Science Fund (DID-02/16). We thank the ISOLDE technical group for their professional assistance.

*Deyan.Yordanov@cern.ch

[1] M. G. Mayer, Phys. Rev. **78**, 16 (1950).
[2] M. G. Mayer and J. H. D. Jensen, *Elementary Theory of Nuclear Shell Stricture* (John Wiley & Sons, Inc., New York, 1955).
[3] H. Horie and A. Arima, Phys. Rev. **99**, 778 (1955).
[4] J. Hakala *et al.*, Phys. Rev. Lett. **109**, 032501 (2012).
[5] T. Kautzsch *et al.*, Eur. Phys. J. A **9**, 201 (2000).
[6] I. Dillmann *et al.*, Phys. Rev. Lett. **91**, 162503 (2003).
[7] M. Dworschak *et al.*, Phys. Rev. Lett. **100**, 072501 (2008).
[8] A. Jungclaus and J. L. Egido, Phys. Scr. **T125**, 53 (2006).
[9] T. R. Rodríguez, J. L. Egido, and A. Jungclaus, Phys. Lett. B **668**, 410 (2008).
[10] P. E. Garrett and J. L. Wood, J. Phys. G **37**, 064028 (2010).
[11] U. Köster, O. Arndt, E. Bouquerel, V. N. Fedoseyev, H. Frånberg, A. Joinet, C. Jost, I. S. K. Kerkines, and R. Kirchner, Nucl. Instrum. Methods Phys. Res., Sect. B **266**, 4229 (2008).
[12] E. Mané *et al.*, Eur. Phys. J. A **42**, 503 (2009).
[13] N. Hoteling *et al.*, Phys. Rev. C **76**, 044324 (2007).
[14] F. Naqvi *et al.*, Phys. Rev. C **82**, 034323 (2010).
[15] K.-L. Kratz *et al.*, Eur. Phys. J. A **25**, 633 (2005).
[16] P. A. Moskowitz and M. Lombardi, Phys. Lett. **46B**, 334 (1973).
[17] R. L. Chaney and M. N. McDermott, Phys. Lett. **29A**, 103 (1969).
[18] P. W. Spence and M. N. McDermott, Phys. Lett. **42A**, 273 (1972).
[19] P. J. Mohr, B. N. Taylor, and D. B. Newell, Rev. Mod. Phys. **80**, 633 (2008).
[20] P. Raghavan, At. Data Nucl. Data Tables **42**, 189 (1989).
[21] D. M. Symochko, E. Browne, and J. K. Tuli, Nucl. Data Sheets **110**, 2945 (2009).
[22] I. P. Grant, *Relativistic Quantum Theory of Atoms and Molecules: Theory and Computation* (Springer, New York, 2007).
[23] P. Jönsson, X. He, C. Froese Fischer, and I. P. Grant, Comput. Phys. Commun. **177**, 597 (2007).
[24] J. Bieroń, C. Froese Fischer, P. Jönsson, and P. Pyykkö, J. Phys. B **41**, 115002 (2008).
[25] J. Bieroń, P. Jönsson, and C. Froese Fischer, Phys. Rev. A **60**, 3547 (1999).
[26] J. Bieroń, P. Pyykkö, and P. Jönsson, Phys. Rev. A **71**, 012502 (2005).
[27] N. S. Laulainen and M. N. McDermott, Phys. Rev. **177**, 1615 (1969).
[28] A. de-Shalit and I. Talmi, *Nuclear Shell Theory* (Academic Press, New York, 1963).
[29] B. F. Bayman and A. Lande, Nucl. Phys. **77**, 1 (1966).
[30] G. Fricke and K. Heilig, *Nuclear Charge Radii* (Springer, Berlin Heidelberg, 2004).
[31] F. W. Byron, M. McDermott, R. Novick, B. Perry, and E. Saloman, Phys. Rev. **136**, B1654 (1964).
[32] G. Neyens, Rep. Prog. Phys. **66**, 633 (2003).
[33] A. Arima and H. Horie, Prog. Theor. Phys. **12**, 623 (1954).
[34] M. Nomura, Phys. Lett. **40B**, 522 (1972).
[35] J. Wouters, N. Severijns, J. Vanhaverbeke, and L. Vanneste, J. Phys. G **17**, 1673 (1991).

Simple Nuclear Structure in $^{111-129}$Cd from Atomic Isomer Shifts

D. T. Yordanov,[1,2,3,*] D. L. Balabanski,[4] M. L. Bissell,[5] K. Blaum,[2] I. Budinčević,[5] B. Cheal,[6] K. Flanagan,[7] N. Frömmgen,[8] G. Georgiev,[9] Ch. Geppert,[8,10] M. Hammen,[8] M. Kowalska,[3] K. Kreim,[2] A. Krieger,[8] J. Meng,[11] R. Neugart,[2,8] G. Neyens,[5] W. Nörtershäuser,[8,12] M. M. Rajabali,[5] J. Papuga,[5] S. Schmidt,[10] and P. W. Zhao[13]

[1]*Institut de Physique Nucléaire, CNRS-IN2P3, Université Paris-Sud, Université Paris-Saclay, 91406 Orsay, France*
[2]*Max-Planck-Institut für Kernphysik, Saupfercheckweg 1, 69117 Heidelberg, Germany*
[3]*CERN European Organization for Nuclear Research, Physics Department, 1211 Geneva 23, Switzerland*
[4]*ELI-NP, Horia Hulubei National Institute for R&D in Physics and Nuclear Engineering, 077125 Magurele, Romania*
[5]*Instituut voor Kern- en Stralingsfysica, KU Leuven, Celestijnenlaan 200D, 3001 Leuven, Belgium*
[6]*Oliver Lodge Laboratory, University of Liverpool, Liverpool, L69 7ZE, United Kingdom*
[7]*School of Physics and Astronomy, University of Manchester, Manchester, M13 9PL, United Kingdom*
[8]*Institut für Kernchemie, Johannes Gutenberg-Universität Mainz, 55128 Mainz, Germany*
[9]*CSNSM, CNRS-IN2P3, Université Paris-Sud, Université Paris-Saclay, 91405 Orsay, France*
[10]*GSI Helmholtzzentrum für Schwerionenforschung GmbH, 64291 Darmstadt, Germany*
[11]*State Key Laboratory of Nuclear Physics and Technology, School of Physics, Peking University, Beijing 100871, China*
[12]*Institut fur Kernphysik, Technische Universität Darmstadt, 64289 Darmstadt, Germany*
[13]*Physics Division, Argonne National Laboratory, Argonne, Illinois 60439, USA*

(Received 13 October 2015; published 22 January 2016)

Isomer shifts have been determined in $^{111-129}$Cd by high-resolution laser spectroscopy at CERN-ISOLDE. The corresponding mean square charge-radii changes, from the $1/2^+$ and the $3/2^+$ ground states to the $11/2^-$ isomers, have been found to follow a distinct parabolic dependence as a function of the atomic mass number. Since the isomers have been previously associated with simplicity due to the linear mass dependence of their quadrupole moments, the regularity of the isomer shifts suggests a higher order of symmetry affecting the ground states in addition. A comprehensive description assuming nuclear deformation is found to accurately reproduce the radii differences in conjunction with the known quadrupole moments. This intuitive interpretation is supported by covariant density functional theory.

DOI: 10.1103/PhysRevLett.116.032501

Complexity is known to dominate the nuclear state, hence, sustaining the need for theoretical input to nearly every experimental work in order to disentangle the nuclear problem down to a set of basic concepts, e.g., shell structure, pairing, "magic" numbers, deformation, etc. However, in near-closed-shell nuclei, simple structures may occur as a result of the spherical symmetry breaking up. The cadmium isotopic chain studied here appears to provide one such instance of simplicity.

Already in 1949, Brix and Kopfermann [1] pointed out the connection between the anomalous isotope shift separating ^{150}Sm and ^{152}Sm, observed for the first time by Schüler and Schmidt in 1934 [2], and the jump of the quadrupole moment between ^{151}Eu and ^{153}Eu. Since then, the importance of looking at nuclear charge radii was further highlighted in the measurements of the neutron-deficient mercury isotopes [3] where shape staggering and shape coexistence generate sizable changes in the charge distribution between neighboring isotopes [4,5] or states in the same nucleus [6]. Thus far, radial changes of such magnitude appear to be uncommon, the other prominent examples being the halo structures in light nuclei [7–11] and the onset of deformation at $N = 60$ [12–16]. Cadmium and mercury are analogues in terms of their charge distributions since both incorporate an open shell with two protons less than a magic number, respectively, $Z = 50$ and $Z = 82$. Despite the similarities, the cadmium case presented here shows no abrupt changes of the nuclear size. Instead, one observes a small-to-moderate effect on the radii characterized by regularity which may be attributed to the unique-parity $h_{11/2}$ orbital.

In this Letter, we report on the simplicity of high-precision isomer shifts derived from collinear laser spectroscopy on the neutron-rich cadmium isotopes towards the $N = 82$ shell closure. A comprehensive model resting on some of the basic concepts in nuclear physics suggests an apparent link between the $11/2^-$ radii and quadrupole moments. The credibility of such an interpretation is examined quantitatively within a relativistic mean field calculation.

The work was carried out with the collinear laser spectroscopy setup at the CERN-ISOLDE radioactive-beam facility. Of interest were the odd neutron-rich

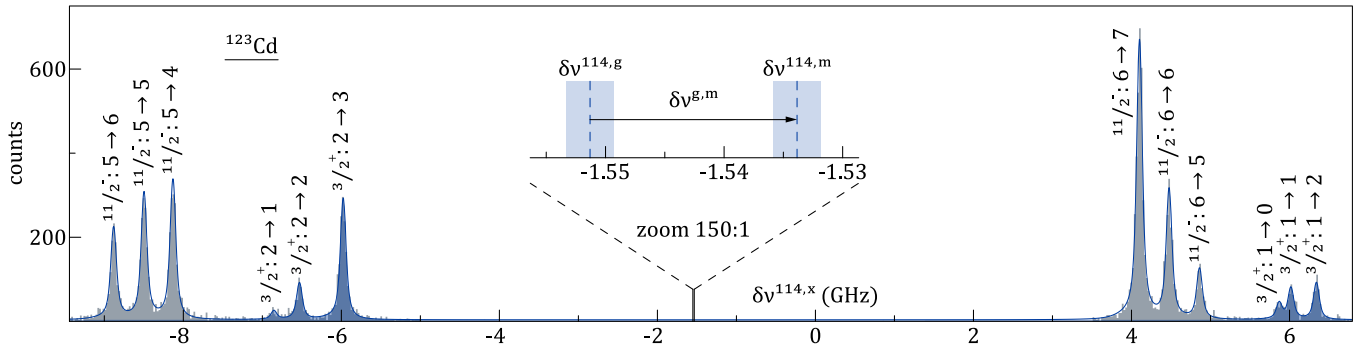

FIG. 1. Spectral lines of ^{123}Cd relative to the excitation frequency of ^{114}Cd in the ionic transition $5s\ ^2S_{1/2} \rightarrow 5p\ ^2P_{3/2}$. The hyperfine structure is comprised of a $3/2^+$ ground state and an $11/2^-$ isomer. The centroids of both states with their statistical uncertainties, as determined by the fit, are shown in the magnified range.

cadmium isotopes whose long-lived isomeric states were readily available as a component in the beam. Most of the measurements were conducted in the cadmium ion in order to benefit from an exceptionally high sensitivity in the $5s\ ^2S_{1/2} \rightarrow 5p\ ^2P_{3/2}$ transition at 214.5 nm [17]. Beam-purity improvement by multiple orders of magnitude was achieved by the use of a neutron converter [18], a quartz transfer line [19], and by resonant laser ionization [20]. Significant background suppression in the fluorescence measurements derived from ion-beam bunching [21,22]. Ground states and isomers were recorded in the same spectrum allowing for a direct measurement of the isomer shift independent of most experimental uncertainties. The work in the ionic system was supported by spectroscopy in the transition $5s5p\ ^3P_2 \rightarrow 5s6s\ ^3S_1$ of the atom at 508.7 nm [17]. The experimental details of both measurements have been previously described in Refs. [23,24] which are reporting on a different aspect of the data.

The isomer shifts in $^{111-129}$Cd are being presented for the first time. The precision of the measurements requires comment, as the studied effects are about 3 orders of magnitude smaller than the hyperfine structure and, in most cases, are appreciably smaller than the natural linewidth. Hence, this study can only be conducted with high resolution. An example spectrum of ^{123}Cd is presented in Fig. 1 where one can acknowledge the relative scale. The following equation relates the nuclear mean square charge-radius change $\delta\langle r^2\rangle^{g,m} = \langle r^2\rangle^m - \langle r^2\rangle^g$ to the isomer shift:

$$\delta\nu^{g,m} = \nu^m - \nu^g = F\delta\langle r^2\rangle^{g,m}. \quad (1)$$

Here, F is the electronic factor related to the change in the total electronic charge density at the site of the nucleus. The term taking into account the difference in mass between the two states is omitted for simplicity since it is negligible with respect to the statistical uncertainty. The atomic masses are still critical for determining the ion-beam velocities since they enter implicitly in the measured Doppler-shifted frequencies. The experimental isomer shifts and thus obtained differential charge-radii changes are presented in Table I. For most of the studied isotopes, the atomic masses of both states are well known [25,26], largely as a result of high-precision Penning-trap measurements [27–29]. In ^{127}Cd and ^{129}Cd, accurate data exist only for one state [30], and therefore, the level ordering is experimentally unknown. With that in mind, we assign the notation "m" to the $11/2^-$ state and "g" to the lower-spin state, either $1/2^+$ or $3/2^+$, coupled to the terms "isomer" and "ground state" even for the latter two cases. Following the systematics in the lighter isotopes, the isomeric excitation energies in ^{127}Cd and ^{129}Cd are assumed to be within a range of ± 200 keV. The above considerations contribute an estimated 0.9 MHz to the final uncertainties. The isotope shifts and the known rms charge radii of the stable isotopes [31] have been analyzed by a King-plot procedure establishing the electronic factors in Table I. The relative uncertainties of those are similar at 8% since the measurements in both transitions are referenced to the same set of

TABLE I. Isomer shifts and differential mean square charge radii of $^{111-129}$Cd in the 214.5 nm and 508.7 nm transitions of Cd II and Cd I, respectively. Statistical uncertainties are quoted in parentheses. Square brackets denote systematic uncertainties reflecting the accuracy of the electronic factors.

	$5s\ ^2S_{1/2} \rightarrow 5p\ ^2P_{3/2}$				$5s5p\ ^3P_2 \rightarrow 5s6s\ ^3S_1$			
	$\delta\nu_{II}^{g,m}$		$\delta\langle r^2\rangle^{g,m}$		$\delta\nu_{I}^{g,m}$		$\delta\langle r^2\rangle^{g,m}$	
A	(MHz)		(μb)		(MHz)		(μb)	
111	−167.5	(9)	272	(2) [21]	31.5	(10)	258	(8) [20]
113	−65.8	(10)	107	(2) [8]	13.8	(8)	113	(6) [9]
115	10.1	(9)	−16	(2) [1]	−2.0	(10)	−16	(8) [1]
117	45.3	(17)	−74	(3) [6]	−7.2	(6)	−59	(5) [5]
119	47.9	(9)	−78	(2) [6]	−9.7	(9)	−80	(7) [6]
121	31.1	(23)	−50	(4) [4]	−6.6	(10)	−54	(8) [4]
123	17.5	(20)	−28	(3) [2]	−5.1	(16)	−42	(13) [3]
125	−13.9	(13)	23	(2) [2]				
127	−119.6	(26)	194	(4) [15]				
129	−235.5	(60)	382	(10) [30]				

$F_{II} = -0.62\,(5)$ MHz/μb $F_I = 0.12\,(1)$ MHz/μb

$F_{II}/F_I = -5.2\,(2)$

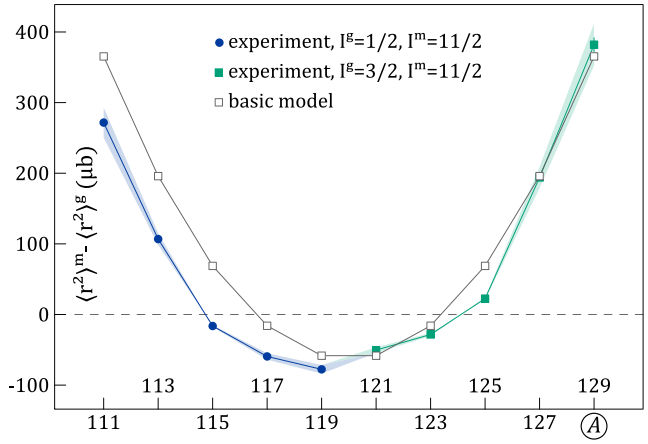

FIG. 2. Mean square charge-radii differences between isomers (m) and ground states (g) in $^{111-129}$Cd compared with calculations discussed in the text. The data correspond to the ionic transition except for ^{117}Cd whose value is taken from the atomic one. In all but one case, the statistical errors are smaller than the dots. The shaded bands represent the systematic uncertainty.

radii. Correspondingly, an 8% systematic uncertainty is associated with all mean square charge-radii changes in the table. The ratio of the electronic factors, being a straightforward ratio of the corresponding isomer shifts, is deduced with a higher precision of 4%. Because of the larger electronic factor, the proportionally larger isomer shifts in the ionic transition dominate the mean square radii changes with smaller uncertainties. The results in the two transitions are statistically consistent. A larger difference of 2.6 standard deviations for ^{117}Cd is potentially caused by random photomultiplier bursts affecting the hyperfine structure of the isomer in the ionic spectrum.

The experimental results are plotted in Fig. 2, where a strikingly simple parabolic trend appears to characterize the differential mean square charge radii as a function of the atomic mass number. To our knowledge, no such clear dependence has ever been observed or discussed before. Furthermore, there is no apparent resemblance of this effect to be found in the mercury analogues [3]. It is reasonable to assume that the present feature is not unique to the cadmium species, but it is likely a general phenomenon that is relevant under common circumstances. In support of this assertion, we consider below a simple model which reproduces the data with remarkable accuracy, and we tie this model to complementary experimental data on the same nuclides. The high experimental precision may be a key factor for making this discovery in the cadmium isotopes and not in the lower-resolution data of tin [32] and lead [33] where, in principle, the unique-parity orbitals $h_{11/2}$ and $i_{13/2}$ should play a similar role.

The question examined here is whether there is a connection between the parabolic mass dependence of the isomer shifts and the linear increase [23] of the $11/2^-$ quadrupole moments in $^{111-129}$Cd. There is a natural link between charge radii and quadrupole moments, since both depend on the nuclear shape and, more specifically, on the deformation parameter β of the charge distribution, in the case of an ellipsoidal nucleus. Below, we propose an interpretation that rests on a number of basic concepts. The mean square charge radius may be decomposed into a spherical and a deformed component [3]. In the case of isomer shifts, i.e., states in the same nucleus, it is approximately true that the spherical component will cancel in the differential mean square charge radii, and therefore, the following relation will hold:

$$\delta\langle r^2\rangle^{g,m} = \frac{5}{4\pi}\langle r_0^2\rangle(\beta_m^2 - \beta_g^2). \tag{2}$$

Here, $\langle r_0^2\rangle$ is the mean square charge radius of the nucleus assuming a spherical distribution. A quick analysis of the above equation implies that the parabolic trend in Fig. 2 may be simply a result of a linearly increasing deformation parameter of the isomeric state while the ground-state deformation is constant or relatively small. The above is a compelling argument to make a connection with the quadrupole moments of the $11/2^-$ states which have been found to obey the simple relation [23]

$$Q = \underbrace{\frac{120 - A}{9}Q_{sp}}_{2Q'} + \underbrace{Q_{core}}_{2Q''}. \tag{3}$$

The above single-particle and core parameters take the values $Q_{sp} = -667(31)$ mb and $Q_{core} = -85(8)$ mb, and A is the atomic mass number. It was concluded, in the original work, that Q_{sp} is about a factor of 2 larger than the expected contribution from a single neutron on the $h_{11/2}$ orbital, suggesting a sizable polarization of the proton distribution. In other words, the polarized, or deformed, proton core must be responsible for half of each measured quadrupole moment. These findings have been later supported by a dedicated theoretical study [34]. Thus, Eq. (3) is, in effect, a definition of two quantities: Q', representing the quadrupole-moment contribution from polarization of the proton core by the addition of $h_{11/2}$ neutrons, and Q'', representing a constant deformation of the ground state regardless of any $h_{11/2}$ occupation.

One of the basic equations resulting from the collective model of the nucleus [35] is the connection between the observable and the intrinsic quadrupole moment: $Q = \langle IK20|IK\rangle\langle II20|II\rangle Q_0$, where K is the projection of the nuclear spin $\vec{I}$ onto the symmetry axis. With the standard assumption of $K = I$, and by expressing the intrinsic quadrupole moment as a function of the deformation, one can formally write

$$Q = \frac{3}{\sqrt{5\pi}}\langle r_0^2\rangle Z\beta\frac{I(2I-1)}{(I+1)(2I+3)}. \tag{4}$$

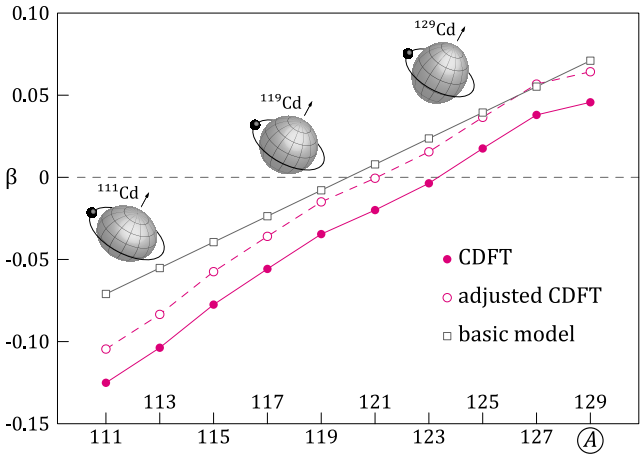

FIG. 3. Quadrupole deformation of the proton distribution in the $11/2^-$ states of $^{111-129}$Cd from covariant density functional theory (CDFT) compared with the basic model discussed in the text. For the sake of clarity, in the visualized examples, the deformation parameters are exaggerated with respect to the model by a factor of 3.

An inclusion of higher powers of β is not necessary because the deformations are relatively small. Indeed, with the aid of Eq. (4) and by approximating the mean square charge radius with a constant value equal to the one of ^{116}Cd [31], one arrives at the deformation parameters plotted with the squares in Fig. 3. For that purpose, the quadrupole moment is substituted by $Q'(A)$ from Eq. (3), and therefore, the obtained deformation parameters correspond to the isomer. Evidently, the parabola in Fig. 2 crosses the zero line. This is a solid evidence that a moderate constant deformation is retained by the cadmium isotopes in their ground states. Clearly, the spin change between ^{119}Cd and ^{121}Cd does not produce any significant effect. We estimate the common deformation of the $1/2^+$ and the $3/2^+$ ground states, on the basis of Q'', to be -0.03. Finally, the obtained β_g and β_m are substituted in Eq. (2) to produce the modeled differential square radii plotted in Fig. 2. The agreement with experiment is remarkable, which in turn strongly supports the formalism and the assumptions along the way. Moreover, this is a manifestation of one of the long-standing concepts in nuclear physics, the deformed nucleus. Yet, one needs to point out that the cadmium species are very close to spherical with deformation parameters never exceeding ± 0.07 along the discussed range. It is, perhaps, in this regime that one truly observes "simple structure in complex nuclei" [36].

Having clearly established its relevance, one still needs to examine any apparent difficulties with the proposed picture of weakly deformed nuclei. In our basic model, we postulate a constant ground-state charge deformation. On the other hand, the measured $3/2^+$ quadrupole moments in $^{121-129}$Cd have been found to spread over a wide range of 500 mb [23]. Arguably, these quadrupole moments are, therefore, of noncollective origin. Neglecting the second term in Eq. (3) for the calculation of the isomer's deformation is somewhat more difficult to justify. In this, we are mostly guided by the experimental data which clearly show a minimum in the differential mean square charge radii at $A = 120$ (Fig. 2). Should the offset in Eq. (3) be taken into account, the modeled parabola will exhibit a minimum at a higher mass number resulting in large discrepancies with the experiment especially at the wings of the parabola. As a matter of fact, the inconsistency does not lie with the isomer shifts but with the quadrupole moments. Since the $h_{11/2}$ shell is being filled between ^{111}Cd and ^{129}Cd, the minimum in quadrupole deformation should, indeed, be at $A = 120$, as argued in Ref. [23]. Instead, a zero quadrupole moment is measured at $A = 121$. So far, the origin of this discrepancy of one mass unit has not been fully understood. Further studies should address the theoretical grounds for our hypotheses and this issue in particular.

The quadrupole deformations of the proton distribution for the $11/2^-$ states obtained with the covariant density functional theory (CDFT) [37,38] are shown in Fig. 3 for comparison. The point-coupling functional PC-PK1 [39] is used for the Lagrangian, and the pairing correlations are taken into account by the Bardeen-Cooper-Schrieffer (BCS) method with a zero-range force. Since we are focusing on the $11/2^-$ states of the odd-A nuclei, the last unpaired neutron will block its occupied level in the BCS calculations; i.e., the Pauli principle excludes this level from the scattering process of nucleon pairs by the pairing correlations. In practical calculations, the single-particle orbital $h_{11/2}$ with the third projection of the total angular momentum $j_z = 11/2$ is always blocked in order to obtain the nuclear states with $K = 11/2$. In fact, in most cases, such $K = I$ states are more favorable in energy than other K states.

It has been found in the previous work [34] that the experimental quadrupole moments are well reproduced by the same calculation. In Fig. 3, we present the corresponding quadrupole deformation values for the proton distribution. In general, it supports the linear behavior of the deformation obtained with the basic model. Note that, here, the CDFT deformations are the average deformation of the intrinsic state associated with the collective part of the quadrupole moment, while other effects from the beyond mean field level, such as the configuration mixing, are not included. This may lead to the differences between the basic model and CDFT results. In fact, as in Ref. [34], the contribution from the noncollective parts of the quadrupole moments are roughly 150 mb. If this amount is accounted for in the CDFT calculation, the deformation parameters would essentially align, as shown with the dashed line in Fig. 3.

In summary, isomer shifts in $^{111-129}$Cd have been found to follow a distinct parabolic mass dependence. This observation is, so far, unique to the cadmium chain, although it may be relevant to other nuclear species under the influence of unique-parity orbitals, namely $h_{11/2}$ or $i_{13/2}$. The corresponding regularity in the radii changes is

understood in conjunction with previously reported electric quadrupole moments within a common picture assuming axial deformation. This sets a constraint on the ground states which are found to have an identical nearly spherical shape along the chain regardless of the change in configuration from $1/2^+$ to $3/2^+$ at ^{121}Cd. Self-consistent calculations with the covariant density functional theory corroborate our conclusions. Nonetheless, our approach does not address the magnetic properties of the above nuclides [40,41], or their $3/2^+$ quadrupole moments in particular. Further theoretical work, notably by using the spherical shell model in a large model space, would be highly beneficial for understanding all aspects of the nuclear simplicity in this region of the nuclear chart.

This work has been supported by the Max-Planck Society, the German Federal Ministry for Education and Research under Contract No. 05P12RDCIC, the Belgian IAP Project No. P7/12, the FWO-Vlaanderen, and the European commission Union seventh framework through ENSAR under Contract No. 262010. The CDFT calculations were supported by U.S. Department of Energy (DOE), Office of Science, Office of Nuclear Physics, under Contract No. DE-AC02-06CH11357, by the Chinese Major State 973 Program No. 2013CB834402, and by the NSFC (Grants No. 11175002 and No. 11335002). We thank the ISOLDE technical group for the outstanding performance of the machine.

*Yordanov@ipno.in2p3.fr

[1] P. Brix and H. Kopfermann, Z. Phys. **126**, 344 (1949).
[2] H. Schüler and Th. Schmidt, Z. Phys. **92**, 148 (1934).
[3] G. Ulm *et al.*, Z. Phys. A **325**, 247 (1986).
[4] J. Bonn, G. Huber, H.-J. Kluge, and E. W. Otten, Z. Phys. A **276**, 203 (1976).
[5] T. Kühl, P. Dabkiewicz, C. Duke, H. Fischer, H. -J. Kluge, H. Kremmling, and E. -W. Otten, Phys. Rev. Lett. **39**, 180 (1977).
[6] P. Dabkiewicz F. Buchinger, H. Fischer, H.-J. Kluge, H. Kremmling, T. Kühl, A. C. Müller, and H. A. Schuessler, Phys. Lett. B **82**, 199 (1979).
[7] L.-B. Wang *et al.*, Phys. Rev. Lett. **93**, 142501 (2004).
[8] R. Sánchez *et al.*, Phys. Rev. Lett. **96**, 033002 (2006).
[9] P. Mueller *et al.*, Phys. Rev. Lett. **99**, 252501 (2007).
[10] W. Geithner *et al.*, Phys. Rev. Lett. **101**, 252502 (2008).
[11] W. Nörtershäuser *et al.*, Phys. Rev. Lett. **102**, 062503 (2009).
[12] C. Thibault *et al.*, Phys. Rev. C **23**, 2720 (1981).
[13] F. Buchinger *et al.*, Phys. Rev. C **41**, 2883 (1990).
[14] P. Campbell *et al.*, Phys. Rev. Lett. **89**, 082501 (2002).
[15] B. Cheal *et al.*, Phys. Lett. B **645**, 133 (2007).
[16] B. Cheal *et al.*, Phys. Rev. Lett. **102**, 222501 (2009).
[17] K. Burns and K. B. Adams, J. Opt. Soc. Am. **46**, 94 (1956).
[18] R. Catherall, J. Lettry, S. Gilardoni, and U. Köster, Nucl. Instrum. Methods Phys. Res., Sect. B **204**, 235 (2003).
[19] U. Köster, O. Arndt, E. Bouquerel, V.N. Fedoseyev, H. Frånberg, A. Joinet, C. Jost, I.S.K. Kerkines, and R. Kirchner, Nucl. Instrum. Methods Phys. Res., Sect. B **266**, 4229 (2008).
[20] U. Köster *et al.*, Nucl. Instrum. Methods Phys. Res., Sect. B **204**, 347 (2003).
[21] H. Frånberg *et al.*, Nucl. Instrum. Methods Phys. Res., Sect. B **266**, 4502 (2008).
[22] K. T. Flanagan *et al.*, Phys. Rev. Lett. **103**, 142501 (2009).
[23] D. T. Yordanov *et al.*, Phys. Rev. Lett. **110**, 192501 (2013).
[24] N. Frömmgen *et al.*, Eur. Phys. J. D **69**, 164 (2015).
[25] M. Wang, G. Audi, and A. H. Wapstra, Chin. Phys. C **36**, 1603 (2012).
[26] G. Audi, O. Bersillon, J. Blachot, and A. H. Wapstra, Nucl. Phys. **A729**, 3 (2003).
[27] M. Breitenfeldt *et al.*, Phys. Rev. C **81**, 034313 (2010).
[28] J. Hakala *et al.*, Phys. Rev. Lett. **109**, 032501 (2012).
[29] A. Kankainen *et al.*, Phys. Rev. C **87**, 024307 (2013).
[30] D. Atanasov *et al.* Phys. Rev. Lett. **115**, 232501 (2015).
[31] G. Fricke and K. Heilig, *Nuclear Charge Radii* (Springer, New York, 2004).
[32] F. Le Blanc *et al.*, Phys. Rev. C **72**, 034305 (2005).
[33] H. D. Witte *et al.*, Phys. Rev. Lett. **98**, 112502 (2007).
[34] P. W. Zhao, S. Q. Zhang, and J. Meng, Phys. Rev. C **89**, 011301(R) (2014).
[35] A. Bohr and B. R. Mottelson, *Nuclear Structure* (W. A. Benjamin, Inc., New York, 1975), Vol. 2.
[36] J. Wood, Physics **6**, 52 (2013).
[37] P. Ring, Prog. Part. Nucl. Phys. **37**, 193 (1996).
[38] J. Meng, H. Toki, S. G. Zhou, S. Q. Zhang, W. H. Long, and L. S. Geng, Prog. Part. Nucl. Phys. **57**, 470 (2006).
[39] P. W. Zhao, Z. P. Li, J. M. Yao, and J. Meng, Phys. Rev. C **82**, 054319 (2010).
[40] Y. Lei, H. Jiang, and S. Pittel, Phys. Rev. C **92**, 024321 (2015).
[41] S. Mishev and V. V. Voronov, Phys. Rev. C **92**, 044329 (2015).

Rapid Communications

Spins and electromagnetic moments of $^{101-109}$Cd

D. T. Yordanov,[1,2,3,*] D. L. Balabanski,[4] M. L. Bissell,[5,6] K. Blaum,[2] A. Blazhev,[7] I. Budinčević,[6] N. Frömmgen,[8] Ch. Geppert,[9,8,10] H. Grawe,[10] M. Hammen,[8] K. Kreim,[2] R. Neugart,[2,8] G. Neyens,[6,3] and W. Nörtershäuser[9,8,10]

[1]*Institut de Physique Nucléaire, CNRS-IN2P3, Université Paris-Sud, Université Paris-Saclay, F-91406 Orsay, France*

[2]*Max-Planck-Institut für Kernphysik, Saupfercheckweg 1, D-69117 Heidelberg, Germany*

[3]*CERN European Organization for Nuclear Research, Physics Department, CH-1211 Geneva 23, Switzerland*

[4]*ELI-NP, Horia Hulubei National Institute for R&D in Physics and Nuclear Engineering, 077125 Magurele, Romania*

[5]*School of Physics and Astronomy, The University of Manchester, Manchester, M13 9PL, United Kingdom*

[6]*Instituut voor Kern- en Stralingsfysica, KU Leuven, Celestijnenlaan 200D, 3001 Leuven, Belgium*

[7]*Institut für Kernphysik, Universität zu Köln, Zülpicher Straße 77, D-50937 Köln, Germany*

[8]*Institut für Kernchemie, Johannes Gutenberg-Universität Mainz, D-55128 Mainz, Germany*

[9]*Institut für Kernphysik, Technische Universität Darmstadt, D-64289 Darmstadt, Germany*

[10]*GSI Helmholtzzentrum für Schwerionenforschung GmbH, D-64291 Darmstadt, Germany*

(Received 25 May 2018; published 30 July 2018)

The neutron-deficient cadmium isotopes have been measured by high-resolution laser spectroscopy at CERN-ISOLDE. The electromagnetic moments of ^{101}Cd have been determined for the first time and the quadrupole-moment precision of ^{103}Cd has been vastly improved. The results on the sequence of $5/2^+$ ground states in $^{101-109}$Cd are tentatively discussed in the context of simple structure in complex nuclei as similarities are found with the $11/2^-$ states in the neutron-rich cases. Comparison with shell-model calculations reveals a prominent role of the two holes in the $Z = 50$ core.

DOI: 10.1103/PhysRevC.98.011303

The isotopic chain of cadmium has emerged in recent years as a pivotal case for nuclear-structure studies in the intermediate-mass region, perhaps outweighing tin itself whose closed proton shell is certainly one of the major landmarks in the nuclear landscape. Shell quenching [1], stellar nucleosynthesis [2], and isomerism [3] are some of the topics addressed most recently. With respect to charge radii and electromagnetic moments, simple mass-dependent trends have been observed in the heavier isotopes [4,5] which are yet to be discussed in the tin counterparts. In this text we are exploring the sequence of neutron-deficient isotopes from ^{109}Cd down to ^{101}Cd whose ground states are expected to involve the $d_{5/2}$ shell embedded in the neighboring $g_{7/2}$, $s_{1/2}$, and $d_{3/2}$ orbits, and as such would be unlikely to adopt a simple configuration when compared to the unique-parity $h_{11/2}$ states in the neutron-rich cases. A simplified view on the matter is outlined in the beginning and ultimately examined against large-scale shell-model calculations.

The measurements were carried out with the instrumentation for collinear laser spectroscopy (COLLAPS) at ISOLDE-CERN [6]. The radionuclides of interest were produced by high-energy protons impinging on a molten tin target and ionized using a plasma source. This production arrangement is very efficient [7] for the longer-lived cadmium isotopes discussed here. After 30-kV acceleration and mass selection the ion beams were accumulated in a radio-frequency Paul trap [8] and subsequently released every 100 ms with a temporal width of about 5 μs. The cadmium ions were excited in the transition: $5s\ ^2S_{1/2} \rightarrow 5p\ ^2P_{3/2}$ at 214.5 nm. The corresponding cw laser beam was produced by sequential second-harmonic generation from the output of a titanium-sapphire laser. Chronologically, this was the first instance of frequency quadrupling being utilized for collinear laser spectroscopy. Atomic excitations were detected by the ion-beam fluorescence as a function of the Doppler-shifted laser frequency [6]. The timing structure of the ion beam mentioned above facilitated a background suppression with a factor of the order of 10^4.

Example spectra of the studied isotopes are fitted and presented in Fig. 1. The fit functions utilize free intensities and the empirical line shape from Ref. [9]. Only in ^{107}Cd the relative amplitudes of the fourth and the fifth resonance from the left have been fixed to each other due to a near coincidence of the $F = 3$ and $F = 4$ levels in the $^2P_{3/2}$ multiplet. The hyperfine parameters and electromagnetic moments from this work are presented in Table I and compared to literature values. We have previously published the results on ^{107}Cd and ^{109}Cd since they played a role in the evaluation of the hyperfine anomaly of the $3/2^+$ states in the heavier isotopes [5]. However, their physics case is being addressed in this text.

Previous laser spectroscopy measurements [10] have been Doppler limited. The high-resolution data presented here

*Yordanov@ipno.in2p3.fr

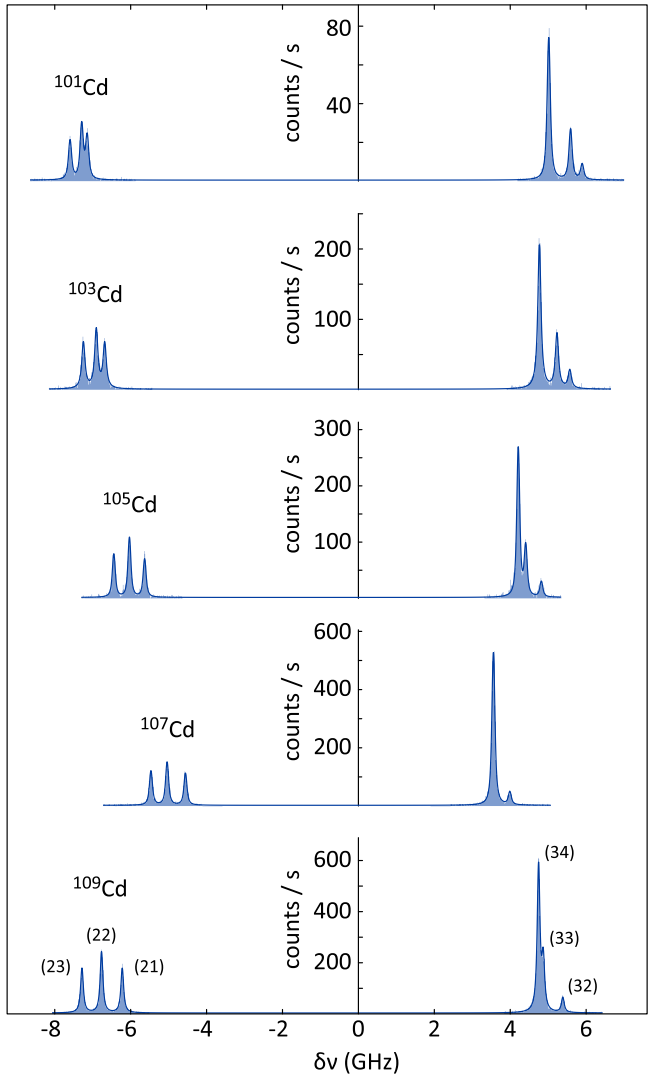

FIG. 1. Example spectra of $^{101-109}$Cd. The hfs level ordering is identical for all cases, as indicated for ^{109}Cd. The frequency scale is relative to the fine-structure splitting.

enable an assessment of the nuclear spin. In all cases the spins are clearly higher than 1/2, otherwise there would have been only three observable transitions instead of six. The relative position of resonances in the spectra of ^{105}Cd, ^{107}Cd, and ^{109}Cd are impossible to describe with any spin other than 5/2 under the condition of a fixed ratio between the $^2S_{1/2}$ and $^2P_{3/2}$ magnetic hyperfine parameters. This result is consistent with the assignments from optical double resonance [11,12], and is further supported by NMR [13]. In both ^{101}Cd and ^{103}Cd, χ^2 analysis under different spin assumptions using the Racah intensities [14] shows a strong minimum at spin 5/2. Spin 3/2 can be ruled out even without evoking the condition of fixed intensities.

The following equations have been used to determine electromagnetic moments from the measured hyperfine parameters:

$$A\frac{I}{\mu} = \text{const}, \tag{1}$$

$$\frac{B}{Q} = \text{const}. \tag{2}$$

The constants above denote the average magnetic field per unit angular momentum and the average electric field gradient induced at the origin by the atomic electrons. For alkali-like multiplets their values are positive, resulting in an identical sign of a given hyperfine parameter and its corresponding nuclear moment. The magnetic moments have been determined from the $^2S_{1/2}$ parameters relative to ^{109}Cd whose magnetic moment [15] is known precisely from NMR frequency ratios [13] and corrected for diamagnetism. All values are negative. Hyperfine anomalies are not deduced because these are extremely small between isotopes of the same spin and similar magnetic moments. The quadrupole moments have been calculated with the electric field gradient 666 (27) MHz/b adopted for the neutron-rich cases [5]. The reduction in absolute value of the quadrupole moments with respect to former measurements [12,16] has been discussed in our previous work [5], and more recently addressed in a multidisciplinary theoretical study [17].

The apparent behavior of the $5/2^+$ electromagnetic moments in $^{101-107}$Cd, as shown in Fig. 2, bears a striking resemblance to the linear trends associated with the $11/2^-$ states in $^{111-129}$Cd [5], as well as other established examples [18–20] involving a unique-parity orbital, either $g_{9/2}$, $h_{11/2}$, or $i_{13/2}$. In the basic case of a j^n configuration the quadrupole moment follows a simple mass dependence [21,22]:

$$\langle j^n|\hat{Q}|j^n\rangle = \frac{2j+1-2n}{2j-1}\langle j|\hat{Q}|j\rangle. \tag{3}$$

TABLE I. Spins, hyperfine parameters, and electromagnetic moments from this work compared with literature values [10–13,15,16]. Statistical uncertainties are shown in parentheses. A second set of parentheses denotes the uncertainty associated with the accuracy of the electric field gradient. The previously published values of ^{107}Cd and ^{109}Cd [5] are given here for completeness.

$Z+N$	I	A (MHz)	A (MHz)	B (MHz)	μ/μ_N	$\mu_{literature}/\mu_N$	Q (mb)	$Q_{literature}$ (mb)
101	5/2	−4395.9 (8)	−120.6 (3)	−118 (2)	−0.8983 (2)		−177 (2) (7)	
103	5/2	−4158.6 (7)	−114.3 (2)	−4 (2)	−0.8498 (2)	−0.81 (3)	−7 (3) (0)	−790 (660)
105	5/2	−3617.6 (6)	−99.7 (2)	251 (1)	−0.7393 (2)	−0.7393 (2)	377 (2) (15)	430 (40)
107	5/2	−3009.8 (7)	−82.3 (3)	401 (2)	−0.6151 (2)	−0.6150554 (11)	601 (3) (24)	680 (70)
109	5/2	−4051.0 (7)	−111.4 (2)	403 (1)		−0.8278461 (15)[a]	604 (1) (25)	690 (70)
		$5s\ ^2S_{1/2}$	$5p\ ^2P_{3/2}$					

[a]Magnetic moment of ^{109}Cd [13,15] used for calibration.

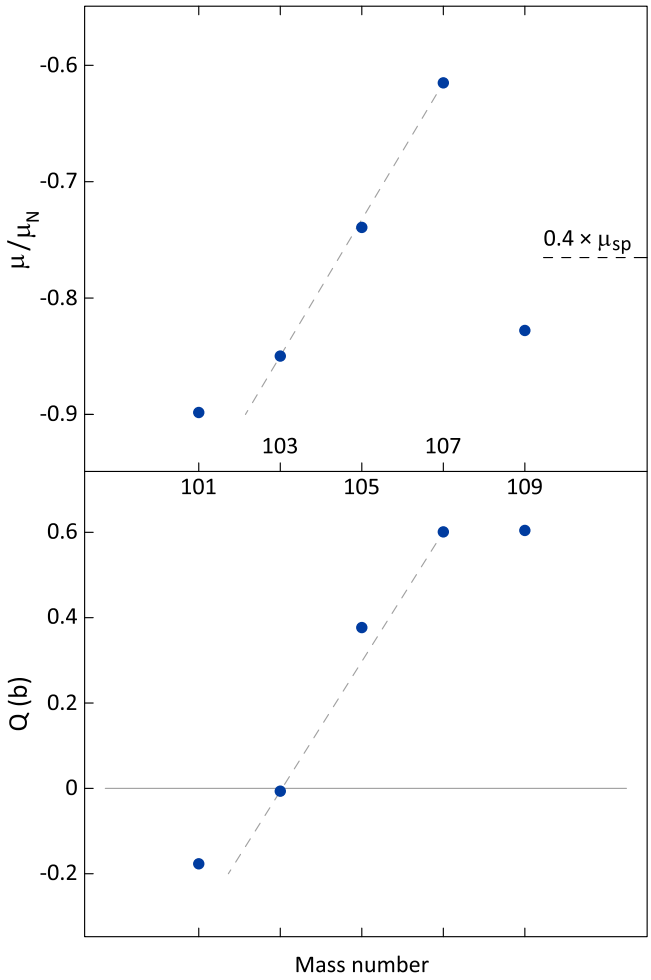

FIG. 2. Ground-state electromagnetic moments of $^{101-109}$Cd from this work. All uncertainties are smaller than the dots. The dashed lines are defined by the values at ^{103}Cd and ^{107}Cd.

The corresponding magnetic moments are expected to remain constant or to exhibit a weak linear deviation induced by core polarization [23,24]. In $^{101-109}$Cd, on the other hand, the odd neutron is not restricted by the parity to a particular orbital. Similar arrangement is at work in the calcium isotopes [25,26] as well as in the $N = 125, 126$ isotones [27], both showing consistency with Eq. (3). Therefore, the evidence for apparent linearity in Fig. 2 is worth investigating. As in our previous work [5] the following substitution can be made:

$$n = 1 + p(A - A_0). \tag{4}$$

The parameters p and A_0 can be easily calculated from the data. First, it would appear that the neutron occupation of $d_{5/2}$ is already at its maximum in ^{107}Cd since the quadrupole moment of ^{109}Cd is identical. Thus, one can formally write $n(107) = 5$. Second, the quadrupole moment of ^{103}Cd from our experiment is practically zero, which according to Eq. (3) occurs for $n = (2j + 1)/2$, therefore $n(103) = 3$. Consequently, one arrives at

$$n = 1 + \frac{A - 99}{2}. \tag{5}$$

Having determined $A_0 = 99$ simply means that there is only one $d_{5/2}$ neutron in ^{99}Cd. And indeed, without particle-hole excitations across $N = 50$ there can be no more. The probability $p = 1/2$ for $d_{5/2}$ occupation corresponds to the number of neutron pairs that can be added to the $d_{5/2}$ shell in addition to an odd neutron, divided by the number of pairs filled between ^{99}Cd and ^{107}Cd. In this interpretation ^{99}Cd would have a quadrupole moment with the opposite sign and identical in magnitude to the 601 mb of ^{107}Cd. In comparison, the size of the single-particle quadrupole moment $-\langle r^2\rangle(2j-1)/(2j+2) = -200$ mb is exactly three times smaller. Here, under the assumption of a uniformly charged spherical nucleus, the mean-square orbital radius is approximated by 5/3 of the mean-square charge radius of ^{111}Cd [28]. The above factor of 3 would indicate that in the proposed simplified picture about 2/3 of the $5/2^+$ quadrupole moments are generated through core polarization. This figure, while similar to the one of the $11/2^-$ states inferred from our previous work [5], is somewhat larger in comparison to a dedicated relativistic mean-field study [29].

A more realistic view on the underlined nuclear structure is obtained by large-scale shell-model calculations carried out with the SR88MHJM Hamiltonian [20,31] using the M-scheme code for massive parallel computation KSHELL [32]. The model space incorporates the orbitals up to the $Z = 50$ and $N = 82$ shell closures outside a hypothetical ^{88}Sr core. Effective spin gyromagnetic ratios at 70% of the free nucleon values and effective charges $e_\nu = e$ and $e_\pi = 1.7e$ were used. The results for the lowest $5/2^+$ states are compared in Fig. 3 to our measurements and the $5/2^+$ isomer in ^{111}Cd [17,30]. For both observables the agreement is fairly good. In the following we offer a simplified analysis of the theoretical output in order to discuss the main features in Fig. 3, and also to assess the relevance of the basic description inferred in the beginning.

One may first consider Fig. 4(a) showing the probability for occurrence of an odd neutron in either and only one of the neutron positive-parity orbitals. For clarity we have presented the occupation of $d_{5/2}$ against the combined contribution from $g_{7/2}$, $d_{3/2}$, and $s_{1/2}$, rather than showing all individually. The latter three would each produce a sizable positive magnetic moment when coupled with a 2^+ proton state. This statement is also valid for $d_{5/2}$, albeit the value is somewhat smaller and strongly dependent on the choice of effective operators. Therefore, the upward trend in the magnetic moments from ^{99}Cd to ^{107}Cd should be understood as a depletion of the single-particle contribution from $d_{5/2}$ in favor of configurations of the type $[(\pi g_{9/2})^{-2}_{2^+} \otimes \nu l_{j^+}]_{5/2^+}$. Conversely, the drop at the ^{109}Cd moment is produced by the opposite effect where the odd-neutron occupation of $d_{5/2}$ is suddenly increased. This occurs almost exclusively at the expense of the $g_{7/2}$ orbital. The emerging picture is different from the one proposed by Byron and co-workers [11] who, on the basis of the configuration-mixing approach of Noya, Arima, and Horie [33], suggested an interplay with the neutron $g_{9/2}$ spin partner. The latter is not present in the SR88MHJM configuration space, and yet the effect is largely reproduced. The value at ^{103}Cd is overestimated in part due to stronger contributions from $s_{1/2}$ and $d_{3/2}$ relative to $g_{7/2}$, as the proton-neutron configurations of the former two generate larger magnetic moments. This

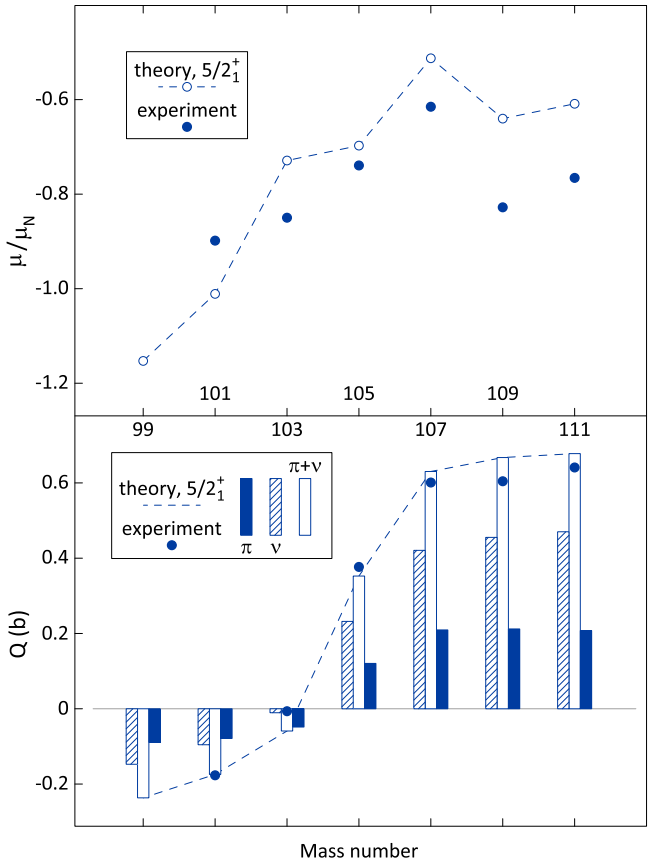

FIG. 3. Electromagnetic moments from theory (opened bars and circles linked by dashed lines) compared to this work and ^{111}Cd [17,30] (filled dots). The experimental uncertainties are smaller than the dots.

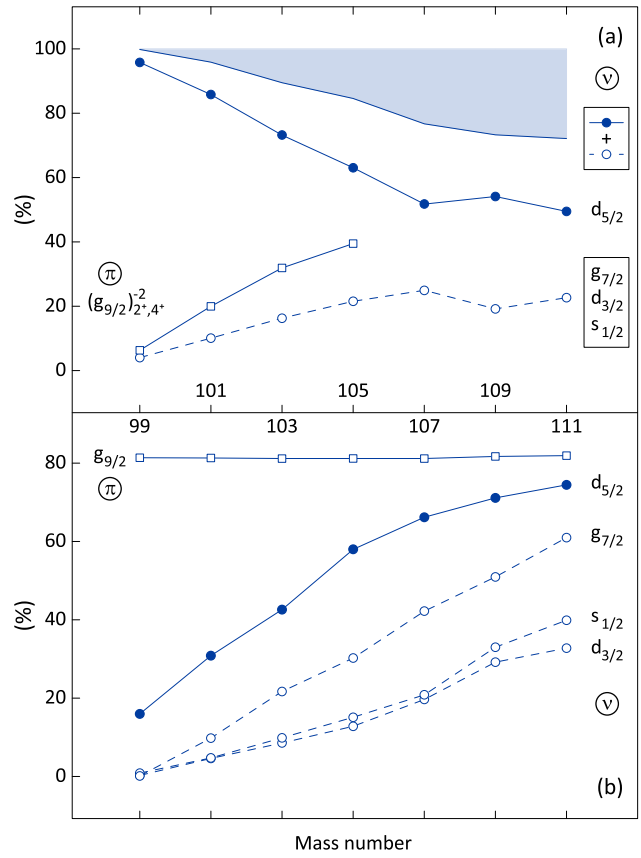

FIG. 4. (a) Odd-neutron occupation of one and only one of the respective orbitals (see text for details). (b) Total population of the respective orbitals in percent. The evolution of the proton $g_{9/2}$ shell is also depicted.

local occurrence contributes to an apparent staggering of the magnetic moments in Fig. 3. Additional calculations with the same interaction using the J-scheme code NuShellX@MSU [34] could be propagated up to ^{105}Cd in order to quantify the amount of $(\pi g_{9/2})^{-2}_{2^+}$ configurations. As shown in Fig. 4(a) the corresponding values rapidly increase toward the middle of the shell, much faster than the summed contribution from the $g_{7/2}$, $d_{3/2}$, and $s_{1/2}$ orbitals. Simultaneously multiparticle configurations of three or a higher number of unpaired nucleons also become abundant, as represented by the shaded area in the figure. An onset of $(\pi g_{9/2})^{-2}_{4^+}$ configurations is also present toward the middle of the shell, rising to about 4% in ^{105}Cd. The negative-parity orbitals $p_{1/2}$ and $h_{11/2}$ are not depicted as their role is limited.

The trend of theoretical quadrupole moments in Fig. 3 appears to deviate from linearity, with the value at ^{103}Cd seemingly being an inflection point. However, there is no prominent feature at this mass in either of the plots in Fig. 4. On the contrary, the occurrence of an odd $d_{5/2}$ neutron in Fig. 4(a) and the total $d_{5/2}$ population in Fig. 4(b) both change regularly between ^{99}Cd and ^{107}Cd. Hence, the role of 2^+ proton configurations requires further investigation. Accordingly, the quadrupole moment is decomposed into a proton- and a neutron-generated part, as shown explicitly in Fig. 3. It is evident that in all cases the proton constituent amounts to about 1/3 of the total moment, a figure twice smaller than anticipated from the simplistic interpretation above. In the beginning of the shell the quadrupole moment obtains a negative value, followed by a regular increase in accordance with Eq. (3) as a function of the $d_{5/2}$ population. The features on top of this trend should be understood as an interplay between configurations of the type $[(\pi g_{9/2})^{-2}_{2^+} \otimes \nu(l_j)^n_{j^+}]_{5/2^+}$. The corresponding contributions involving $s_{1/2}$ and $d_{3/2}$ neutrons are negative. These cause a prediction at ^{99}Cd below the single-particle value discussed earlier. In the heavier isotopes the quadrupole moment rapidly increases with the filling of the $g_{7/2}$ and $d_{5/2}$ orbitals whose contribution is positive. Toward the end of the studied range the moments appear to incline toward a constant value. This should be attributed in part to a $d_{5/2}$ saturation, and in part to approaching a limit in the amount of non-zero-spin proton couplings which would also change composition to include 4^+ and possibly higher-spin values. On the whole, the observed trend is governed by the $d_{5/2}$ occupation being delayed due to the simultaneous $g_{7/2}$ filling. It is not symmetric to midshell $d_{5/2}$ nor to $Q = 0$, as an increasing proton $g_{9/2}$ contribution is superimposed. For the sake of completeness, we note that the lowest $5/2^+$ states calculated in ^{107}Cd and ^{109}Cd appear at small excitation energies above

a $1/2^+$ ground state, respectively, at 59 and 234 keV. In ^{111}Cd the level ordering of the two states is reproduced correctly.

In summary, we have provided accurate ground-state electromagnetic moments for $^{101-105}$Cd. The data are initially discussed in the context of simple structure in complex nuclei [26,35–37]. Large-scale shell-model calculations using the SR88MHJM Hamiltonian firmly establish the significance of the proton $g_{9/2}$ contribution to both electromagnetic moments and the importance of the joined filling, in particular of the close-lying $d_{5/2}$ and $g_{7/2}$ orbitals, for the observed nuclear structure. With regard to the quadrupole moment of ^{99}Cd, -600 mb have been inferred from a simplistic interpretation. The shell-model calculations, on the other hand, support a much weaker value of about -240 mb. A measurement by collinear laser spectroscopy is certainly achievable, and being a closed-shell-plus-one-neutron case of key importance, ^{99}Cd will most certainly receive further attention in the future.

We thank the ISOLDE technical group for their professional assistance. This work has been supported by the Max-Planck Society, the German Federal Ministry for Education and Research under Contract No. 05P12RDCIC, the Belgian IAP Project P7/12, the FWO-Vlaanderen, and the European Union seventh framework through ENSAR under Contract No. 262010. D.L.B. acknowledges support by the Extreme Light Infrastructure Nuclear Physics, a project co-financed by the Romanian Government and the European Union through the European Regional Development Fund – Competitiveness Operational Programme (1/07.07.2016, COP, ID 1334).

[1] I. Dillmann, K.-L. Kratz, A. Wöhr, O. Arndt, B. A. Brown, P. Hoff, M. Hjorth-Jensen, U. Köster, A. N. Ostrowski, B. Pfeiffer, D. Seweryniak, J. Shergur, and W. B. Walters, Phys. Rev. Lett. **91**, 162503 (2003).
[2] D. Atanasov, P. Ascher, K. Blaum, R. B. Cakirli, T. E. Cocolios, S. George, S. Goriely, F. Herfurth, H.-T. Janka, O. Just, M. Kowalska, S. Kreim, D. Kisler, Y. A. Litvinov, D. Lunney, V. Manea, D. Neidherr, M. Rosenbusch, L. Schweikhard, A. Welker, F. Wienholtz, R. N. Wolf, and K. Zuber, Phys. Rev. Lett. **115**, 232501 (2015).
[3] A. Jungclaus *et al.*, Phys. Lett. B **772**, 483 (2017).
[4] D. T. Yordanov, D. L. Balabanski, M. L. Bissell, K. Blaum, I. Budinčević, B. Cheal, K. Flanagan, N. Frömmgen, G. Georgiev, C. Geppert, M. Hammen, M. Kowalska, K. Kreim, A. Krieger, J. Meng, R. Neugart, G. Neyens, W. Nortershauser, M.M. Rajabali, J. Papuga, S. Schmidt, and P. W. Zhao, Phys. Rev. Lett. **116**, 032501 (2016).
[5] D. T. Yordanov, D. L. Balabanski, J. Bieroń, M. L. Bissell, K. Blaum, I. Budinčević, S. Fritzsche, N. Frömmgen, G. Georgiev, C. Geppert, M. Hammen, M. Kowalska, K. Kreim, A. Krieger, R. Neugart, W. Nörtershäuser, J. Papuga, and S. Schmidt, Phys. Rev. Lett. **110**, 192501 (2013).
[6] R. Neugart *et al.*, J. Phys. G **44**, 064002 (2017).
[7] H. J. Kluge, Isolde users' guide, CERN-86-05 (CERN, Geneva, 1986), p. 200, https://cds.cern.ch/collection/ISOLDE%20Reports?ln=en.
[8] E. Mané *et al.*, Eur. Phys. J. A **42**, 503 (2009).
[9] D. T. Yordanov *et al.*, J. Phys. G **44**, 075104 (2017).
[10] F. Buchinger *et al.*, Nucl. Phys. A **462**, 305 (1987).
[11] F. W. Byron, M. N. McDermott, and R. Novick, Phys. Rev. **132**, 1181 (1963).
[12] N. S. Laulainen and M. N. McDermott, Phys. Rev. **177**, 1615 (1969).
[13] P. W. Spence and M. N. McDermott, Phys. Lett. A **42**, 273 (1972).
[14] P. C. Magnante and H. H. Stroke, J. Opt. Soc. Am. **59**, 836 (1969).
[15] P. Raghavan, At. Data Nucl. Data Tables **42**, 189 (1989).
[16] M. N. McDermott and R. Novick, Phys. Rev. **131**, 707 (1963).
[17] H. Haas *et al.*, Europhys. Lett. **117**, 62001 (2017).
[18] G. Neyens, Rep. Prog. Phys. **66**, 633 (2003).
[19] H. Grawe, Lect. Notes Phys. **651**, 33 (2004).
[20] T. Faestermann, M. Górska, and H. Grawe, Prog. Part. Nucl. Phys. **69**, 85 (2013).
[21] H. Horie and A. Arima, Phys. Rev. **99**, 778 (1955).
[22] I. Talmi, *Simple Models of Complex Nuclei* (Harwood Academic, Amsterdam, 1993).
[23] M. Nomura, Phys. Lett. B **40**, 522 (1972).
[24] J. Wouters, N. Severijns, J. Vanhaverbeke, and L. Vanneste, J. Phys. G **17**, 1673 (1991).
[25] R. F. GarciaRuiz, M. L. Bissell, K. Blaum, N. Frömmgen, M. Hammen, J. D. Holt, M. Kowalska, K. Kreim, J. Menéndez, R. Neugart, G. Neyens, W. Nörtershäuser, F. Nowacki, J. Papuga, A. Poves, A. Schwenk, J. Simonis, and D. T. Yordanov, Phys. Rev. C **91**, 041304(R) (2015).
[26] I. Talmi, Phys. Scr. **92**, 083001 (2017).
[27] R. Ferrer, A. Barzakh *et al.*, Nat. Commun. **8**, 14520 (2017).
[28] G. Fricke and K. Heilig, *Nuclear Charge Radii* (Springer, Berlin, 2004).
[29] P. W. Zhao, S. Q. Zhang, and J. Meng, Phys. Rev. C **89**, 011301(R) (2014).
[30] H. Bertschat *et al.*, Z. Phys. **270**, 203 (1974).
[31] O. Kavatsyuk *et al.*, Eur. Phys. J. A **31**, 319 (2007).
[32] N. Shimizu, arXiv:1310.5431.
[33] H. Noya, A. Arima, and H. Horie, Prog. Theor. Phys. Suppl. **8**, 33 (1958).
[34] B. A. Brown and W. Rae, Nucl. Data Sheets **120**, 115 (2014).
[35] A. E. Stuchbery, J. Phys.: Conf. Ser. **366**, 012042 (2012).
[36] J. Wood, Physics **6**, 52 (2013).
[37] P. V. Isacker, Nucl. Phys. News **24**, 23 (2014).

Structural trends in atomic nuclei from laser spectroscopy of tin

Deyan T. Yordanov,[1,2,*] Liss V. Rodríguez,[1,3] Dimiter L. Balabanski,[4] Jacek Bieroń,[5] Mark L. Bissell,[6] Klaus Blaum,[3] Bradley Cheal,[7] Jörgen Ekman,[8] Gediminas Gaigalas,[9] Ronald F. Garcia Ruiz,[2,†] Georgi Georgiev,[10] Wouter Gins,[11,‡] Michel R. Godefroid,[12] Christian Gorges,[13,§] Zoltán Harman,[3] Hanne Heylen,[3,2] Per Jönsson,[8] Anastasios Kanellakopoulos,[11] Simon Kaufmann,[13] Christoph H. Keitel,[3] Varvara Lagaki,[2,14] Simon Lechner,[2,15] Bernhard Maaß,[13] Stephan Malbrunot-Ettenauer,[2] Witold Nazarewicz,[16] Rainer Neugart,[17,3] Gerda Neyens,[11,2] Wilfried Nörtershäuser,[13] Natalia S. Oreshkina,[3] Asimina Papoulia,[8,18] Pekka Pyykkö,[19] Paul-Gerhard Reinhard,[20] Stefan Sailer,[21] Rodolfo Sánchez,[22] Sacha Schiffmann,[12,18] Stefan Schmidt,[13] Laura Wehner,[17] Calvin Wraith,[7] Liang Xie,[6] Zhengyu Xu,[11,¶] and Xiaofei Yang[11,23]

[1]*Institut de Physique Nucléaire, CNRS-IN2P3, Université Paris-Sud, Université Paris-Saclay, Orsay, France*
[2]*Experimental Physics Department, CERN, Geneva, Switzerland*
[3]*Max-Planck-Institut für Kernphysik, Heidelberg, Germany*
[4]*ELI-NP, Horia Hulubei National Institute for R&D in Physics and Nuclear Engineering, Magurele, Romania*
[5]*Instytut Fizyki imienia Mariana Smoluchowskiego, Uniwersytet Jagielloński, Kraków, Poland*
[6]*School of Physics and Astronomy, The University of Manchester, Manchester, United Kingdom*
[7]*Oliver Lodge Laboratory, University of Liverpool, Liverpool, United Kingdom*
[8]*Department of Materials Science and Applied Mathematics, Malmö University, Malmö, Sweden*
[9]*Institute of Theoretical Physics and Astronomy, Vilnius University, Vilnius, Lithuania*
[10]*CSNSM, CNRS-IN2P3, Université Paris-Sud, Université Paris-Saclay, Orsay, France*
[11]*Instituut voor Kern- en Stralingsfysica, KU Leuven, Leuven, Belgium*
[12]*Chimie Quantique et Photophysique, Université libre de Bruxelles, Brussels, Belgium*
[13]*Institut für Kernphysik, Technische Universität Darmstadt, Darmstadt, Germany*
[14]*Institut für Physik, Universität Greifswald, Greifswald, Germany*
[15]*Technische Universität Wien, Vienna, Austria*
[16]*Department of Physics and Astronomy and FRIB Laboratory, Michigan State University, East Lansing, Michigan, USA*
[17]*Institut für Kernchemie, Universität Mainz, Mainz, Germany*
[18]*Division of Mathematical Physics, Department of Physics, Lund University, Lund, Sweden*
[19]*Department of Chemistry, University of Helsinki, Helsinki, Finland*
[20]*Institut für Theoretische Physik II, Universität Erlangen-Nürnberg, Erlangen, Germany*
[21]*Technische Universität München, Munich, Germany*
[22]*GSI Helmholtzzentrum für Schwerionenforschung GmbH, Darmstadt, Germany*
[23]*School of Physics and State Key Laboratory of Nuclear Physics and Technology, Peking University, Beijing, China*

(Dated: April 3, 2020)

Tin is the chemical element with the largest number of stable isotopes. Its complete proton shell, comparable with the closed electron shells in the chemically inert noble gases, is not a mere precursor to extended stability; since the protons carry the nuclear charge, their spatial arrangement also drives the nuclear electromagnetism. We report high-precision measurements of the electromagnetic moments and isomeric differences in charge radii between the lowest $1/2^+$, $3/2^+$, and $11/2^-$ states in $^{117\text{-}131}$Sn, obtained by collinear laser spectroscopy. Supported by state-of-the-art atomic-structure calculations, the data accurately show a considerable attenuation of the quadrupole moments in the closed-shell tin isotopes relative to those of cadmium, with two protons less. Linear and quadratic mass-dependent trends are observed. While microscopic density functional theory explains the global behaviour of the measured quantities, interpretation of the local patterns demands higher-fidelity modelling.

Nuclear science greatly relies on observations, not only in naturally-occurring, but also in laboratory-synthesized nuclides, which represent the majority of approximately 3000 species discovered to date [1]. Either type can be studied by laser spectroscopy, a non-destructive experimental technique probing the hyperfine splitting of atomic energy levels induced by the nuclear electromagnetism. An electric quadrupole moment, for instance, reflects an anisotropic (deformed) charge distribution within the nucleus [2]. Appreciable nuclear deformation is primarily found in species with open shells for both protons and neutrons [3, 4]. The tin isotopes, with their proton core complete (spherical), may still acquire quadrupole moments through the geometry of valence neutron orbitals. Those can be discussed in terms of schematic theoretical descriptions such as the seniority or generalized-seniority models [5, 6], which explain the striking regularities previously observed, e.g. the nearly-constant energy of excited states and simple patterns exhibited by other quantities [7–9]. When looking into details, however, deviations from regular behaviour are revealed as fingerprints of the underlying nucleonic shell

* Deyan.Yordanov@cern.ch
† Massachusetts Institute of Technology, Cambridge, USA
‡ Department of Physics, University of Jyväskylä, Jyväskylä, Finland.
§ Institut für Kernchemie, Universität Mainz, Mainz, Germany
¶ Department of Physics and Astronomy University of Tennessee, Knoxville, Tennessee, USA

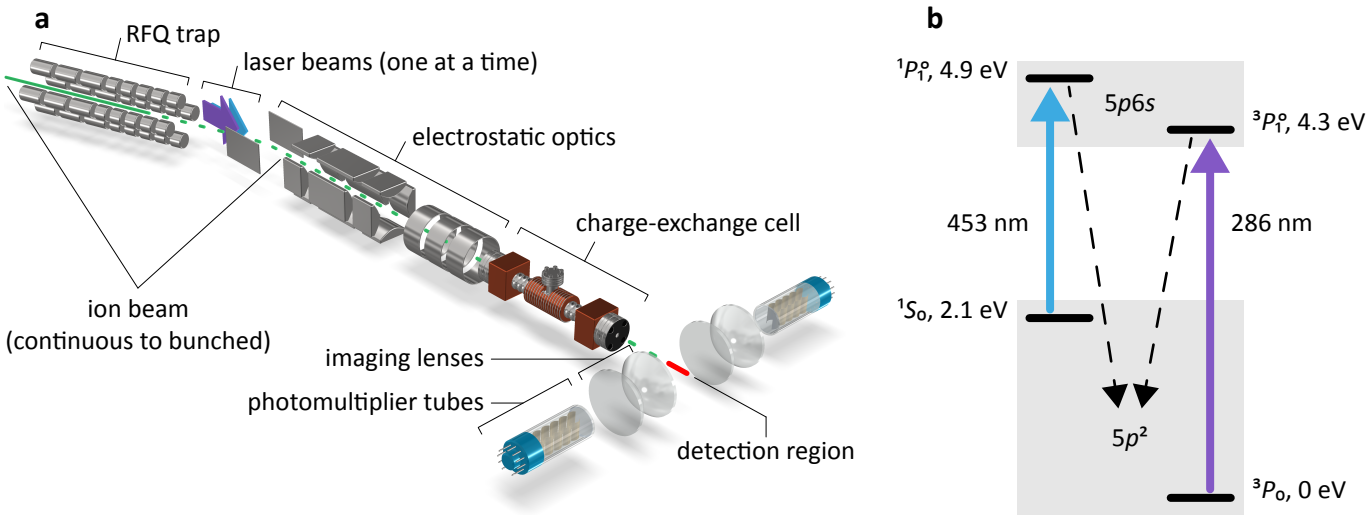

FIG. 1. **Experimental arrangement and level scheme in the neutral atom of Sn.** **a**, From left to right: linear Paul trap for ion-beam bunching; continuous-wave laser beams; electrostatic elements: deflector, quadrupole triplet, cylinder lens; alkali-vapour cell; optical detection: fused-silica aspheric lenses, photomultiplier tubes. **b**, Partial energy level scheme of neutral tin indicating the studied excitations and the subsequent fluorescence used for detection. The shaded areas indicate the groups of $5p^2$ and $5p6s$ levels.

structure and many-body correlations [10–13].

Here we study the odd-mass isotopes $^{117\text{-}131}$Sn. An $11/2^-$ state with an unpaired neutron confined by the rules of quantum mechanics to the unique-parity $h_{11/2}$ orbital is present in each case. The remaining valence orbitals in the neutron shell have the opposite parity and considerably lower angular momenta, which results in isomerism (metastability of an excited nuclear state). Quadrupole moments in the closed-shell tin isotopes are found at variance with those in the cadmium isotopes having two protons less. Differences in radii between nuclear ground and isomeric states, on the other hand, are shown to remain surprisingly similar. Calculations in the framework of nuclear density functional theory with recently optimized input describe the global behaviour of the experimental observables. Interpretation of the local patterns, however, calls for a dedicated microscopic modelling.

Results and discussion

Measurements. Short-lived nuclei, naturally occurring only in astrophysical phenomena such as supernovae explosions [14], are synthesized on Earth using particle accelerators. The tin isotopes for this study were produced at the CERN-ISOLDE laboratory [15] by uranium fission using fast protons travelling with more than 90% of the speed of light. Prior conversion to neutrons increased the fission purity [16]. Tin atoms were laser ionized, accelerated to an energy of 40 or 50 keV to form a continuous beam of fast-travelling ions, and mass separated. Typically, each 100-ms segment of the beam was compressed into an ion bunch with a temporal width of less than 10 μs using a linear Paul trap [17]. Individual bunches were subsequently released, re-accelerated, and guided with a dedicated set of electrostatic optics into a volume of vaporized sodium for neutralization. Narrow-bandwidth continuous-wave laser light was introduced along the axis of ion/atom propagation. The atomic-beam energy and the associated Doppler-shifted laser frequency were defined at the sodium charge-exchange cell, whose electrostatic potential was scanned in search of resonant atomic-beam fluorescence. The latter was collected by telescopes of aspheric lenses and imaged onto the photocathodes of photomultiplier tubes for single-photon counting. The measurements were correlated with the timing structure of the atomic beam, which allowed substantial background suppression and high sensitivity. A sketch of the experimental arrangement is shown in Fig. 1a.

Laser excitation of tin atoms was performed using the two complementary transitions in Fig. 1b to resolve the nuclear properties, as described in Methods. The laser system comprised a diode-pumped solid-state laser, a tunable laser using either dye or titanium-sapphire as the active medium, and a second-harmonic-generation cavity. Two nuclear states were detected for each odd-mass isotope in the range $^{117\text{-}131}$Sn, as shown in Fig. 2. The hyperfine structure is characterized by a sizeable quadrupole splitting in the $5p6s\ ^1P_1^o$ state and a large magnetic splitting in the $5p6s\ ^3P_1^o$ state. The two are correlated through the nuclear electromagnetic properties and are thus fitted simultaneously. All results are shown in Tab. I. The magnetic moments therein incorporate the latest computation of the absolute shielding constant in tin [18]. The accuracy of quadrupole moments is ensured by the theoretical work outlined in the following.

Atomic structure calculations. The fully relativistic multiconfiguration Dirac-Hartree-Fock (MCDHF) method was employed to calculate the magnetic dipole hyperfine-structure constants and electric-field gradients in the

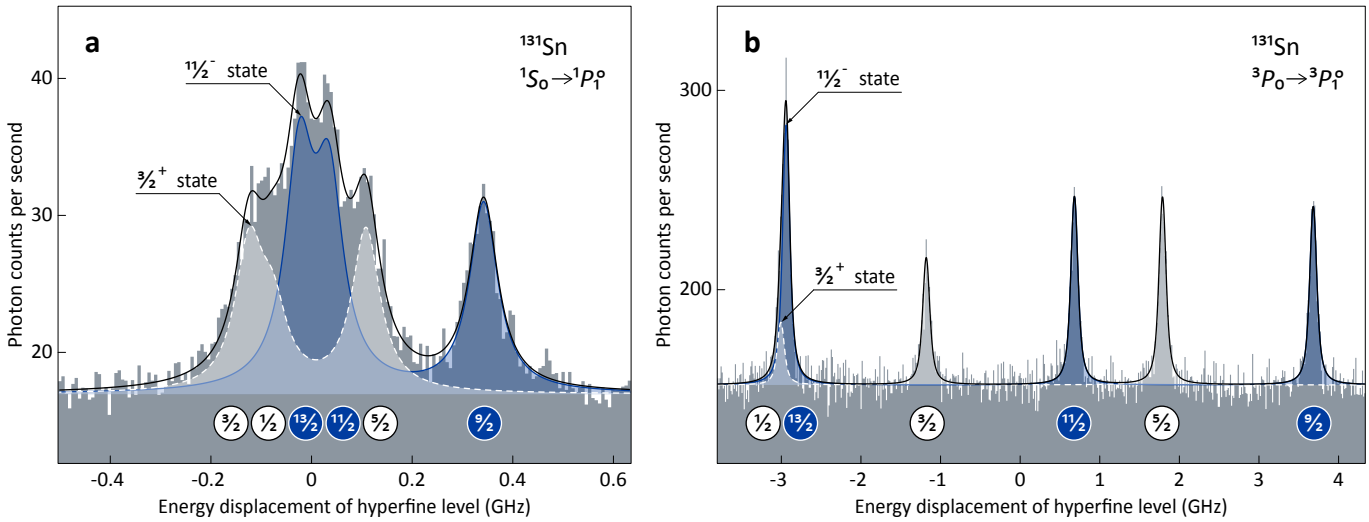

FIG. 2. **Fluorescence spectra of ^{131}Sn.** Hyperfine structure in the: **a**, $5p6s\ {}^1P_1^o$ state; **b**, $5p6s\ {}^3P_1^o$ state. The fitted black curves comprise a $3/2^+$ nuclear ground state, represented by the dashed white lines, and an $11/2^-$ isomer, represented by the solid blue lines. Hyperfine levels are denoted by the individual total angular-momentum quantum number.

$5p6s\ {}^1P_1^o$ and $5p6s\ {}^3P_1^o$ states of tin (see Methods for definition of these quantities). Three independent series of large-scale calculations were performed, adopting different computational strategies and correlation models using the General Relativistic Atomic Structure Package computer codes GRASP2K [19] and GRASP2018 [20], based on the same relativistic MCDHF theory and methodology [21, 22]. Classes of electron excitations adopting different multireference spaces and active orbital sets were investigated in detail to clarify the role of electron correlation in the relevant matrix elements. A combined effort was put in assessing the reliability of the resulting *ab initio* electronic factors involved in M1 and E2 hyperfine interactions for both levels [23]. The quadrupole moments from this work are obtained with the electric-field gradient 706(50) MHz/b in the singlet state, which is the mean value resulting from the aforementioned calculations. With regard to the dipole hyperfine constants in the triplet state, cross-checking calculations were performed using the configuration interaction Dirac-Fock-Sturm (CI-DFS) method [24]. The hyperfine anomaly (see Methods) was estimated in separate mulitireference calculations for each isotope using a Fermi charge distribution with adopted root mean square radius and a parametrized squared harmonic-oscillator wave function of the last unpaired neutron as magnetization distribution [25]. It reaches a maximum at $^{119g}\Delta^{131m} = 0.05\%$ due to the limited overlap between the $3s$ and $1h$ nuclear wave functions and partly due to the increase in the charge radius between the two isotopes. The anomaly between positive-parity states was found to be negligible with respect to the experimental precision.

Experimental trends. The data on quadrupole moments and differences in mean square charge radii between nuclear ground and isomeric states are compared in Fig. 3 with values measured in the cadmium isotones [27–29]. A number of key observations are worth being pointed out: **(i)** There is a significant attenuation of the quadrupole moments of tin ($Z = 50$) with respect to cadmium ($Z = 48$). Note that the observed charge (proton) quadrupole moment originates from the nuclear response to an odd neutron in a $d_{3/2}$ or an $h_{11/2}$ single-particle state. **(ii)** The fitted trends in Figs. 3a and 3b cross each other close to zero, i.e., the $h_{11/2}$ orbital is half full [5, 6] for both tin and cadmium at $N = 73$, as is $d_{3/2}$ at $N = 75$. **(iii)** The quadrupole moments of tin in the $11/2^-$ states are by a factor of about two larger in magnitude than those in the $3/2^+$ states. This is consistent with a stronger quadrupole polarization exerted by unique-parity $h_{11/2}$ nucleons. **(iv)** All trends are remarkably smooth, often near linear, at most quadratic. **(v)** The quadrupole moments of the $11/2^-$ states in tin exhibit a quadratic behaviour with changing neutron number, strikingly different from the linear trend observed along the cadmium chain. **(vi)** The pattern is unexpectedly reversed for the $3/2^+$ states whose quadrupole moments change linearly for tin and quadratically for cadmium. **(vii)** Re-evaluated values for ^{113,115,119}Sn [26] in Figs. 3a and 3b are consistent with the trends defined by the heavier isotopes. These are independently calibrated to experimental γ-decay rates, thus showing consistency between nuclear data and atomic theory. **(viii)** The measured mean square charge-radii changes in Fig. 3c are fairly similar for tin and cadmium. All these features are discussed in the following.

Nuclear structure calculations. The theoretical analysis at the level of nuclear Density Functional Theory [30] (DFT) employs the standard Skyrme functional SV-min [31] and the recently optimized Fayans functional Fy(Δr, HFB) [32], the latter containing gradient terms in surface and pairing energies [33, 34]. Both models are optimized to the same large set of basic ground-state nuclear data [31]. In addition, Fy(Δr, HFB) accommodates the isotopic shifts of

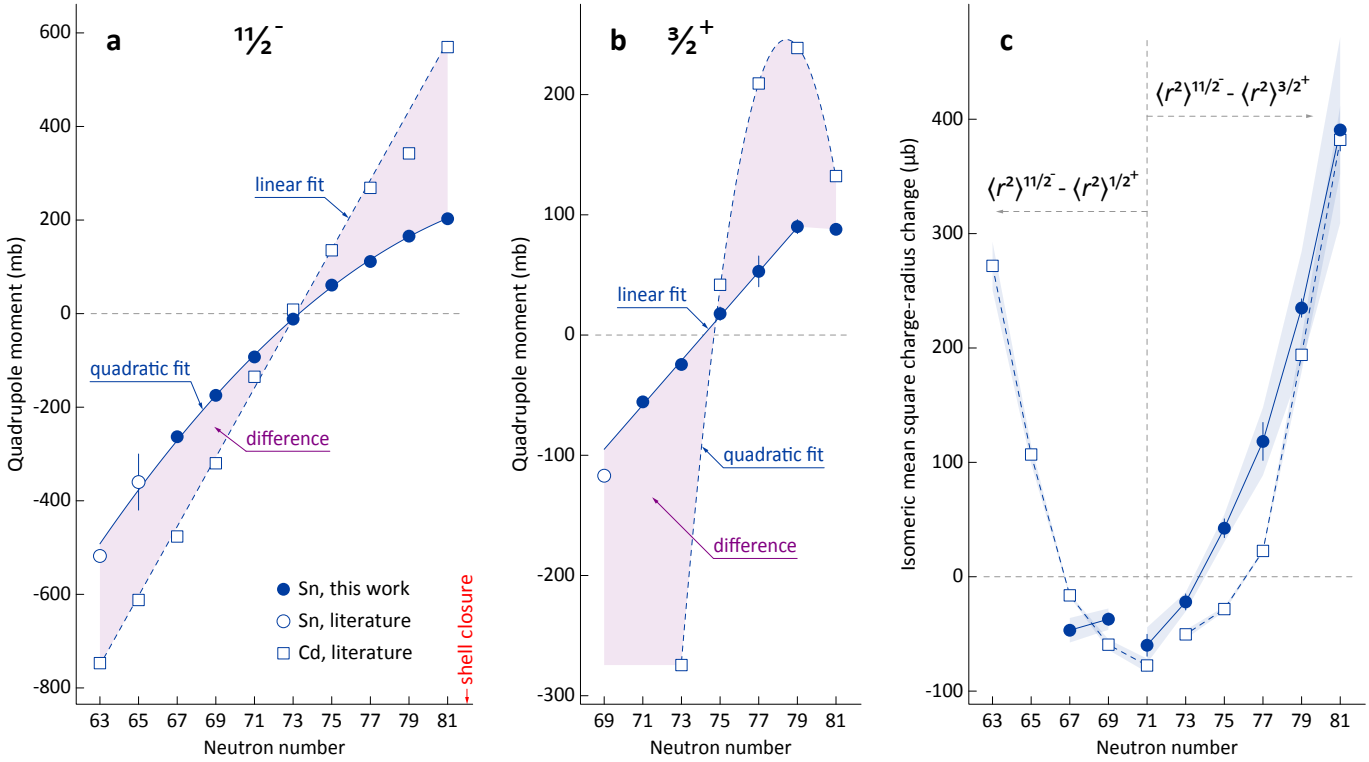

FIG. 3. **Sn vs. Cd: a**, $11/2^-$ quadrupole moments. **b**, $3/2^+$ quadrupole moments. Correlated uncertainties originating from the electric-field gradients are smaller than the dots. **c**, Mean square charge-radii changes for the $11/2^-$ states relative to the $1/2^+$ ($N \leq 71$) and $3/2^+$ ($N \geq 71$) states. Shaded bands represent systematic uncertainties originating from the field-shift coefficients. The literature values are taken from Refs. [26–28].

charge radii in the calcium chain, a feature which could only be achieved by invoking the Fayans gradient terms [32, 35]. The calculations for the charge radius, which is an isotropic observable, were done in spherical approximation with pairing handled at Hartree-Fock-Bogoliubov (HFB) level. The odd nucleons were treated within the blocking ansatz [36]. In principle, the odd nucleon polarizes the nucleus and so perturbs the spherical shape. The impact of this polarization effect on charge radii and correlations beyond mean field are small for heavier spherical species as the tin isotopes [37, 38]. To check the uncertainty from the spherical mean-field approximation, we performed more elaborate blocked HFB calculations allowing axial deformations and spin polarization for the case of the SV-min model. In this variant, each magnetic sub-state produces a slightly different radius whose average is very close to the spherical result. This supports our spherical calculations and the variance of charge radii within a jm shell delivers an estimate of their theoretical uncertainties.

Figure 4a shows the quadrupole moments of $11/2^-$ states in tin and cadmium which were obtained by blocking the $m = 11/2$ magnetic substate of the $h_{11/2}$ orbital in calculations that break spherical symmetry. It is satisfactory to see that the general experimental pattern in Fig. 3a is reproduced. Namely, the quadrupole moments exhibit a smooth increase as a function of the neutron number, with the quadrupole moments of tin being reduced in magnitude relative to cadmium. The enhanced quadrupole correlations in cadmium stem from the enhanced polarizability through the two $g_{9/2}$ proton holes [39, 40]. Indeed, in the nuclear shell model [41] and in nuclear DFT [42], deformation is primarily driven by the isoscalar neutron-proton (quadrupole) interaction, acting against the sphericity-favouring monopole force, which includes the isovector pairing interaction. According to the seniority coupling scheme [5–7], the spectroscopic quadrupole moment should vanish at mid-shell. In SV-min, the neutron $h_{11/2}$ shell becomes half-filled at $N = 75$, as seen in Fig. 4a. Experimentally, the zero crossover point is at $N = 73$, which suggests that the single-particle energy of the $h_{11/2}$ shell is perhaps not optimal in our model. This nicely demonstrates that the present high-precision data on quadrupole moments deliver extremely sensitive criteria for probing the shell structure of a model.

Theoretical values for the isomeric charge-radii shifts of the odd-mass tin isotopes are displayed in Figs. 4b and 4c. The error bars on the SV-min results indicate the estimated uncertainty of the spherical approach as compared to calculations allowing shape deformation as well as spin polarization and subsequent angular momentum projection, as explained above. We expect similar uncertainty for the Fy(Δr, HFB) model. One finds an acceptable agreement for the charge radii difference between the $11/2^-$ and the

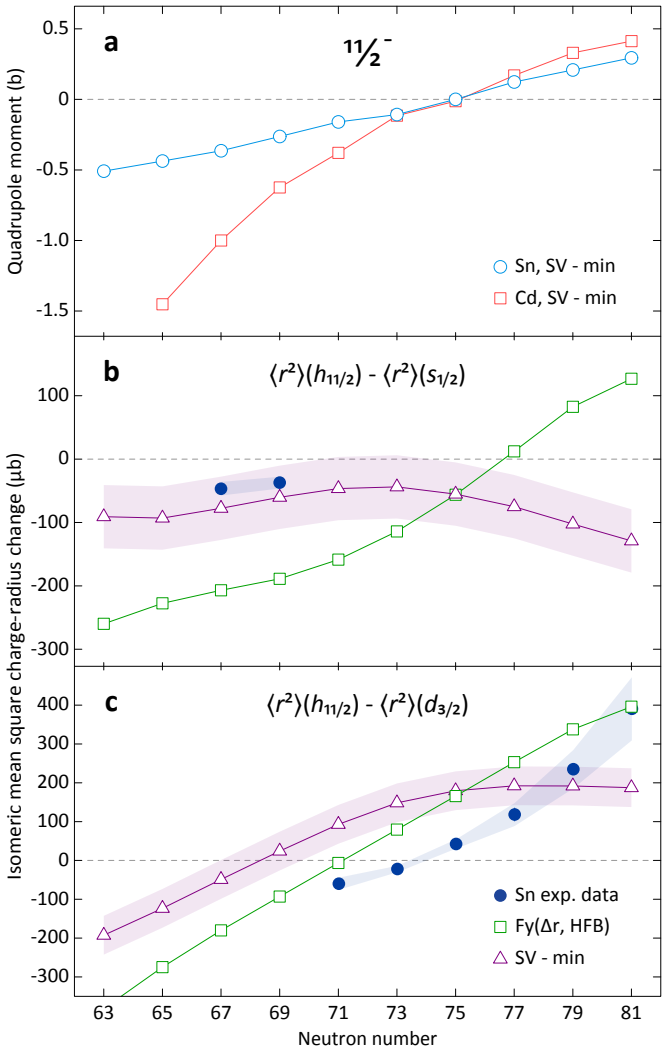

FIG. 4. **Theoretical calculations: a**, $11/2^-$ quadrupole moments in tin and cadmium isotopes computed with the Skyrme density functional SV-min [31]. **b** and **c**, Mean square charge-radii changes for the $11/2^-$ states relative to the $1/2^+$ and $3/2^+$ states in tin obtained with SV-min and the Fayans functional Fy(Δr, HFB) [32].

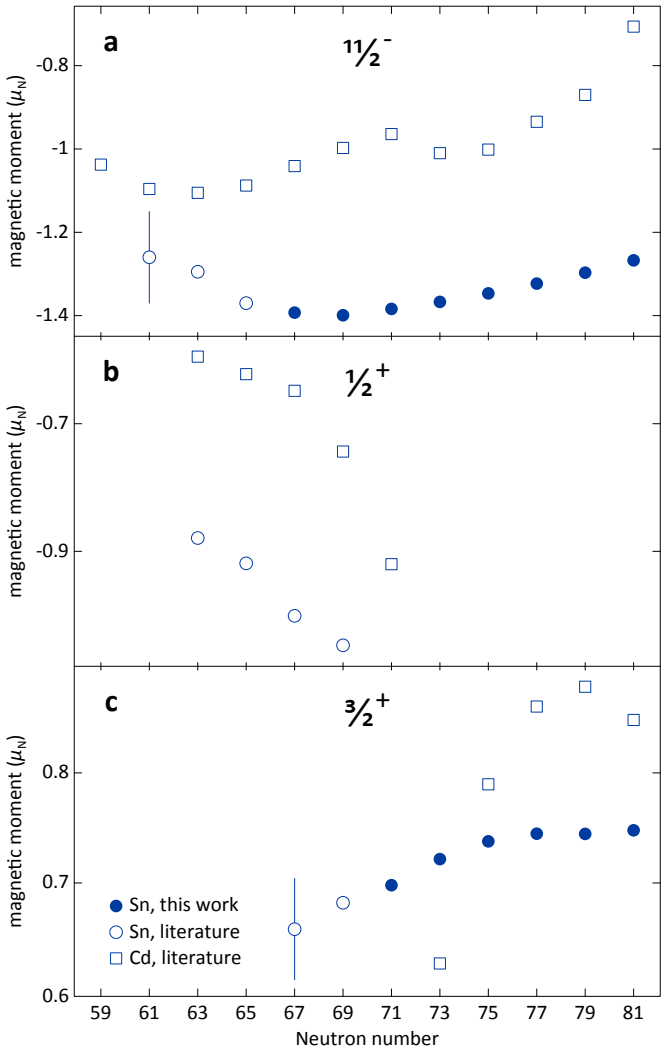

FIG. 5. **Sn vs. Cd: Magnetic moments. a**, of the $11/2^-$ states **b**, of the $3/2^+$ states; **c**, of the $1/2^+$ states. The literature values are taken from Refs. [27, 43]. The current high-resolution data correspond to former measurements in Refs. [44, 45]. The magnetic moment of the $3/2^+$ state in ^{123}Sn is reported for the first time.

$3/2^+$ states, with a preference towards the Fy(Δr, HFB) description, especially when considering the theoretical uncertainty. This is not the case for the radii changes between the $11/2^-$ and the $1/2^+$ states, since the experimental data approach the upper end of theoretical results in Fig. 4b. A word of caution is in order here: the $1/2^+$ state is particularly prone to a dynamical coupling with low-energy quadrupole vibrations which is expected to enhance the charge radius.

The trends of quadrupole moments, linear versus quadratic, are different for cadmium and tin owing to a significant configuration dependence. The latter does not cause a substantial deviation between the corresponding mean square charge-radii changes. Future theoretical analysis would need to address these features in greater detail together with variations of the magnetic moments shown in Fig. 5. Any connection with the quadrupole moments of the lowest 2^+ states in the even-even isotopes [46, 47] should also be examined.

Perspective. Complex systems often display regular patterns. Atomic nuclei, composite structures consisting of hundreds of nucleons, are no exception; they often behave as ordered systems obeying elementary rules [5]. The reason for such simplicities is the presence of many-body symmetries resulting in a collective nucleonic motion. A challenge for the modern microscopic theory is to explain the origin of underlying symmetries.

In this work, we showed that electromagnetic properties of tin nuclei evolve from one isotope to another in a simple way: along a line or parabola. The microscopic mechanisms behind the observed behaviour are rooted in many-body po-

larization effects. While the general trends are explained by theory, the regularities seen at high experimental resolution provide a strong motivation for further theoretical developments.

Similar effects are expected to be common for nuclei whose valence nucleons move in a unique-parity shell. Dedicated studies would be required to refine the systematics in lead and mercury isotopes [48], which are the closest analogues of tin and cadmium in terms of nuclear structure. While initial assessments could be made by in-source measurements [49, 50], the high-resolution spectroscopic techniques employed here, in combination with advanced atomic calculations, will be essential for developing further understanding of complex nuclear systems.

Methods

Hyperfine structure. The electromagnetic interaction of the nucleus with the electron environment in an atom causes splitting of the energy levels which is about a millionth of the fine-structure splitting, hence the term hyperfine structure. The energy shift of the individual hyperfine components equals:

$$E_F - E_J = A\frac{k}{2} + B\frac{3k(k+1) - 4I(I+1)J(J+1)}{8I(2I-1)J(2J-1)},$$

where $A = \mu B_0/(IJ)$ is proportional to the nuclear magnetic moment μ and the average magnetic-flux density at the origin B_0, $B = eQV_{JJ}$ is proportional to the nuclear quadrupole moment Q and the average electric-field gradient at the origin V_{JJ}, $\mathbf{F} = \mathbf{I} + \mathbf{J}$ is the total angular momentum of the atom, and $k = F(F+1) - I(I+1) - J(J+1)$. The hyperfine-structure splitting is determined by the A and B parameters whose values are obtained from experiment. The decay rate per atom, commonly refereed to as Racah intensities [51], is given by:

$$\frac{R}{n} = \frac{\gamma}{3\tau}\frac{(2J_1+1)(2F_1+1)(2F_2+1)}{(2I+1)(2J_2+1)}\begin{Bmatrix} J_2 & F_2 & I \\ F_1 & J_1 & 1 \end{Bmatrix}^2,$$

where τ is the lifetime of the excited atomic state and γ is the ratio between the induced and spontaneous emission coefficients, which incorporates the laser intensity and the spectral lineshape.

Hyperfine anomaly. The A hyperfine constant is influenced by the extended nuclear magnetization, known as Bohr-Weisskopf effect, and the extended nuclear charge distribution, known as Breit-Rosenthal-Crawford-Schawlow correction. Both contribute to the hyperfine anomaly:

$${}^1\Delta^2 = \frac{A_1}{A_2}\frac{I_1}{I_2}\frac{\mu_2}{\mu_1} - 1.$$

Following justification by atomic calculations, the anomaly is neglected in our analysis. However, its estimated contribution to the $11/2^-$ magnetic moments is predicted to be on the level of the experimental precision and it is therefore incorporated into the final uncertainties quoted in Tab. I, as further discussed.

Isomer shifts. A change in the nuclear mean square charge radius between a nuclear ground state and an isomer results in a common energy displacement of all levels in a given hyperfine multiplet. The combined effect in a transition between two atomic levels is manifested in spectra from laser spectroscopy as an apparent "isomer shift". For example, in Fig. 6, this causes the pattern of peaks associated with the $11/2^-$ state in the right column to "walk" towards higher frequencies in the heavier isotopes. The isomer (frequency) shift is a product of the electronic factor, related to a change in the total electronic charge density at the site of the nucleus, and a change in the nuclear mean square charge radius:

$$\delta\nu = F_\lambda \delta\langle r^2\rangle.$$

Distinction should be made between F_λ and the total angular-momentum quantum number F introduced earlier. The effect from a change in the nuclear mass is negligible.

Fitting of multiple spectra. Routines for fitting multiple spectra were developed in the ROOT data analysis framework [52], making use of the WrappedMultiTF1 class for enveloping individual fit functions under a common χ^2. Spectra of the stable $1/2^+$ ground states in ^{115,117,119}Sn, free of quadrupole splitting, were used to determine the proportionality of A factors between the singlet and the triplet state. With this condition applied to the spectra of ^{109}Sn and ^{133}Sn, which are unperturbed by the presence of an isomer, one obtained the ratio of B factors. Individual masses were used for ground and isomeric states [53]. The isomer shifts were constrained to one another by a King plot [54] of data on the even-even isotopes. The three aforementioned ratios are presented in Tab. I. Voigt lineshapes were used with a predominant Lorentzian component emerging from the fits. Resolved lines were fitted with free intensities. The heights of overlapping lines were locked to each other, or to other resolved lines when available, by using the Racah intensities. As constrained above, the fits fully determine the nuclear spins.

Nuclear properties. Using frequency ratios from nuclear magnetic resonance of the $1/2^+$ states in ^{115,117,119}Sn [55], and the latest evaluation of the magnetic moment of ^{119}Sn [18] with an adopted uncertainty of 0.01% [56], one arrives at a high-precision magnetic moment for each of the three isotopes, as given in Tab. I. These in combination with their corresponding A factors in the triplet state are used to determine the ratio $AI\mu_N/(h\mu) = 2396.6(7)$ MHz through a weighted mean, which is then used to extract magnetic moments for the rest of the isotopes. A small hyperfine-anomaly contribution of 0.05% (see the main text) is added in quadrature to the uncertainties of the $11/2^-$ magnetic moments. The quadrupole moments are determined in the singlet state with the electric-field gradient $B/(hQ) = 706(50)$ MHz/b from this work. Using the B ratio reported in Tab. I, the electric-field gradient in the triplet state is found to be $-173(17)$ MHz/b. Both are substantially stronger in comparison with semi-empirical estimates adopted in former studies [44, 45, 57]. This has had an impact on the results of a recent phenomenological analysis [58]. Mean square charge-radii changes are extracted in the triplet state with the field shift $\delta\nu/\delta\langle r^2\rangle = 0.274(57)$ MHz/μb [38].

Data availability

The authors declare that the data supporting this study are published within the paper as histograms in Fig. 6.

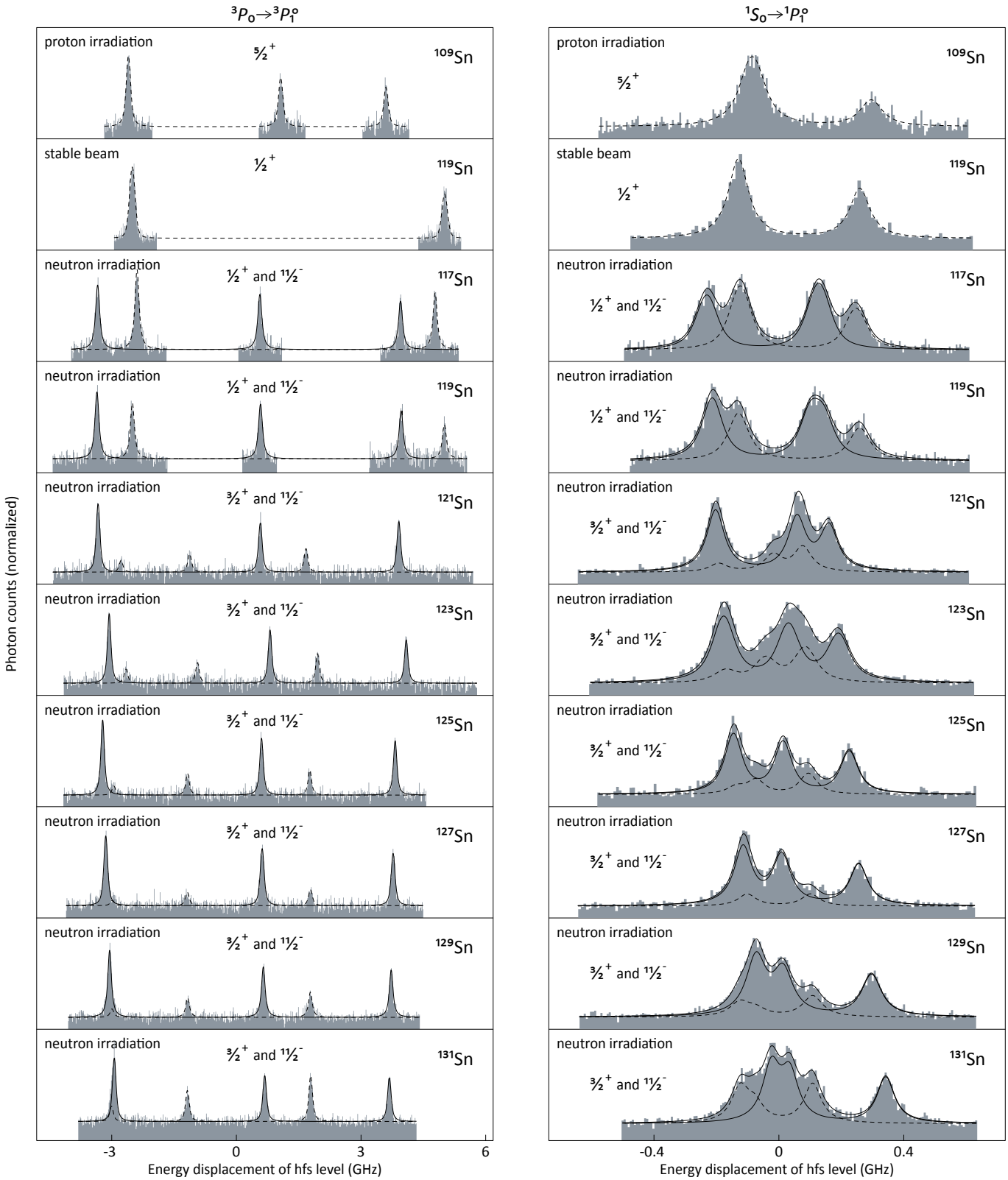

FIG. 6. **Fitted fluorescence spectra of $^{109,\,117\text{-}131}$Sn.** The common frequency scales are relative to the fine-structure splittings in the transitions $5p^2\ {}^3P_0 \rightarrow 5p6s\ {}^3P_1^o$ and $5p^2\ {}^1S_0 \rightarrow 5p6s\ {}^1P_1^o$. Positive- and negative-parity states are represented by dashed and solid lines, respectively. Solid lines in the right column also show the sum fit function. ^{119}Sn is studied from a mass marker to observe only the stable $1/2^+$ g.s., and after target irradiation to detect the radioactive $11/2^-$ state. Spectra of the stable g.s. in $^{115,\,117}$Sn (similar to ^{119}Sn g.s.) are not shown. ^{133}Sn, used together with ^{109}Sn for calibration of the B-ratio, will be published elsewhere.

TABLE I. **Experimental results on $^{109,\,115\text{-}131}$Sn.** Content of each column, from left to right: isotopes; measured nuclear spins I with parity assignments π; magnetic dipole hyperfine constants A in the $5p6s\ ^3P_1^o$ state; isomer shifts relative to the unique-parity state $\delta\nu^{e,o} = \nu^{\text{odd-parity state}} - \nu^{\text{even-parity state}}$, i.e., odd "o" − even "e"; electric quadrupole hyperfine constants B in the $5p6s\ ^1P_1^o$ state; magnetic dipole moments μ in nuclear magnetons μ_N; mean square charge-radii changes relative to the unique-parity state $\delta\langle r^2\rangle^{e,o} = \delta\langle r^2\rangle^{\text{odd-parity state}} - \delta\langle r^2\rangle^{\text{even-parity state}}$; electric quadrupole moments Q with systematic uncertainties from the computed electric-field gradient and the experimental field-shift factor shown in the second sets of parentheses. In the SI system of units 1 b = 100 fm^2 = 10^{-28} m^2.

	I^π	A (MHz)	$\delta\nu^{e,o}$ (MHz)	B (MHz)	μ (μ_N)	$\delta\langle r^2\rangle^{e,o}$ (μb)	Q (mb)
^{109}Sn	$5/2^+$	−1035.8(6)		+154(5)	−1.081(1)		+218(7)(15)
^{115}Sn	$1/2^+$	−4394(2)			−0.9167(1)		
^{117}Sn	$1/2^+$	−4783(2)			−0.9983(1)		
^{117}Sn	$11/2^-$	−606.9(3)	−12(2)	−186(4)	−1.393(1)	−46(5)(11)	−263(6)(19)
^{119}Sn	$1/2^+$	−5011(3)			−1.0448(1)		
^{119}Sn	$11/2^-$	−609.6(4)	−10(2)	−123(3)	−1.399(1)	−37(5)(9)	−175(4)(12)
^{121}Sn	$3/2^+$	+1115(2)		−39(3)	+0.698(1)		−56(4)(4)
^{121}Sn	$11/2^-$	−603.0(3)	−16(3)	−65(2)	−1.384(1)	−60(10)(16)	−93(3)(7)
^{123}Sn	$3/2^+$	+1153(2)		−17(3)	+0.722(1)		−24(4)(2)
^{123}Sn	$11/2^-$	−595.7(3)	−6(2)	−8(2)	−1.367(1)	−22(7)(8)	−12(3)(1)
^{125}Sn	$3/2^+$	+1179(2)		+13(4)	+0.738(1)		+18(6)(1)
^{125}Sn	$11/2^-$	−586.8(2)	+12(2)	+43(2)	−1.347(1)	+42(8)(12)	+61(2)(4)
^{127}Sn	$3/2^+$	+1190(3)		+37(9)	+0.745(2)		+53(13)(4)
^{127}Sn	$11/2^-$	−576.6(3)	+32(5)	+79(2)	−1.323(1)	+118(17)(30)	+111(3)(8)
^{129}Sn	$3/2^+$	+1190(2)		+64(4)	+0.745(2)		+90(6)(6)
^{129}Sn	$11/2^-$	−565.1(2)	+64(2)	+117(2)	−1.297(1)	+235(8)(50)	+166(3)(12)
^{131}Sn	$3/2^+$	+1195(1)		+62(2)	+0.748(1)		+88(2)(6)
^{131}Sn	$11/2^-$	−552.2(2)	+107(1)	+143(2)	−1.267(1)	+391(4)(81)	+203(3)(14)
		$5p6s\ ^3P_1^o$	$5p^2\ ^3P_0 \rightarrow 5p6s\ ^3P_1^o$	$5p6s\ ^1P_1^o$			

$$\frac{A(^1P_1^o)}{A(^3P_1^o)} = 0.0517(2) \qquad \frac{B(^3P_1^o)}{B(^1P_1^o)} = -0.25(2) \qquad \frac{\delta\nu(^1S_0 \rightarrow {}^1P_1^o)}{\delta\nu(^3P_0 \rightarrow {}^3P_1^o)} = 0.91(2)$$

[1] M. Thoennessen, *The Discovery of Isotopes* (Springer, Cham, Switzerland, 2016).

[2] A. Bohr and B. R. Mottelson, *Nuclear Structure*, Vol. 2 (W. A. Benjamin, Inc., Singapore, 1975).

[3] P.-G. Reinhard and E. W. Otten, "Transition to deformed shapes as a nuclear Jahn-Teller effect," Nucl. Phys. **A420**, 173 (1984).

[4] W. Nazarewicz, "Microscopic origin of nuclear deformations," Nucl. Phys. **A574**, 27 (1994).

[5] R. F. Casten, *Nuclear Structure from a Simple Perspective* (Oxford University Press, New York, 1990).

[6] I. Talmi, *Simple Models of Complex Nuclei* (Harwood Academic Publishers, Switzerland, 1993).

[7] I. Talmi, "The shell model - simplicity from complexity: some of my best nuclei are spherical," Phys. Scr. **92**, 083001 (2017).

[8] I. O. Morales, P. Van Isacker, and I. Talmi, "Generalized seniority and E2 transitions in the tin isotopes," Phys. Lett. B **703**, 606 (2011).

[9] A. E. Stuchbery, "Simple structures in complex nuclei versus complex structures in simple nuclei: a nuclear moments perspective," J. Phys.: Conf. Ser. **366**, 012042 (2012).

[10] T. D. Morris, J. Simonis, S. R. Stroberg, C. Stumpf, *et al.*, "Structure of the lightest tin isotopes," Phys. Rev. Lett. **120**, 152503 (2018).

[11] T. Togashi, Y. Tsunoda, T. Otsuka, N. Shimizu, and M. Honma, "Novel shape evolution in Sn isotopes from magic numbers 50 to 82," Phys. Rev. Lett. **121**, 062501 (2018).

[12] M. Siciliano *et al.*, "Pairing-quadrupole interplay in the neutron deficient tin nuclei: first lifetime measurements of low-lying states in ^{106,108}Sn," arXiv:1905.10313 (2019).

[13] A. P. Zuker, "Quadrupole dominance in light Cd and Sn isotopes," arXiv:1905.11479 (2019).

[14] E. M. Burbidge, G. R. Burbidge, W. A. Fowler, and F. Hoyle, "Synthesis of the elements in stars," Rev. Mod. Phys. **29**, 547 (1957).

[15] R. Neugart *et al.*, "Collinear laser spectroscopy at ISOLDE: new methods and highlights," J. Phys. G **44**, 064002 (2017).

[16] U. Köster *et al.*, "Progress in ISOL target-ion source systems," Nucl. Instrum. Methods Phys. Res., Sect. B **266**, 4229 (2008).

[17] E. Mané *et al.*, "An ion cooler-buncher for high-sensitivity collinear laser spectroscopy at isolde," Eur. Phys. J. A **42**, 503 (2009).

[18] E. Malkin, S. Komorovsky, M. Repisky, T. B. Demissie, and K. Ruud, "The absolute shielding constants of heavy nuclei: Resolving the enigma of the ^{119}Sn absolute shielding," J. Phys. Chem. Lett. **4**, 459 (2013).

[19] P. Jönsson, G. Gaigalas, J. Bieroń, C. Froese Fischer, and I. P. Grant, "New version: GRASP2K relativistic atomic structure package," Comput. Phys. Commun. **184**, 2197 (2013).

[20] C. Froese Fischer, G. Gaigalas, P. Jönsson, and J. Bieroń, "GRASP2018 - A Fortran 95 version of the General Relativistic Atomic Structure Package," Comput. Phys. Commun. **237**, 184 (2019).

[21] C. Froese Fischer, M. Godefroid, T. Brage, P. Jönsson, and G. Gaigalas, "Advanced multiconfiguration methods for com-

plex atoms: I. energies and wave functions," J. Phys. B **49**, 182004 (2016).
[22] I. P. Grant, *Relativistic Quantum Theory of Atoms and Molecules. Theory and Computation* (Springer-Verlag, New York, USA, 2007).
[23] A. Papoulia, S. Schiffmann, *et al.*, "*Ab initio* calculations of hyperfine structures of tin and evaluation of the nuclear quadrupole moment of $Q(^{119}\mathrm{Sn})$," (2020), work in progress.
[24] I. I. Tupitsyn and A. V. Loginov, "Use of Sturmian expansions in calculations of the hyperfine structure of atomic spectra," Opt. Spectrosc. **94**, 319 (2003).
[25] J. Ekman, J. Li, P. Jönsson, M. Godefroid, and G. Gaigalas, "Modeling hyperfine anomalies using GRASP," EOS workshop on Electronic Atomic Factors and Hyperfine Anomalies for Nuclear Physics, Brussels (Belgium) (2019).
[26] H. Haas, (2019), data re-evaluation, private communication.
[27] D. T. Yordanov *et al.*, "Spins, electromagnetic moments, and isomers of $^{107\text{-}129}$Cd," Phys. Rev. Lett. **110**, 192501 (2013).
[28] D. T. Yordanov *et al.*, "Simple nuclear structure in $^{111\text{-}129}$Cd from atomic isomer shifts," Phys. Rev. Lett. **116**, 032501 (2016).
[29] N. Frömmgen *et al.*, "Collinear laser spectroscopy of atomic cadmium," Eur. Phys. J. D **69**, 164 (2015).
[30] M. Bender, P.-H. Heenen, and P.-G. Reinhard, "Self-consistent mean-field models for nuclear structure," Rev. Mod. Phys. **75**, 121 (2003).
[31] P. Klüpfel, P.-G. Reinhard, T. J. Bürvenich, and J. A. Maruhn, "Variations on a theme by Skyrme: A systematic study of adjustments of model parameters," Phys. Rev. C **79**, 034310 (2009).
[32] A. J. Miller, K. Minamisono, A. Klose, *et al.*, "Proton superfluidity and charge radii in proton-rich calcium isotopes," Nat. Phys. **15**, 432 (2019).
[33] S. A. Fayans, "Towards a universal nuclear density functional," JETP Lett. **68**, 169 (1998).
[34] S. A. Fayans, S. V. Tolokonnikov, E. L. Trykov, and D. Zawischa, "Nuclear isotope shifts within the local energy-density functional approach," Nucl. Phys. **A676**, 49 (2000).
[35] P.-G. Reinhard and W. Nazarewicz, "Toward a global description of nuclear charge radii: Exploring the fayans energy density functional," Phys. Rev. C **95**, 064328 (2017).
[36] P. Ring and P. Schuck, *The Nuclear Many-Body Problem* (Springer-Verlag, New York, Heidelberg, Berlin, 1980).
[37] M. Hammen, W. Nörtershäuser, *et al.*, "From calcium to cadmium: Testing the pairing functional through charge radii measurements of $^{100\text{-}130}$Cd," Phys. Rev. Lett. **121**, 102501 (2018).
[38] C. Gorges, L. V. Rodríguez, *et al.*, "Laser spectroscopy of neutron-rich tin isotopes: A discontinuity in charge radii across the $N = 82$ shell closure," Phys. Rev. Lett. **122**, 192502 (2019).
[39] P. W. Zhao, S. Q. Zhang, and J. Meng, "Explanation of the simplicity of the quadrupole moments recently observed in Cd isotopes from covariant density functional theory," Phys. Rev. C **89**, 011301(R) (2014).
[40] D. T. Yordanov *et al.*, "Spins and electromagnetic moments of $^{101\text{-}109}$Cd," Phys. Rev. C **98**, 011303(R) (2018).
[41] P. Federman and S. Pittel, "Unified shell-model description of nuclear deformation," Phys. Rev. C **20**, 820 (1979).
[42] J. Dobaczewski, W. Nazarewicz, J. Skalski, and T. Werner, "Nuclear deformation: A proton-neutron effect?" Phys. Rev. Lett. **60**, 2254 (1988).
[43] P. Raghavan, "Table of nuclear moments," At. Data Nucl. Data Tables **42**, 189 (1989).
[44] M. Anselment *et al.*, "Charge radii and moments of tin nuclei by laser spectroscopy," Phys. Rev. C **34**, 1052 (1986).
[45] F. Le Blanc *et al.*, "Charge-radius change and nuclear moments in the heavy tin isotopes from laser spectroscopy: Charge radius of ^{132}Sn," Phys. Rev. C **72**, 034305 (2005).
[46] M. T. Esat, D. C. Kean, R.H. Spear, and A. M. Baxter, "Mass dependence of the static quadrupole moments of the first 2^+ states in the cadmium isotopes," Nucl. Phys. **A274**, 237 (1976).
[47] J. M. Allmond, A. E. Stuchbery, A. Galindo-Uribarri, E. Padilla Rodal, *et al.*, "Investigation into the semimagic nature of the tin isotopes through electromagnetic moments," Phys. Rev. C **92**, 041303(R) (2015).
[48] G. Neyens, "Nuclear magnetic and quadrupole moments for nuclear structure research on exotic nuclei," Rep. Prog. Phys. **66**, 633 (2003).
[49] R. Ferrer, A. Barzakh, *et al.*, "Towards high-resolution laser ionization spectroscopy of the heaviest elements in supersonic gas jet expansion," Nat. Comm. **8**, 14520 (2017).
[50] S. Sels, T. Day Goodacre, B. A. Marsh, A. Pastore, W. Ryssens, Y. Tsunoda, *et al.*, "Shape staggering of midshell mercury isotopes from in-source laser spectroscopy compared with density-functional-theory and Monte Carlo shell-model calculations," Phys. Rev. C **99**, 044306 (2019).
[51] P. C. Magnante and H. H. Stroke, "Isotope shift between ^{209}Bi and 6.3-day ^{206}Bi," J. Opt. Soc. Am. **59**, 836 (1969).
[52] R. Brun and F. Rademakers, "ROOT - An object oriented data analysis framework," Nucl. Instrum. Methods Phys. Res., Sect. A **389**, 81 (1997).
[53] G. Audi, F. G. Kondev, Meng Wang, W. J. Huang, and S. Naimi, "The NUBASE2016 evaluation of nuclear properties," Chinese Phys. C **41**, 030001 (2017).
[54] W. H. King, "Comments on the article "Peculiarities of the isotope shift in the samarium spectrum"," J. Opt. Soc. Am. **53**, 638 (1963).
[55] W. Makulski, "Tetramethyltin study by NMR spectroscopy in the gas and liquid phase," J. Mol. Str. **1017**, 45 (2012).
[56] W. Makulski, K. Jackowski, A. Antušek, and M. Jaszuński, "Gas-phase NMR measurements, absolute shielding scales, and magnetic dipole moments of ^{29}Si and ^{73}Ge nuclei," J. Phys. Chem. A **110**, 11462 (2006).
[57] J. Eberz *et al.*, "Nuclear spins, moments and charge radii of $^{108\text{-}111}$Sn," Z. Phys. A **326**, 121 (1987).
[58] B. Maheshwari, H. Abu Kassim, N. Yusof, and A. K. Jain, "Evolution of nuclear structure in and around $Z = 50$ closed shell: Generalized Seniority in Cd, Sn and Te isotopes," Nucl. Phys. **A992**, 121619 (2019).

Acknowledgements

We thank the ISOLDE technical group for their professional assistance and Heinz Haas for re-evaluating the quadrupole moments of the very short-lived isomers in ^{113,115,119}Sn. This work has been supported by the Max Planck Society, the German Federal Ministry for Education and Research under Contract no. 05P15RDCIA, the Helmholtz International Center for FAIR within the LOEWE program by the State of Hesse, the Belgian IAP Project no. P7/12, the FWO-Vlaanderen, GOA 15/010 from KU Leuven, the European Union seventh framework through ENSAR under Contract no. 262010, the Science and Technology Facilities Council (ST/P004423/1 and ST/P004598/1), and by the Office of Science, U.S. Department of Energy underGrants no.DE-SC0013365 and no. DE-SC0018083 (NUCLEI SciDAC-4 Collaboration). D.L.B. acknowledges support from the EU

Development Fund and Competitiveness Operational Program for the ELI-NP Project Phase II (1/07.07.2016, COP, ID1334), M.R.G. from the FWO & FNRS Excellence of Science Programme (EOS-O022818F), A.P., J.E., and P.J. from the Swedish Research Council (VR) under contract no. 2015-04842, and P.P. from the Magnus Ehrnrooth Foundation.

Author contributions

M.L.B., R.F.G.R., C.G., H.H., S.K., V.L., S.L., S.M.-E., L.V.R., S.S.[21], L.X., X.Y., and D.T.Y. prepared the instrumentation and contributed to the on-line measurements along with D.L.B., K.B., B.C., G.G.[10], W.G., A.K., B.M., R.N., G.N., W.N.[13], R.S., S.S.[13], L.W., C.W., and Z.X. L.V.R. developed routines for fitting of multiple spectra. Nuclear DFT analysis was carried out by W.N.[16] and P.-G.R. J.B., J.E., G.G.[9], M.R.G., Z.H., P.J., C.H.K., N.S.O., A.P., P.P. and S.S.[12, 18] contributed to the *ab initio* large-scale MCDHF and CI-DFS calculations of the relevant electronic parameters and to their reliability assessment. J.E. computed the hyperfine anomalies. D.T.Y. proposed the measurements and prepared the manuscript with input from all authors. These results are part of the PhD theses of C.G. and L.V.R.

Competing interests

The authors declare no competing interests.

Nuclear Charge Radii of $^{21-32}$Mg

D. T. Yordanov,[1,2,*] M. L. Bissell,[3] K. Blaum,[1] M. De Rydt,[3] Ch. Geppert,[4] M. Kowalska,[1,2] J. Krämer,[4] K. Kreim,[1] A. Krieger,[4] P. Lievens,[5] T. Neff,[6] R. Neugart,[4] G. Neyens,[3] W. Nörtershäuser,[4,6] R. Sánchez,[4,6] and P. Vingerhoets[3]

[1]*Max-Planck-Institut für Kernphysik, Saupfercheckweg 1, D-69117 Heidelberg, Germany*
[2]*CERN European Organization for Nuclear Research, Physics Department, CH-1211 Geneva 23, Switzerland*
[3]*Instituut voor Kern- en Stralingsfysica, KU Leuven, B-3001 Leuven, Belgium*
[4]*Institut für Kernchemie, Universität Mainz, D-55128 Mainz, Germany*
[5]*Laboratorium voor Vaste-Stoffysica en Magnetisme, KU Leuven, B-3001 Leuven, Belgium*
[6]*GSI Helmholtzzentrum für Schwerionenforschung GmbH, D-64291 Darmstadt, Germany*

(Received 14 October 2011; published 26 January 2012)

Charge radii of all magnesium isotopes in the *sd* shell have been measured, revealing evolution of the nuclear shape throughout two prominent regions of assumed deformation centered on ^{24}Mg and ^{32}Mg. A striking correspondence is found between the nuclear charge radius and the neutron shell structure. The importance of cluster configurations towards $N = 8$ and collectivity near $N = 20$ is discussed in the framework of the fermionic molecular dynamics model. These essential results have been made possible by the first application of laser-induced nuclear orientation for isotope shift measurements.

DOI: 10.1103/PhysRevLett.108.042504 PACS numbers: 21.10.Ft, 27.30.+t, 31.30.Gs, 42.62.Fi

More than three decades set us apart from the first experimental evidence [1–3] prompting Wildenthal and Chung to discuss a ''collapse of the conventional shell-model ordering in the very-neutron-rich isotopes of Na and Mg'' [4]. The associated concept of an ''island of inversion'' has since evolved and many more experimental data have been integrated into the understanding of these nearly magic, yet apparently unpredictable nuclei. Today, as 30 years ago [5], the abnormal data are still attributed to populating the neutron *pf* shell in the presence of *sd* orbitals at a considerable prolate deformation. This idea was repeatedly revisited in recent years to explain new data on nuclear reactions [6–10], spins, and electromagnetic moments [11–16]. The inversion of states in the deformed shell model is directly related to a change in quadrupole deformation [17,18]. In the spherical shell model an adequate description is found, in terms of cross-shell particle-hole excitations ($\hbar\omega$) due to a reduced $N = 20$ shell gap, increased quadrupole collectivity, gain in pairing energy, and the tensor force [19–22]. However, in this approach the deformation does not appear in the sense of a deformed intrinsic state. Therefore, it is difficult to examine to what degree the island of inversion corresponds to an island of deformation. Accommodating the available reaction data and magnetic moments in a common picture is not trivial due to the model dependences in the interpretation of both. As an additional constraint the spectroscopic quadrupole moment is zero for most key isotopes, due to spin zero or one-half, irrespective of the intrinsic deformation. Clearly, there is a need for an observable sensitive to changes in the nuclear shape and common to all isotopes. In this Letter we present an essential step in that direction, a measurement of the rms charge radii. Furthermore, the radii are of critical importance for assessing the role of cluster configurations in the lighter isotopes, where long-range correlations such as in neon [23] are indeed expected. From this perspective our study also explores the applicability of the mean-field description for light nuclei.

Experimentally the charge radii of magnesium present a challenge. The exotic isotopes on both sides of the *sd* shell require an improvement in sensitivity of more than an order of magnitude compared to conventional fluorescence spectroscopy. For other (alkaline-earth or noble-gas) elements state-selective charge exchange [24] and collisional ionization [25] have solved a similar problem, but these rely on specific features in the atomic spectrum. Background rejection by particle-photon coincidence [26] or beam bunching [27] are inapplicable for the cases with considerable beam contamination. Accordingly, we report in this Letter the first application of laser-induced nuclear orientation for high-accuracy isotope shift measurements.

The experiments were carried out with the collinear laser spectroscopy setup [11,16] at ISOLDE-CERN. High-energy protons impinging on a uranium carbide or a silicon carbide target produced neutron-rich or neutron-deficient isotopes, respectively. Magnesium was laser ionized, accelerated to an energy of 50 keV [28] and mass separated. The ion of magnesium (Mg II) was excited in the transition $3s\ ^2S_{1/2} \rightarrow 3p\ ^2P_{1/2}$ (D_1 line at 280.35 nm), which is free of quadrupole interaction and has a well-resolved hyperfine structure. The corresponding ultraviolet light was produced by frequency doubling the output of a stabilized ring dye laser, using Rhodamine 19 as the active medium, pumped at 532 nm. In the conventional manner the atomic transitions were detected by the fluorescence as a function of the Doppler-shifted laser frequency while scanning the ion-beam velocity. The quantity measured was the atomic isotope shift:

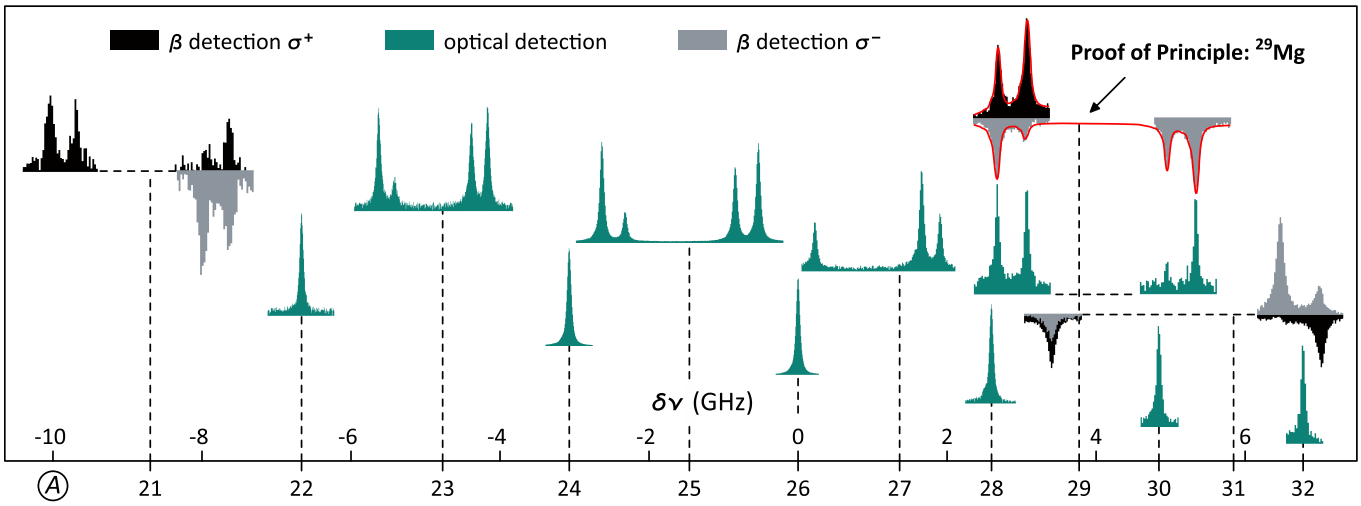

FIG. 1 (color online). Spectral lines of Mg II in the transition $3s\ ^2S_{1/2} \rightarrow 3p\ ^2P_{1/2}$ on a scale relative to the frequency of ^{26}Mg II. The fine structure level of each isotope is represented with a dotted line. All spectra are normalized to a common height. The fitted curves on the β-asymmetry spectra of ^{29}Mg represent the realistic polarization function discussed in the text.

$$\delta\nu^{AA'} = \nu^{A'} - \nu^{A} = K\frac{m_{A'} - m_A}{m_{A'}m_A} + F\delta\langle r^2\rangle^{AA'},$$

with ν^A and $\nu^{A'}$ representing the transition frequencies with respect to the fine structure levels of a reference and a probe isotope, $K = K_{\mathrm{NMS}} + K_{\mathrm{SMS}}$ the sum of the normal and the specific mass shift, m_A and $m_{A'}$ the atomic masses, F the electronic factor, and $\delta\langle r^2\rangle^{AA'} = \langle r^2\rangle^{A'} - \langle r^2\rangle^{A}$ the change in the nuclear mean square charge radius. All measurements used ^{26}Mg [29] as a reference. All isotopes in the range from ^{22}Mg to ^{28}Mg were produced with rates sufficient for fluorescence spectroscopy (above 10^6 ions/s). This method is to a large extent insensitive to the contaminant beams, most notably of sodium and aluminum. In order to enhance the sensitivity to the lower-yield even-even isotopes the photon detection was correlated with the ion beam. In the case of ^{30}Mg ($\approx 5 \times 10^5$ ions/s, $\tau_{1/2} = 335$ ms) the signal was gated on the short release from the target after each proton pulse. True photon-ion coincidence was introduced for the measurements on ^{32}Mg ($\approx 5 \times 10^4$ ions/s), where the ion-beam current also served as a signal normalization against fluctuations of the isotope production. Further use of the coincidence method was limited by the presence of isobaric beam contamination. In addition the sensitivity to nuclei with nonzero spin is generally lower by an order of magnitude. Clearly, the odd isotopes required a different approach.

The application of β-asymmetry detection vastly enhanced the sensitivity and solved the contamination problem by selecting the radioactivity of interest. The atomic angular momenta $\boldsymbol{F} = \boldsymbol{J} + \boldsymbol{I}$ were oriented in the direction of beam propagation by optical pumping with circularly polarized light. A longitudinal magnetic field of 1 mT was used to maintain the polarization axis. The nuclear spin was decoupled from the electron angular momentum by transporting the ion adiabatically into a strong transversal magnetic field of 0.3 T, thus leading to the final nuclear orientation. Excitation in the hyperfine structure transitions was then identified by monitoring the β-decay asymmetry $(N_{0^\circ} - N_{180^\circ})/(N_{0^\circ} + N_{180^\circ})$ after implantation in a MgO crystal.

This orientation method has never been used before as an instrument for investigating isotope shifts. The reason is related to an incomplete control of the orientation process if beams of neutral atoms are used. This was realized in the work on sodium [11] when numerical simulations of the optical pumping process were introduced. In the present work the magnesium ions only interact with the laser light in a well-defined section of constant electrical potential and small longitudinal magnetic field. It was shown [16] that under such conditions the numerical simulations have the potential to quantify the β-asymmetry spectra. For this purpose one needs to solve a system of rate equations $\dot{N} = \hat{M} \cdot N$ for each excitation frequency. Here N is the vector of population densities, $\dot{N} = dN/dt$ and $\hat{M}$ is a $n \times n$ matrix involving the Einstein coefficients, where $n = 2(2I + 1)(J_{\mathrm{lower}} + J_{\mathrm{upper}} + 1)$. Following population transfer in the adiabatic passage to the Paschen-Back regime the orientation is translated from atomic into nuclear. This procedure provides the basis for a realistic polarization function developed to fit the experimental spectra. The equivalence between fluorescence and β-asymmetry detection was investigated on the basis of ^{29}Mg (Fig. 1). This nuclide was accessible by both methods due to its high production rate ($\approx 10^6$ ions/s) and sufficiently short half-life with respect to relaxation times ($\tau_{1/2} = 1.3$ s). The corresponding isotope shifts (Table I) were found consistent within about 2 standard deviations. The small discrepancy may have a statistical origin or could be related to slightly different experimental conditions. The *sd* shell

was completed by measurements with the new method on ^{31}Mg ($\approx 2 \times 10^5$ ions/s) and ^{21}Mg ($\approx 5 \times 10^4$ ions/s). Degrader plates were used in the latter case [30] to shield the detectors from the contaminant beam, whose β decay is much less energetic. By recording the hyperfine structure with left-hand and right-hand circular laser polarization and fitting both simultaneously, one is able to extract information on the magnetic field and the laser power in a self-consistent way. Apart from the moments, radii, and spins the new method is also sensitive to the value and sign of the integral β-decay asymmetry parameter. This quantity can be used, for instance, to aid spin-parity assignments in the daughter nuclei. Such a discussion, however, as well as a detailed description of the numerical approach extend beyond the scope of this Letter and will be published separately.

Typical spectra of all studied isotopes are shown in Fig. 1. Changes in mean square charge radii are extracted from the isotope shifts through a King-plot procedure using the radii [31] of the stable isotopes. The corresponding specific mass shift and the electronic factor of the transition are in excellent agreement with theory [32]. All results are presented in Table I. The systematic errors of the isotope shifts correspond to a 10^{-4} relative uncertainty of the beam energy [28]. These do not influence the extracted radii as they only affect the mass shifts obtained from the King plot [33,34]. This means the accuracy of the radii differences and the absolute radii is essentially determined by the uncertainties of the reference radii. Hence, the corresponding systematic errors are correlated and play no role for the physics discussion.

The total rms charge radii of magnesium spanning the complete *sd* shell are plotted in Fig. 2(a). Clearly, the experimental points lie on three separate slopes signifying three distinct modes of the nuclear size along the chain. This is also evident in Fig. 2(b), which in essence represents the derivative. The physical meaning of the differential plot is an increase of the mean square charge radius by the addition of two neutrons. There is a striking correspondence between the data points and the neutron *sd* orbitals. Beginning with ^{21}Mg the charge distribution is compressed with filling the $d_{5/2}$ orbital up to ^{26}Mg ($N = 14$). A similar effect has also been observed in neon [23,34]. The addition of two neutrons on either $s_{1/2}$ or $d_{3/2}$ in the range $^{28\text{-}30}$Mg results in a steady increase of the radius represented by the middle level in Fig. 2(b). Finally, ^{31}Mg and ^{32}Mg define a third level, which is associated with the island of inversion and in terms of the shell structure would correspond to a cross-shell excitation of two neutrons [12,21]. In ^{27}Mg one of the neutrons added to ^{25}Mg fills the last $d_{5/2}$ hole and the other populates the $s_{1/2}$ subshell, resulting in the intermediate position in Fig. 2(b). Already from a general perspective three important conclusions can be made. First, an island "of inversion" does exist in terms of the rms charge radius and has a well-defined border between

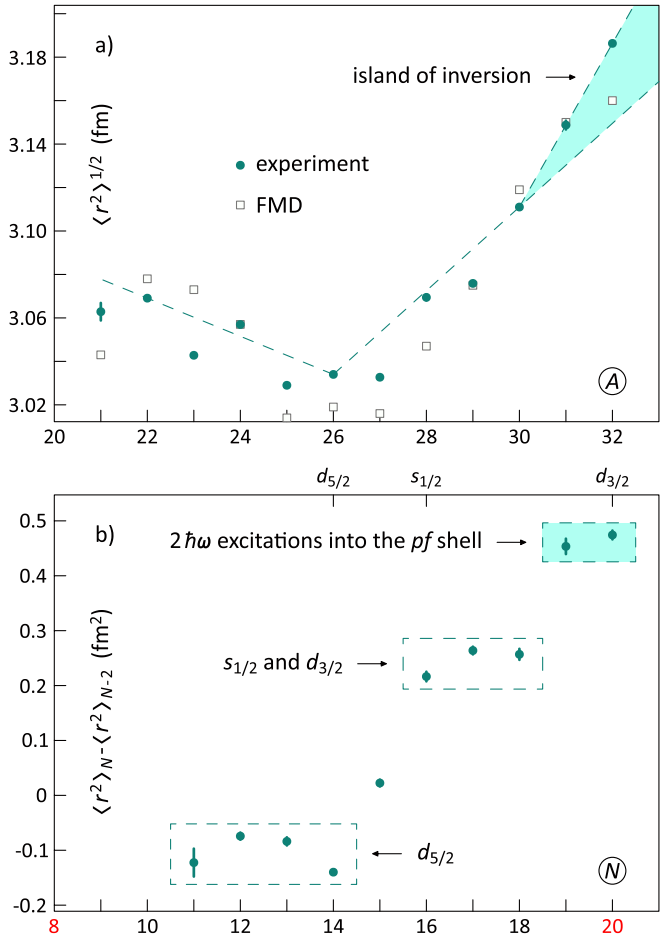

FIG. 2 (color online). Experimental rms charge radii of magnesium (a) compared to theory and differential mean square radii (b). The correlated systematic uncertainties (Table I) are not depicted. Dotted lines and boxes have an illustrative purpose only.

^{30}Mg and ^{31}Mg, as previously anticipated [12,35]. Second, the odd-even staggering is well pronounced except for ^{31}Mg. This indicates a structural change with a prominent effect already in the first isotope of the island. Third, the charge (proton) distribution is strongly correlated with the neutron shell structure.

The role of the quadrupole deformation in the above observations needs to be disentangled from other effects that may contribute. In the mean-field picture the addition of neutrons increases the radius of the mean field for protons, causing the proton distribution to expand. More neutrons also support more binding for protons as the proton-neutron interaction is more attractive than the proton-proton interaction, thus causing the charge distribution to shrink. Alternatively, in the spherical shell model changing trends of the charge radii could be considered as changing contributions from the two major oscillator shells involved, which have different radii and may be associated with different polarizations of the proton distribution. In an attempt to understand these mechanisms we employ the

TABLE I. Nuclear charge radii of $^{21-32}$Mg and isotope shifts of Mg II in the transition $3s\ ^2S_{1/2} \rightarrow 3p\ ^2P_{1/2}$. The statistical and the systematic uncertainties are presented in round and square brackets, respectively.

A	$\delta\nu^{26,A}$ (MHz)	$\delta\langle r^2\rangle^{26,A}$ (fm^2)	$\langle r^2\rangle^{1/2}$ (fm)
21	−8694.3 (31) [345]	0.176 (24) [63]	3.0629 (40) [106]
22	−6663.7 (6) [264]	0.214 (5) [51]	3.0691 (7) [86]
23	−4770.8 (8) [190]	0.053 (6) [34]	3.0428 (10) [61]
24	−3070.6 (7) [122][a,b]	0.140 (5) [25]	3.0570 (7) [48]
25	−1458.5 (6) [58][a]	−0.030 (4) [11]	3.0290 (7) [31]
26	0	0	3.0340 (26)[c]
27	1363.1 (5) [57]	−0.008 (4) [10]	3.0327 (7) [30]
28	2596.5 (11) [118]	0.216 (9) [27]	3.0695 (14) [51]
29	3772.2 (7) [160][d]	0.256 (6) [36]	3.0759 (9) [64]
30	4843.2 (6) [207]	0.473 (5) [56]	3.1110 (8) [94]
31	5845.1 (16) [250]	0.710 (13) [79]	3.1488 (20) [127]
32	6778.4 (8) [310]	0.948 (6) [101]	3.1863 (10) [161]

$F = -127(12)$ MHz/fm^2 $\quad K_{\mathrm{SMS}} = 370(4)$ GHz u

[a]Reference shifts of the n-deficient data set, to be compared with −3073.4(9) [128] and −1460.0(23) [62] of the n-rich data set.
[b]To be compared with −3084.905(93) from in-trap work [29].
[c]Reference rms charge radius of ^{26}Mg [31].
[d]To be compared with 3774.9(9) from β-asymmetry detection.

fermionic molecular dynamics approach (FMD). The many-body basis states are given by intrinsic Slater determinants built from Gaussian wave packets projected on parity and angular momentum [36,37]. Compared with the work on neon [23], we slightly modified the spin-orbit strength of the effective interaction for a better description of the island of inversion. The quadrupole deformation β is used in the present calculation as a generator coordinate. In the island of inversion we find two minima as a function of β corresponding to the normal ($0\hbar\omega$) and the intruder ($2\hbar\omega$) configuration. The matter densities of the two are explicitly shown in Fig. 3 for the case of ^{32}Mg. The full wave function is generated by diagonalizing the Hamiltonian using the β-constrained basis states. Calculated rms charge radii for all measured isotopes are presented in Fig. 2(a). Trends in the deformation of the dominant intrinsic state coincide with the evolution of the radii. Strong deformation and correspondingly large radii, related to γ softness and clustering, are found for $^{22-24}$Mg ($\beta_{^{22}\mathrm{Mg}} = 0.40$). Small charge radii are calculated for the less deformed $^{25-27}$Mg ($\beta_{^{26}\mathrm{Mg}} = 0.22$). With the volume expansion towards ^{30}Mg there is a rapid increase of the radii combined with slightly decreasing deformation ($\beta_{^{30}\mathrm{Mg}} = 0.17$). In the island of inversion we find strong deformation for the intruder configurations ($\beta_{^{32}\mathrm{Mg}} = 0.32$) and further increase of the charge radii. Neutron separation energies are reproduced reasonably well except at the border of the island (^{31,32}Mg) where the sd-pf shell gap is overestimated. As a consequence, the $1/2^+$ ground-state configuration of ^{31}Mg [12] appears in the calculation as an excited state. The magnetic moments of the odd isotopes are found close to the experimental values. Most notably this applies for the $1/2^+$ level of ^{31}Mg, suggesting it has the correct structure and adding confidence to its radius presented in Fig. 2(a). The calculated 2_1^+ energies of the even-even isotopes are also in good agreement with experiment. Description of the experimentally observed odd-even staggering would require either a variation after angular-momentum projection or an explicit treatment of pairing. Mean-field calculations using either Gogny or Skyrme force reproduce roughly the general trends with the minimum at $N = 14$, but are mostly concerned with the even-even cases.

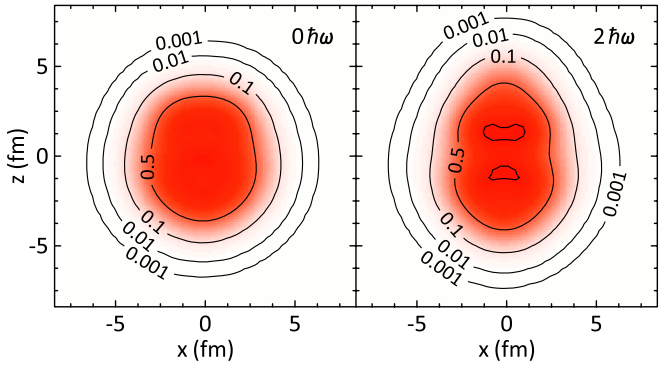

FIG. 3 (color online). Cuts through the matter densities of the intrinsic normal ($0\hbar\omega$) and intruder ($2\hbar\omega$) configurations in ^{32}Mg.

In summary, laser-induced nuclear orientation was combined with fluorescence techniques in order to access all magnesium isotopes in the sd shell. The borderline of the island of inversion was clearly identified between ^{30}Mg and ^{31}Mg. The radial increase towards $N = 8$ is attributed to cluster configurations and γ softness. Both regions were associated with prolate deformation within the fermionic molecular dynamics model. Further theoretical and experimental work is expected to help understand in greater detail the nuclear structure revealed by the rms charge radii.

We are thankful to J.-P. Ebran, T. Rodríguez, and K. Washiyama for providing comparison to mean-field calculations. This work has been supported by the Max-Planck Society, the German Federal Ministry for Education and Research under Contract No. 06MZ9178I, the Helmholtz Association (VH-NG-148), the P6-EURONS (RII3-CT-2004-506065), the BriX IAP Research Program (P6/23), and the FWO-Vlaanderen. A. K. acknowledges support from the Carl Zeiss Stiftung (AZ: 21-0563-2.8/197/1). The authors thank the ISOLDE technical group for their professional assistance.

*Deyan.Yordanov@cern.ch

[1] C. Thibault *et al.*, Phys. Rev. C **12**, 644 (1975).
[2] G. Huber *et al.*, Phys. Rev. C **18**, 2342 (1978).
[3] C. Detraz *et al.*, Phys. Rev. C **19**, 164 (1979).

[4] B. H. Wildenthal and W. Chung, Phys. Rev. C **22**, 2260 (1980).
[5] X. Campi *et al.*, Nucl. Phys. **A251**, 193 (1975).
[6] T. Motobayashi *et al.*, Phys. Lett. B **346**, 9 (1995).
[7] H. Iwasaki *et al.*, Phys. Lett. B **522**, 227 (2001).
[8] Z. Elekes *et al.*, Phys. Rev. C **73**, 044314 (2006).
[9] K. Wimmer *et al.*, Phys. Rev. Lett. **105**, 252501 (2010).
[10] H. T. Fortune, Phys. Rev. C **84**, 024327 (2011).
[11] M. Keim *et al.*, Eur. Phys. J. A **8**, 31 (2000).
[12] G. Neyens *et al.*, Phys. Rev. Lett. **94**, 022501 (2005).
[13] P. Himpe *et al.*, Phys. Lett. B **643**, 257 (2006).
[14] D. Yordanov *et al.*, Phys. Rev. Lett. **99**, 212501 (2007).
[15] P. Himpe *et al.*, Phys. Lett. B **658**, 203 (2008).
[16] M. Kowalska *et al.*, Phys. Rev. C **77**, 034307 (2008).
[17] I. Hamamoto, Phys. Rev. C **76**, 054319 (2007).
[18] D. Yordanov *et al.*, Phys. Rev. Lett. **104**, 129201 (2010).
[19] E. K. Warburton, J. A. Becker, and B. A. Brown, Phys. Rev. C **41**, 1147 (1990).
[20] K. Heyde and J. L. Wood, J. Phys. G **17**, 135 (1991).
[21] A. Poves and J. Retamosa, Phys. Lett. B **184**, 311 (1987).
[22] T. Otsuka *et al.*, Phys. Rev. Lett. **95**, 232502 (2005).
[23] W. Geithner *et al.*, Phys. Rev. Lett. **101**, 252502 (2008).
[24] R. E. Silverans *et al.*, Nucl. Instrum. Methods Phys. Res., Sect. B **26**, 591 (1987).
[25] R. Neugart *et al.*, Nucl. Instrum. Methods Phys. Res., Sect. B **17**, 354 (1986).
[26] D. A. Eastham *et al.*, Opt. Commun. **60**, 293 (1986).
[27] A. Nieminen *et al.*, Phys. Rev. Lett. **88**, 094801 (2002).
[28] A. Krieger *et al.*, Nucl. Instrum. Methods Phys. Res., Sect. A **632**, 23 (2011).
[29] V. Batteiger *et al.*, Phys. Rev. A **80**, 022503 (2009).
[30] J. Krämer *et al.*, Phys. Lett. B **678**, 465 (2009).
[31] G. Fricke and K. Heilig, *Nuclear Charge Radii* (Springer-Verlag, Berlin, Heidelberg, New York, 2004).
[32] B. K. Sahoo, J. Phys. B **43**, 231001 (2010).
[33] A. Klein *et al.*, Nucl. Phys. **A607**, 1 (1996).
[34] K. Marinova *et al.*, Phys. Rev. C **84**, 034313 (2011).
[35] O. Niedermaier *et al.*, Phys. Rev. Lett. **94**, 172501 (2005).
[36] R. Roth *et al.*, Nucl. Phys. **A745**, 3 (2004).
[37] T. Neff and H. Feldmeier, Eur. Phys. J. Special Topics **156**, 69 (2008).